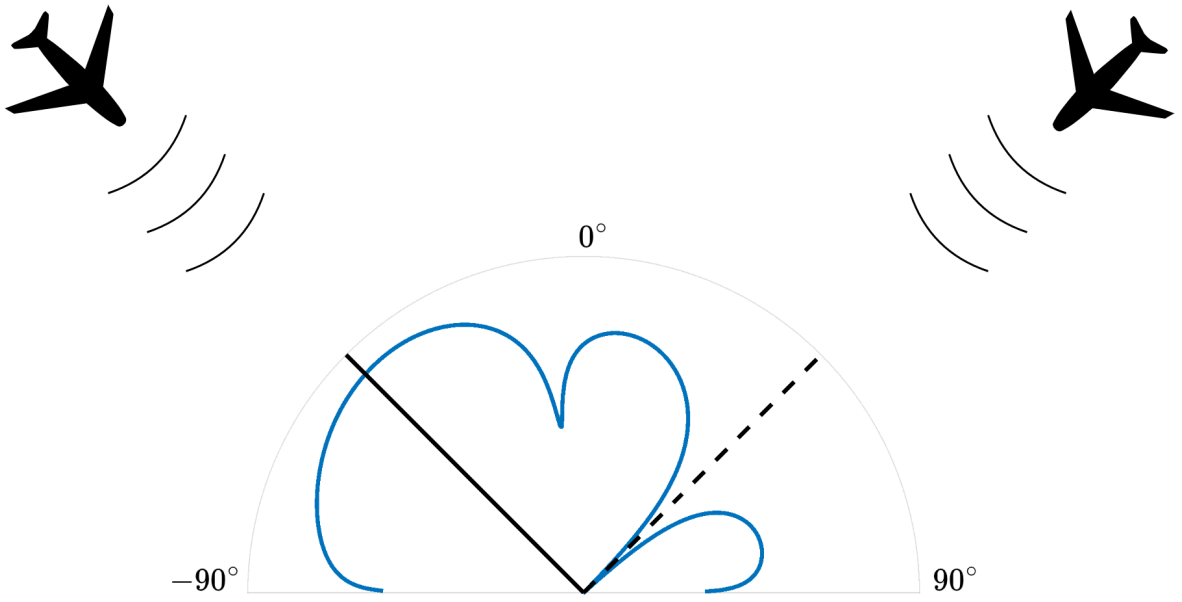

Digital Beamforming for a Secondary Surveillance Radar

Numerical and statistical analysis of the ADS-B reception performance for an SSR system with conventional and adaptive beamforming

Master's thesis in Complex Adaptive Systems

MATTIAS WIKLUND

DEPARTMENT OF MATHEMATICAL SCIENCES

CHALMERS UNIVERSITY OF TECHNOLOGY
Gothenburg, Sweden 2024
www.chalmers.se

Master's thesis 2024

Digital Beamforming for a Secondary Surveillance Radar

Numerical and statistical analysis of the ADS-B reception performance for an SSR system with conventional and adaptive beamforming

MATTIAS WIKLUND

CHALMERS
UNIVERSITY OF TECHNOLOGY

Department of Mathematical Sciences
Division of Applied Mathematics and Statistics
Chalmers University of Technology
Gothenburg, Sweden 2024

Digital Beamforming for a Secondary Surveillance Radar
Numerical and statistical analysis of the ADS-B reception performance for an SSR system with conventional and adaptive beamforming
MATTIAS WIKLUND

Supervisors: Ida-Maria Svensson, Lars Sundell & Juan Cabello Sánchez, Saab AB
Examiner: Adam Andersson, Department of Mathematical Sciences

Master's Thesis 2024
Department of Mathematical Sciences
Division of Applied Mathematics and Statistics
Chalmers University of Technology
SE-412 96 Gothenburg
Telephone +46 31 772 1000

Cover: Beam pattern in polar coordinates for adaptive linear constraint minimum power (LCMP) beamforming. A signal of interest is marked with a solid line and an interfering signal with a dashed line.

Typeset in LaTeX
Printed by Chalmers Reproservice
Gothenburg, Sweden 2024

Digital Beamforming for a Secondary Surveillance Radar
Numerical and statistical analysis of the ADS-B reception performance for an SSR system with conventional and adaptive beamforming
MATTIAS WIKLUND
Department of Mathematical Sciences
Chalmers University of Technology

Abstract

A secondary surveillance radar (SSR) is a surveillance radar system which, rather than detecting reflected signals, relies on interrogations and replies to identify targets. In this master's thesis, the performance of an SSR system is analyzed. The performance is measured by estimating the probability to detect Automatic Dependent Surveillance-Broadcast (ADS-B) signals interfered by other signals on the 1090 MHz frequency band. The study is performed using different beamforming techniques, with the aim of enhancing the reception in some directions while reducing it in others. The probability of detection is estimated by performing Monte Carlo simulations for different target positions and interference scenarios. Simulations are performed for a system using digital beamforming, individually digitizing the received signal in the different antenna elements in the SSR. Both conventional beamforming, using a fixed set of beam positions, and adaptive beamforming, using properties of the received data to optimize the reception, is analyzed. This is benchmarked against a system using analog conventional beamforming, where the signals are decoded in either a sum or a difference channel. The results of this study highlight the potential of digital beamforming, significantly increasing the probability of detection compared to the analog system, especially in an environment with large amounts of interfering signals. Among the adaptive algorithms tested, linear constraint minimum power (LCMP) beamforming, imposing null constraints on interfering signals, exhibited the most promising results. There is potential to build on this work, further analyzing the applicability of the different beamforming techniques. Future research areas could include analyzing more adaptive algorithms, as well as optimizing the ones studied in this thesis.

Keywords: Secondary surveillance radar, ADS-B, Conventional beamforming, Adaptive beamforming, Statistical signal processing, Monte Carlo simulations.

Acknowledgements

First and foremost, I would like to express my deepest gratitude to my supervisors Ida-Maria Svensson, Lars Sundell and Juan Cabello Sánchez. Ida, for your immense commitment and continuous support throughout the whole project. Your mentorship and feedback helped me navigate this thesis. Lars, for all rewarding and ever so interesting discussions about theoretical concepts and ideas. Juan, for always being ready to answer questions and offer advice. Moreover, I would like to thank my examiner Adam Andersson, for contributing with valuable input, and my Saab manager Johan Lindström, for giving me the opportunity to work on this project. To my fellow master's thesis students at Saab, thank you for enjoyable and much-needed breaks during many long and at times challenging days. Lastly, I would like to express my gratitude to friends and family for supporting me not only during this project, but throughout my Engineering Physics studies at Chalmers. And not least − thank you, Mom and Dad, for your ceaseless love and support.

Mattias Wiklund, Gothenburg, June 2024

List of Acronyms

Below is the list of acronyms that have been used throughout this thesis listed in alphabetical order:

ACAS	Airborne collision avoidance system
ADS-B	Automatic Dependent Surveillance-Broadcast
AESA	Active electronically scanned array
CMC	Multi-channel system using conventional beamforming
DOA	Direction of arrival
ESPRIT	Estimation of signal parameters via rotational invariance techniques
FRUIT	False replies unsynchronised in time
GPS	Global Positioning System
ICAO	International Civil Aviation Organization
IFF	Identification friend or foe
LCMP	Linear constraint minimum power
LMS	Least mean squares
LNA	Low-noise amplifier
LOS	Line-of-sight
MAE	Mean absolute error
MDL	Minimum detection level
MPDR	Minimum power distortionless response
MUSIC	Multiple signal classification
PC	Principal component
PESA	Passive electronically scanned array
PSR	Primary surveillance radar
RADAR	Radio detection and ranging
SIR	Signal-to-interference ratio
SMI	Sample matrix inversion
SNR	Signal-to-noise-ratio
SOI	Signal of interest
SSR	Secondary surveillance radar
ULA	Uniform linear array

Contents

List of Figures

List of Tables

1

Introduction

Ever since the breakthrough of electromagnetic theory in the 19th century, the application of radio waves has been a topic of great interest in physics and engineering. Based on the property that surfaces can reflect these waves, it was realized that this phenomenon could be used to detect different objects. The potential for military applications was soon realized, leading to the development of radio detection and ranging (RADAR) systems during World War II [1], [2]. In the decades that followed, the technology was developed further. The areas of application grew, also including civilian aircraft surveillance, and the acronym "RADAR" now became a concept of its own.

A radar system commonly used in aircraft surveillance is the primary surveillance radar (PSR) [1]. It functions by measuring the reflected waves from aircraft within range. From this, the position of the aircraft can be estimated. One major advantage of the PSR is its independence of the onboard equipment of the targets. However, the system has its limitations. It does not know whether the reflected signals are coming from actual aircraft targets or from other objects. Such unwanted reflections are known as clutter. Moreover, targets close to each other are difficult to identify separately.

To address the limitations of the PSR, the secondary surveillance radar (SSR) was developed. Rather than relying on reflected signals, the SSR operates by transmitting interrogations to targets. The received reply contains the identity of the target. The SSR requires less power than the PSR, as the signals only has to reach the target rather than also being reflected back. Moreover, the problem with clutter is reduced by transmitting the interrogations and replies on different frequency bands: 1030 MHz for interrogations and 1090 MHz for replies. The SSR has multiple applications related to air traffic control. One such important application is Identification friend or foe (IFF) [3]. This identification system, implemented in both ground- and air-based radars, was originally developed to prevent "friendly fire" incidents. IFF systems are today used for both military and civilian purposes, and is a requirement for several flying platforms.

The SSR is not the only surveillance technology operating on the 1090 MHz band. Automatic Dependent Surveillance-Broadcast (ADS-B) is a technology in which aircraft periodically broadcast their position, identity and other information of interest [1]. Hence, there is no need for interrogations. Since ADS-B signals are transmitted on the same frequency band as SSR replies, 1090 MHz, this enables them to be

detected by SSR systems [4]. As air traffic continues to grow, there is an increasing risk that ADS-B signals are interfered by other signals on the 1090 MHz band. ADS-B is an important part of air traffic control and flight safety, and missed replies can therefore potentially have dire consequences. Thus, it is of great importance to enhance the ability to decode the information encoded in an ADS-B signal of interest.

There are different signal processing techniques which can be applied to detect a signal of interest, despite it being interfered by other signals. One important technique is beamforming, where the receiving antenna in the radar is used in such a way that the reception of signals is enhanced in some directions and reduced in others [5], [6]. There is conventional beamforming, which utilizes the fact that an incoming wave has different times of arrival at the different antenna elements building up the antenna. This corresponds to a relative phase shift between the elements. By adding a compensatory phase shift, maximum reception can be obtained in a desired direction. Depending on whether this is performed in hardware or software, the beamforming can be either analog or digital [7]. Moreover, there is adaptive beamforming, in which properties of the received data are used to optimize the reception performance in certain directions [6]. Unlike the conventional case, this enables more possibilities in handling different interference scenarios.

1.1 Aims and outline of the thesis

In this thesis, the main aim is to analyze the performance of an airborne SSR system using different types of beamforming techniques. The signal of interest is assumed to be an incoming ADS-B signal. The performance parameter analyzed is the probability of detection, defined here by the amplitude of the signal of interest as well as its relation to the amplitude of possible interfering signals. This parameter is estimated for every point in a simulated spatial grid using Monte Carlo simulations. Simulations are performed for digital systems using both conventional and adaptive beamforming, and their performance is benchmarked against an analog system using conventional beamforming.

The outline of the thesis is as follows: In Chapter 2, the underlying theory behind the work is presented. This includes the characteristics of the different signals and systems, antenna theory and mathematical formulations of beamforming. In Chapter 3, the implementation is described. This includes all models and assumptions, as well as a description of the Monte Carlo simulations performed. In Chapter 4, the obtained results are presented. This includes main results for the probability of detection, as well as some illustrative beamforming examples and a deeper analysis on the adaptive algorithms. In Chapter 5, the results are interpreted and discussed in relation to the underlying theory and the methods used. Potential limitations of the methods are discussed, as well as an outlook for future studies. In Chapter 6, the findings in the thesis are summarized, thus concluding this work.

2

Theory

The following chapter contains the theory behind this thesis. This includes the characteristics of SSR replies and ADS-B signals, configuration of SSR systems, fundamental antenna theory, mathematical aspects of conventional and adaptive beamforming, as well as estimation theory.

2.1 Secondary Surveillance Radar and ADS-B

A secondary surveillance radar uses an interrogator transmitting signals on the 1030 MHz frequency band [1]. A transmitter-responder, transponder, within range can receive this signal and transmit a reply with a frequency on the 1090 MHz band. According to international rules and regulations, all flying platforms are obliged to have a transponder and antenna for receiving interrogations and replying [4]. A simple illustration of the principle behind an airborne SSR system, which is the focus of this thesis, can be seen in Figure 2.1 below. The reply contains information requested by the interrogation, where different interrogation modes contain different types of information. The different modes are in general characterized by the spacing between the pulses in the transmitted waveform.

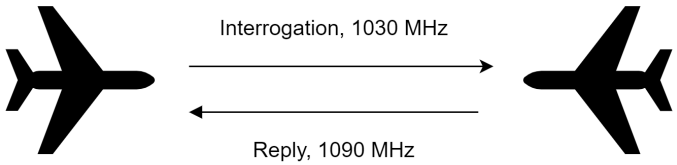

Figure 2.1: A simple illustration of the principle behind an airborne SSR system. An aircraft transmits interrogations on the 1030 MHz frequency band. Under certain circumstances, governed by regulations, another transponder-equipped aircraft should then transmit a reply on the 1090 MHz frequency band.

The most common mode with civilian use is Mode S (Mode Select) [1]. It it "selective" in the sense that this mode enables selective interrogation of individual aircraft. This is possible thanks to a 24-bit unique code, or address, being assigned to each aircraft. The address is encrypted in the waveform and regulated by the International Civil Aviation Organization (ICAO) [4]. A 24-bit address gives $2^{24} - 2 = 16,777,214$ unique codes (the two codes only containing zeros or ones are not valid). This can

for example be compared to the older Mode A, where the address instead is given by a four-digit octal number, yielding only $8^4 = 4,096$ different codes. For increased air traffic, this can result in several aircraft in the same region with identical addresses, with potential safety risks as a consequence.

Looking closer on the transmitted waveforms, or codes, a Mode S interrogation starts with two pulses of length 0.8 µs, with a relative time delay of 2 µs [1]. This is known as the preamble, and has the purpose of preventing replies from transponders using other modes. After the preamble follows a longer pulse, the data block, containing the interrogation information. The data block is phase-modulated using differential phase-shift keying modulation, with a phase reversal resulting in bit 1 and no phase reversal resulting in bit 0. There are two types of Mode S interrogations: short with a 16.125 µs data block containing 56 bits and long with a 30.25 µs data block containing 112 bits.

The reply from a transponder has a format similar to the interrogation with a preamble and a data block, but with a different composition. The reply preamble has four pulses of length 0.5 µs. The data block that follows contains 56 or 112 bits, with the rate of one bit/µs [1]. The information requested in the interrogation, for example the identity of the aircraft, is encoded in the different parts of the data block. It is encoded using pulse-position modulation, where bit 1 is indicated by a 0.5 µs pulse followed by a flat signal of the same length. Bit 0 is instead indicated by a flat signal followed by a pulse. This is also known as Manchester encoding [8]. Consequently, 0 is coded as [0, 1] and 1 is coded as [1, 0]. An example of this encoding scheme is illustrated in Figure 2.2 below.

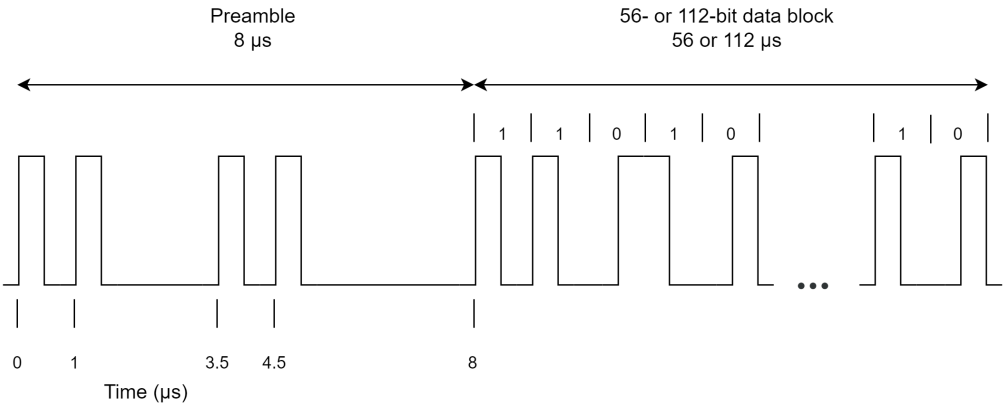

Figure 2.2: The waveform of a Mode S reply. It begins with a 8 µs long preamble, containing four pulses of length 0.5 µs. The length of the data block is either 56 or 112 µs, depending on whether it is a long or short reply. The information in the data block is encoded using a digital pulse-position modulation, with ”0” being represented by a pulse in the second half of the bit period, whereas ”1” has a pulse in the first half.

Different information is encoded in different parts of the waveform. For example, this includes the format number, indicating which type of response it is, the 24-bit

address and a parity check, used for finding and correcting potential errors in the message [1]. Mathematically, the reply waveform can be described as

$$a(t) = \sum_{k=0}^{2t_{\text{reply}}-1} a_k \text{rect}(t - kt_{\text{pulse}}), \tag{2.1}$$

where t_{reply} is either 64 or 120 µs, a_k is the Manchester encoded data for entry k and rect(t) is a rectangular pulse of width $t_{\text{pulse}} = 0.5$ µs [9].

A subset of Mode S Long replies is ADS-B, Automatic Dependent Surveillance-Broadcast. This is a surveillance system where aircraft broadcasts their position and other relevant flight data periodically, without any need for interrogation [1]. A simple illustration of this principle can be seen in Figure 2.3. ADS-B is "dependent" in the sense that the transmitted information is dependent on other systems, such as the Global Positioning System (GPS). This is a commonly used surveillance technology and since 2020, civil aircraft in Europe and the United States are required to be compatible with ADS-B.

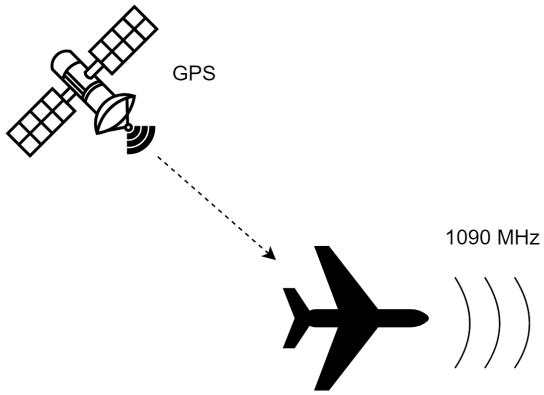

Figure 2.3: A simple illustration of the principle behind ADS-B. An aircraft determines its position using GPS and transmits the information on the 1090 MHz frequency band.

ADS-B is a Mode S of type "Extended Squitter". In this case, a "squitter" refers to periodic burst transmissions not generated by interrogations [4]. It should be noted that ADS-B messages have different transmissions rates depending on the information transmitted. Messages related to airborne position and velocity are transmitted twice per second.

2.2 Interfering signals

In order for the information in the ADS-B waveform to be decoded, the signal must first be detected. There are several factors affecting the possibility to detect a signal of interest (SOI), in this case an ADS-B signal. One such factor is the occurrence of interfering signals. In areas with large amounts of air traffic, there are many signals in air on the 1090 MHz frequency band. Hence, the SOI may be interfered by these

signals. This could for example be other ADS-B signals or replies from a transponder that has been interrogated by another SSR interrogator. This phenomenon is known as FRUIT (False replies unsynchronized in time) [10]. When such replies overlap with the SOI, this results in "garbling". This could potentially result in the target not being detected or detection of non-existing targets. A simple illustration of this phenomenon can be seen in Figure 2.4, where two Mode S replies are interfering with an ADS-B signal of interest.

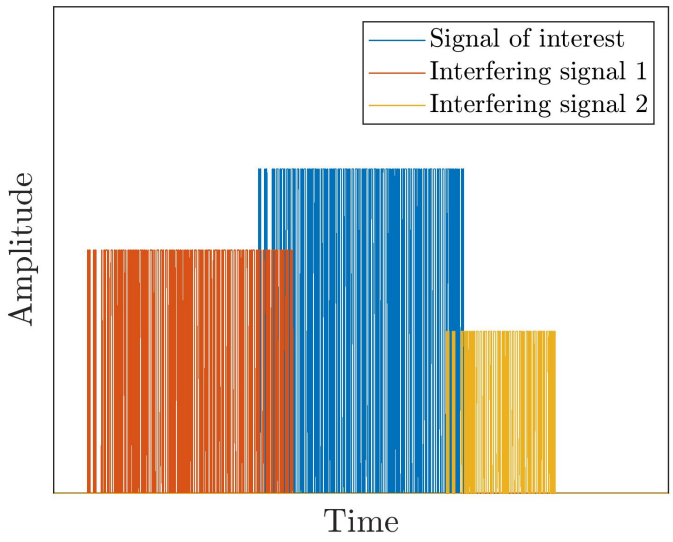

Figure 2.4: Illustration of an ADS-B signal of interest (blue) partly overlapped with two interfering signals, one of type Mode S Long (red) and one of type Mode S Short (yellow). The amplitudes are chosen arbitrarily and no noise is added.

The interfering signals overlapping with an SOI can be seen as random points in time following a Poisson point process [11], [12]. This assumption holds as long as the interfering signals occur independently of each other. The number of interfering signals in a time span of limited size can then be seen as a random variable following a Poisson distribution. The discrete probability density function for this distribution, given a discrete random variable, X, is given by

$$\mathbb{P}(X = k) = \frac{\lambda_{\text{Poi}}^{k} \mathrm{e}^{-\lambda_{\text{Poi}}}}{k!}, \tag{2.2}$$

where k is the number of events, with an expected value of λ_{Poi} [13]. Translated to the scenario of interest here, the expected value can be written as $\lambda_{\text{Poi}} = t_{\text{Poi}}\mu$, where t_{Poi} is the time span and μ is the intensity of interfering signals.

Analyzing the time span in closer detail, the signal of interest is an ADS-B signal with length $t_{\text{SOI}} = t_{\text{ADS-B}} = 120$ µs. Now assume that an interfering signal has length t_{int}. Note that the start of a signal can be seen as a Poisson event. If an SOI begins at time t, an interfering signal overlaps with the SOI as long as it begins anywhere in the interval $[t - t_{\text{int}}, t + t_{\text{SOI}}]$. Therefore, in order for λ_{Poi} to represent the

expected number of interfering signals, the time span is given by $t_{\text{Poi}} = t_{\text{SOI}} + t_{\text{int}}$. For example, $t_{\text{int}} = 120$ µs if the interfering signal is of type Mode S Long and $t_{\text{int}} = 64$ µs if it is of type Mode S Short.

It is, however, possible to detect an SOI, even though interfering signals are overlapping with it. By applying different signal processing techniques, the amplitudes of the interfering signals can be suppressed, while the amplitude of the SOI could be amplified. This affects the signal-to-interference-ratio, defined as the quotient between the received signal power and the sum of the power of the interfering signals. For a given time, t, and spatial location, $\boldsymbol{r}$, this gives

$$\text{SIR}(\boldsymbol{r}, t) = \frac{P_{\text{SOI}}(\boldsymbol{r}, t)}{\sum_{i=1}^{D} P_i(\boldsymbol{r}, t)},$$

where $P_{\text{SOI}}(\boldsymbol{r}, t)$ is received power from the signal of interest and $P_1(\boldsymbol{r}, t), P_2(\boldsymbol{r}, t), \ldots, P_D(\boldsymbol{r}, t)$ are the signal power for D interfering signals [14]. Often, this ratio is written in decibel units, according to

$$\text{SIR}^{[\text{dB}]}(\boldsymbol{r}, t) = 10 \log_{10} \left(\frac{P_{\text{SOI}}(\boldsymbol{r}, t)}{\sum_{i=1}^{D} P_i(\boldsymbol{r}, t)} \right).$$

To detect an SOI and decode the information encoded in its waveform, the SIR should typically be above a given threshold.

2.3 Array antennas

In the last sections, the focus has been on the characteristics of signals and how interference can impair the possibility to detect them. The focus is now shifted towards the configuration of SSR systems.

For an SSR to be able to transfer waves propagating in free space to electrical signals in a circuit, an antenna is required. In this thesis, the focus is on an SSR system based on an array antenna, where the signals in several smaller antennas (antenna elements) interfere with each other constructively and destructively, respectively [5]. In the case of a receiving antenna, this enhances the reception in some directions and reduces it in others, depending on the relative phase between the elements. This process is known as beamforming and is described in more detail in Section 2.6.

An incoming signal has different times of arrival at the different elements. For narrowband signals, this time difference can be translated into a phase difference between the elements [6]. In a phased array, the beamforming process is done by utilizing this phase difference and adding a compensatory phase shift at each element. In practice, this is done by having each element connected to a computer-controlled phase shifter. This way, the antenna beam can be electronically steered to a desired direction. There are different types of phased arrays. In a passive electronically scanned array (PESA), all the individual elements are connected to one and the same transmitter/receiver module, while in an active electronically scanned array (AESA), the different elements all have their own transmitter and receiver module [15].

2.3.1 Uniform linear arrays

A special case of an array antenna is the uniform linear array (ULA) [6]. This type of array consists of N antenna elements placed along a line with a uniform spacing d between them. For this purpose, it is convenient to introduce a spherical coordinate system defined according to Figure 2.5. A unit vector in this system can be written as

$$\hat{\boldsymbol{a}} = \sin\theta\cos\phi\hat{\boldsymbol{x}} + \cos\theta\cos\phi\hat{\boldsymbol{y}} + \sin\phi\hat{\boldsymbol{z}},$$

where θ is the azimuth angle and ϕ is the elevation angle. The figure displays a ULA with six symmetrically placed elements on the x axis, with a physical area in the x-z plane.

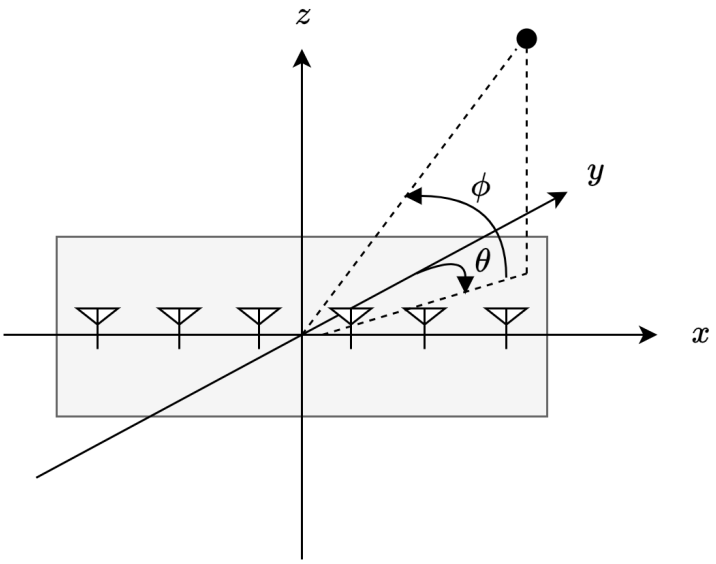

Figure 2.5: Three-dimensional illustration of a uniform linear antenna with six elements located on the x axis. The azimuth angle θ is measured from the y axis to the orthogonal projection of the radial line onto the x-y plane. The elevation angle ϕ is measured from the orthogonal projection to the radial line. The shaded region in the x-z plane represents the physical area of the antenna.

If the elements are symmetrically placed around the origin and on the x axis, the position of the nth element can be written as

$$p_n = \left(n - \frac{N+1}{2}\right) d,$$

for $n = 1, 2, \ldots, N$. Note that this work focuses on the horizontal cut $\phi = 0$, assuming an airborne radar looking at long distances. An illustration of a uniform linear antenna with $N = 6$ in the x-y plane ($\phi = 0$) is shown in Figure 2.6. This displays an incoming plane wave in the x-y plane, with azimuth angle θ relative to antenna normal on the y axis.

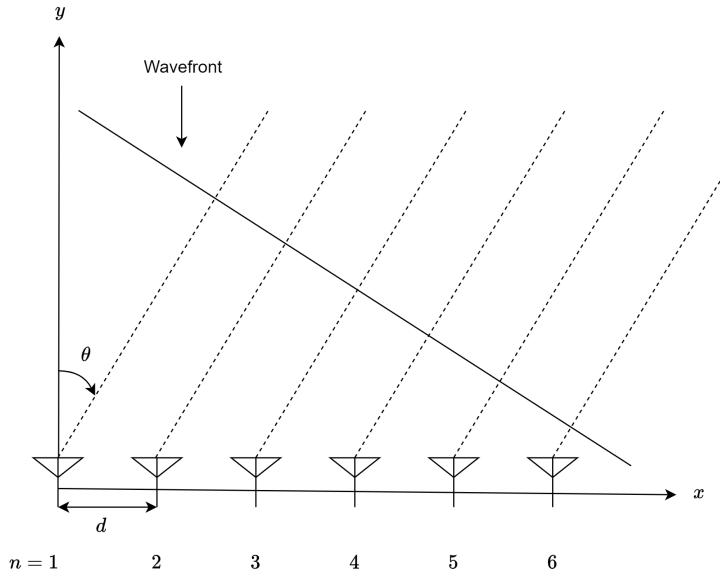

Figure 2.6: Illustration of a uniform linear antenna with six elements with distance d between them in the x-y plane. The wavefront has an angle θ relative to the antenna normal.

Now assume that a plane wave in the x-y plane with azimuth angle θ is received by the ULA. The wave arriving at element n travels an extra distance of $\Delta x = d \sin\theta$ compared to an adjacent element. This corresponds to a time delay of $\Delta t = \Delta x/c$, where c is the speed of light. Assuming a narrowband signal, the time delay can in turn be written as a phase shift according to

$$\Delta\varphi = 2\pi \frac{\Delta t}{T_{\text{period}}} = 2\pi \frac{\Delta x}{\lambda} = \frac{2\pi d \sin\theta}{\lambda}, \tag{2.3}$$

where T_{period} and λ is the period and wavelength of the incoming wave, respectively [6]. How this phase difference relates to the beamforming process is explored more in Section 2.6.

2.4 Properties of a receiving antenna

There are other aspects than the occurrence of interfering signals affecting the ability to detect a signal of interest, not least the performance of the receiving antenna in the SSR. One important performance parameter is the gain of the antenna. The gain of a receiving antenna describes how well the antenna can absorb incident power in a given direction and convert it to electrical power [16], [17]. In general, this is described in terms of a ratio of the radiation intensities for a directional antenna and a theoretical isotropic antenna, i.e., an antenna absorbing the same intensity in all directions.

Gain can also be defined as $G = \eta D$, where η is the radiation efficiency and D is the directivity. The radiation efficiency is a measure of how efficient an antenna

can convert between the power of the incoming wave and electrical power. For a lossless antenna, $\eta = 1$. The directivity describes the degree of concentration for the absorbed radiation in a given direction.

2.4.1 Friis transmission equation

For a given frequency, the gain can also be expressed in terms of effective aperture areas for the directional antenna and a theoretical isotropic antenna. The effective aperture area, A_{eff}, describes how much power, P_{r}, from an incoming plane wave which is captured by an antenna and transformed to electrical power [18]. Again focusing on the horizontal cut $\phi = 0$, this can be described by the intensity, $\boldsymbol{S}(\theta)$, according to

$$P_{\text{r}} = A_{\text{eff}}|\boldsymbol{S}(\theta)|.$$

The power absorbed by the antenna can also be related to the incoming plane wave power, P_{in}, according to

$$P_{\text{r}} = \eta P_{\text{in}} = \eta A_{\text{physical}}|\boldsymbol{S}(\theta) \cdot \hat{\boldsymbol{y}}| = \eta A_{\text{physical}}|\boldsymbol{S}(\theta)| \cos\theta,$$

where A_{physical} is the physical area of the antenna and $\hat{\boldsymbol{y}}$ is a unit vector normal to the antenna on the x axis. Note that P_{in} is free-space power, while P_{r} is conductive power. This gives

$$A_{\text{eff}} = \eta A_{\text{physical}} \cos\theta. \tag{2.4}$$

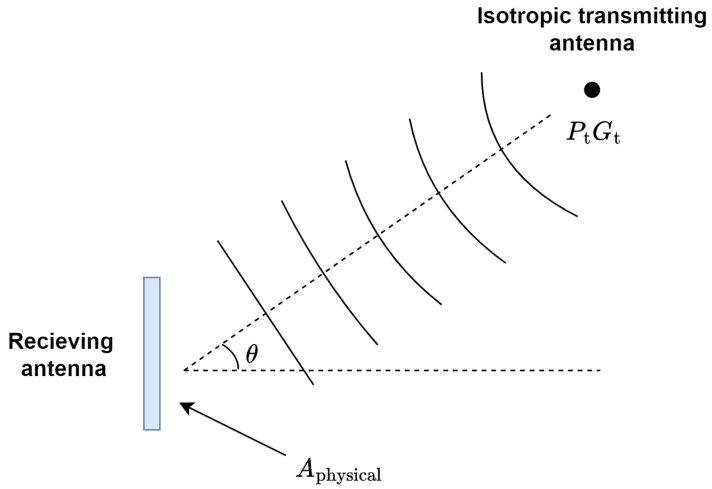

Figure 2.7: A simple illustration of an isotropic transmitting antenna and a receiving antenna, where the incoming wavefront has an angle θ relative to the normal of the receiving antenna. The effective radiated power from the transmitter is $P_{\text{t}}G_{\text{t}}$ and the receiving antenna has a physical area A_{physical}. Note that the plane-wave approximation is assumed to hold at the receiver.

Relating the effective aperture area to the gain, G_{r}, of the receiving antenna, this gives

$$G_{\text{r}} = \frac{P_{\text{r}}}{P_{\text{iso}}} = \frac{A_{\text{eff}}}{A_{\text{iso}}},$$

where A_{iso} is the effective aperture area of an isotropic antenna with output power P_{iso} [16]. For an incident wave with wavelength λ, the effective aperture area of an isotropic antenna is

$$A_{\text{iso}} = \frac{\lambda^2}{4\pi}.$$

Therefore, the relation between the effective aperture area of the receiving antenna and its gain is given by

$$A_{\text{eff}} = \frac{G_{\text{r}}\lambda^2}{4\pi}.$$

The effective radiated power from a transmitting source is given by scaling the output power, P_{t}, with its gain, G_{t}. Assuming an isotropic transmitting antenna at a distance r from the receiving antenna, its intensity, $S_{\text{t}} = |\boldsymbol{S}_t(\theta)|$, is then given by

$$S_{\text{t}} = \frac{P_{\text{t}}G_{\text{t}}}{4\pi r^2}.$$

The available power at the receiver is therefore given by

$$P_{\text{r}} = S_{\text{t}}A_{\text{eff}} = \frac{P_{\text{t}}G_{\text{t}}}{4\pi r^2} \cdot \frac{G_{\text{r}}\lambda^2}{4\pi} = P_{\text{t}}G_{\text{t}}G_{\text{r}}\left(\frac{\lambda}{4\pi r}\right)^2 = \frac{P_{\text{t}}G_{\text{t}}G_{\text{r}}}{L_{\text{p}}}, \tag{2.5}$$

where $L_{\text{p}} = (4\pi r/\lambda)^2$ is the path loss. This result is known as Friis transmission equation, and is used to calculate the amount of power received at a certain distance given the characteristics of the transmitting and receiving antennas [16]. An illustration of a transmitting and a receiving antenna can be seen in Figure 2.7. Using decibel units instead, Friis transmission equation can be written as

$$P_{\text{r}}^{[\text{dBW}]} = P_{\text{t}}^{[\text{dBW}]} + G_{\text{t}}^{[\text{dBi}]} + G_{\text{r}}^{[\text{dBi}]} - L_{\text{p}}^{[\text{dB}]}.$$

Note that power is expressed in dBW (decibel-Watt) and gain in dBi (decibel-isotropic), since this quantity is defined in relation to an isotropic antenna.

2.4.2 Noise and minimum detectable signal

To detect a signal, the received power, P_{r}, should be sufficiently high so that it can be distinguishable from background noise in the system. The noise can for example be thermal Johnson−Nyquist noise, generated by random motion of electrons in the components of the receiving antenna [19]. This sensitivity of the system can be described as the system minimum detection level, MDL, defined according to

$$\text{MDL}^{[\text{dBW}]} = \text{Noise floor}^{[\text{dBW}]} + \text{SNR}_{\text{min}}^{[\text{dB}]}.$$

SNR_{min} is the minimum signal-to-noise-ratio required for the receiver to detect the signal [20]. The noise floor level is given by properties of the system such as bandwidth and temperature.

It is convenient to describe the incoming signals as complex numbers, compactly capturing both magnitude and phase. Assuming the noise is a complex random

variable, n, its variance is given by the sum of the variance of its real and imaginary parts according to

$$\mathrm{Var}[n] = \mathrm{Var}[\mathrm{Re}(n)] + \mathrm{Var}[\mathrm{Im}(n)].$$

Given that both the real and imaginary parts of the noise have variance σ_{n}^2, this gives $\mathrm{Var}[n] = 2\sigma_{\mathrm{n}}^2$ [21]. Note that the standard deviation of the noise corresponds to its amplitude, meaning that the variance, the square of the standard deviation, corresponds to its power. Assuming a complex normal distribution with zero mean, the noise in each of the N antenna elements, $\boldsymbol{n} \in \mathbb{C}^N$, is then given by $\boldsymbol{n} \sim \mathcal{CN}(\boldsymbol{0}, 2\sigma_{\mathrm{n}}^2 \boldsymbol{I}_N)$, where $\boldsymbol{I}_N$ is the N-dimensional identity matrix. The probability density function for an N-dimensional complex normal distribution is given by

$$f(\boldsymbol{z}) = \frac{1}{\pi^N \det(\boldsymbol{\Sigma})} \exp\Big(-(\boldsymbol{z}-\boldsymbol{\mu})^{\mathrm{H}} \boldsymbol{\Sigma}^{-1} (\boldsymbol{z}-\boldsymbol{\mu})\Big), \tag{2.6}$$

where "H" is the Hermitian transpose, $\boldsymbol{\mu} \in \mathbb{C}^N$ is the mean and $\boldsymbol{\Sigma} \in \mathbb{C}^{N \times N}$ is the non-singular covariance matrix [21].

2.5 Configuration of SSR systems

There are different ways to utilize the antenna elements in the phased array in the SSR system. One alternative is to use a two-channel system, or a Σ/Δ system [17]. An illustration of such as system can be seen in Figure 2.8. Focusing on a receiving antenna, the power of the incoming signal is amplified using low-noise amplifiers (LNA). The signal in each element is then electronically shifted to the desired phase. Following this, the signal can be divided into two halves, left and right.

The division into a left and right half can be described in terms of beam patterns, $B(\theta)$. $B(\theta)$ describes how well the antenna can receive a signal from certain direction. As before, the horizontal cut $\phi = 0$ is assumed. Note that the beam pattern is related to the gain parameter introduced in Section 2.4. The gain is directly proportional to the power pattern, $P(\theta)$, which is the squared magnitude of the beam pattern [6]. Consequently, $G(\theta) \propto P(\theta) = |B(\theta)|^2$.

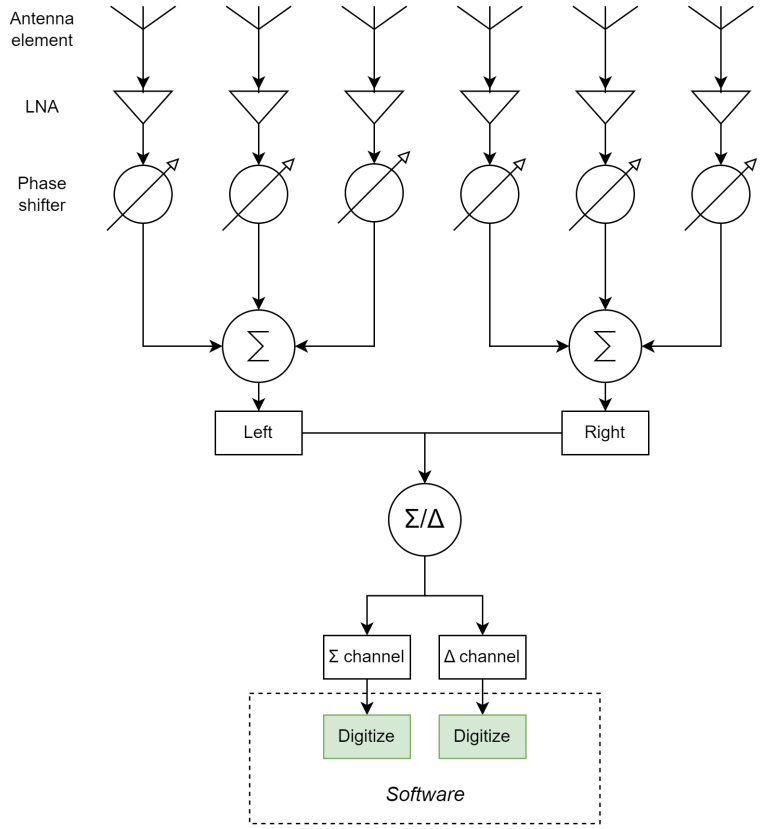

Figure 2.8: A two-channel Σ/Δ system with six antenna elements. After shifting the phase of the signals in each element, they are then combined into a left and right part. These signals are then added to and subtracted from each other, respectively, creating the Σ and Δ channels. These two channels are then digitized.

The normalized beam pattern for element n can be denoted $B_n(\theta)$. Assuming N is an even number of antenna elements, the beam patterns for the left and right parts are given by

$$\begin{cases} B_{\text{Left}}(\theta) = \sum_{n=1}^{\frac{N}{2}} B_n(\theta), \\ B_{\text{Right}}(\theta) = \sum_{n=\frac{N}{2}+1}^{N} B_n(\theta). \end{cases}$$

From these two halves, the beam pattern for the so-called sum and difference channels Σ and Δ can then be obtained according to

$$\begin{cases} B_\Sigma(\theta) = B_{\text{Right}}(\theta) + B_{\text{Left}}(\theta), \\ B_\Delta(\theta) = B_{\text{Right}}(\theta) - B_{\text{Left}}(\theta). \end{cases} \tag{2.7}$$

These two channels are then digitized, thus moving the processing from hardware to software. For a receiving antenna, it is then possible to detect a signal in both the Σ and Δ channels independently.

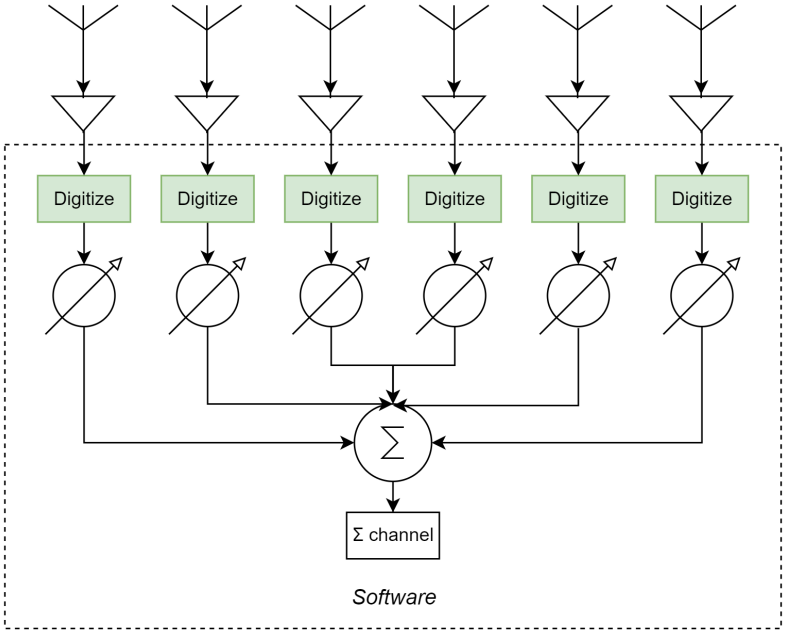

Figure 2.9: A multi-channel system where six antenna elements are individually digitized. Moving the phase shifters from hardware to software enables the possibility to control multiple independent beams simultaneously.

There are, however, other alternatives. Instead of only having two digital channels, there is a possibility to digitize all antenna elements individually [7], [22]. An illustration of such a multi-channel system can be seen in Figure 2.9. Notably, this moves the phase shifters to a software environment. The enables digital beamforming, where the antenna can control multiple independent beams simultaneously. Since the beams can have separate directions, this allows for simultaneous coverage of larger areas. This is in contrast to the analog beamforming used in the Σ/Δ system, where the different beam positions must be stepped through one by one. Note that the multiple simultaneous Σ channels makes reception in a Δ channel redundant in this case.

Instead of using the digital phase shifters to obtain maximum constructive interference in a predetermined direction, the signals in the antenna elements can be combined in different linear combinations. The optimal linear combination, or weighting, of the elements can be obtained be using statistics from the received data [6]. This is known as adaptive beamforming and is explored in more detail in the following section.

2.6 Beamforming

After describing the technical aspects of an SSR system, the beamforming concept introduced earlier is now analyzed in greater detail.

Assume a plane wave arriving at a ULA with N elements. The wavenumber vector,

$\boldsymbol{k}$, corresponds to the spatial frequency of an incoming wave. It can be defined as

$$\boldsymbol{k} = \frac{2\pi}{\lambda}\hat{\boldsymbol{u}},$$

where λ is the wavelength of the wave and $\hat{\boldsymbol{u}} = -(\sin\theta\cos\phi\hat{\boldsymbol{x}} + \cos\theta\cos\phi\hat{\boldsymbol{y}} + \sin\phi\hat{\boldsymbol{z}})$ is a unit vector in the direction of arrival [5], [6]. For a specific wavenumber, the steering vector, $\boldsymbol{v}(\boldsymbol{k}) \in \mathbb{C}^N$, describes how the plane wave propagates across the ULA, resulting in a phase shift between the signals in the different elements. The nth element of the steering vector is given by

$$[\boldsymbol{v}(\boldsymbol{k})]_n = \exp(-i\boldsymbol{k}^{\mathrm{T}}\boldsymbol{p}_n),$$

where $\boldsymbol{p}_n$ is the position for element n. Moreover, the weight vector, $\boldsymbol{w} \in \mathbb{C}^N$, describes how the signal is processed after reaching the array. It adjusts the phase and amplitude of the signals received by each antenna element. The choice of $\boldsymbol{w}$ depends on the type of beamforming.

From the definition of the steering vector and the weight vector, the beam pattern first mentioned in Section 2.5 can be defined as

$$B(\boldsymbol{k}) = \boldsymbol{w}^{\mathrm{H}}\boldsymbol{v}(\boldsymbol{k}). \tag{2.8}$$

Note that the beam pattern can be seen as the Fourier transform of the array response, $b(t)$ [6]. This can be seen by analyzing the time-domain signal

$$b(t) = \sum_{n=1}^{N} w_n^{\mathrm{H}}\delta(t - t_n),$$

where t_n is the relative time delay for the incoming wave at element n and $\delta(t)$ is the Dirac delta function or unit impulse. Shifting to the frequency domain with a Fourier transform gives

$$B(\omega) = \mathcal{F}[b(t)] = \sum_{n=1}^{N} w_n^{\mathrm{H}}\exp(-i\omega t_n).$$

Note that the time delay can be written as

$$t_n = \frac{\hat{\boldsymbol{u}}^{\mathrm{T}}\boldsymbol{p}_n}{c},$$

where c is the velocity of propagation for the wave. Moreover, the angular frequency can be written as $\omega = 2\pi c/\lambda$. Combining these expressions yields

$$\omega t_n = \frac{2\pi c}{\lambda}\frac{\hat{\boldsymbol{u}}^{\mathrm{T}}\boldsymbol{p}_n}{c} = \boldsymbol{k}^{\mathrm{T}}\boldsymbol{p}_n.$$

The beam pattern can now be written as

$$B(\omega) = B(\boldsymbol{k}) = \sum_{n=1}^{N} w_n^{\mathrm{H}}\exp(-i\boldsymbol{k}^{\mathrm{T}}\boldsymbol{p}_n) = \boldsymbol{w}^{\mathrm{H}}\boldsymbol{v}(\boldsymbol{k}),$$

as stated in Equation (2.8). Recall that for a ULA located on the x axis, the position vector can be written as

$$\boldsymbol{p}_n = \left(n - \frac{N+1}{2}\right) d\hat{\boldsymbol{x}}.$$

Assuming the horizontal cut $\phi = 0$, this results in the steering vector

$$[\boldsymbol{v}(\theta)]_n = \exp\left[i\frac{2\pi}{\lambda}\sin\theta\left(n - \frac{N+1}{2}\right)d\right].$$

Observe that the phase shift between the adjacent elements is in accordance with Equation (2.3). The beam pattern can then be written as a function of azimuth according to

$$B(\theta) = \boldsymbol{w}^{\mathrm{H}}\boldsymbol{v}(\theta).$$

As mentioned in Section 2.5, the beam pattern is a useful characteristic for an array antenna as it directly relates to the gain by $G(\theta) \propto |B(\theta)|^2$.

2.6.1 Conventional beamforming

There are different ways to choose the weight vector $\boldsymbol{w}$. In conventional beamforming, the weights are fixed and do not depend on any information from the received signal. The weights are chosen to generate maximum constructive interference between the elements in a given beam position θ_0. In a phased array, this is achieved by shifting the phase for the signals in each element by a proper amount [6]. Consequently, the signals received in each element can be added coherently. This corresponds to defining the weight vector as the steering vector for the antenna, evaluated at the beam position, according to

$$\boldsymbol{w} = \boldsymbol{v}(\theta_0). \tag{2.9}$$

For a ULA, the beam pattern is then given by

$$B(\theta) = \boldsymbol{w}^{\mathrm{H}}\boldsymbol{v}(\theta) = \boldsymbol{v}^{\mathrm{H}}(\theta_0)\boldsymbol{v}(\theta) =$$

$$= \sum_{n=1}^{N} \exp\left[-i\frac{2\pi}{\lambda}\sin\theta_0\left(n - \frac{N+1}{2}\right)d\right]\exp\left[i\frac{2\pi}{\lambda}\sin\theta\left(n - \frac{N+1}{2}\right)d\right] =$$

$$= \sum_{n=1}^{N} \exp\left[i\frac{2\pi}{\lambda}(\sin\theta - \sin\theta_0)\left(n - \frac{N+1}{2}\right)d\right] =$$

$$= \exp[i(\varphi_1(\theta) - \varphi_1(\theta_0))] + \exp[i(\varphi_2(\theta) - \varphi_2(\theta_0))] + \cdots + \exp[i(\varphi_N(\theta) - \varphi_N(\theta_0))],$$

where $\varphi_1, \varphi_2, \ldots, \varphi_N$ are the phases in the different elements. As expected, the magnitude of the sum above has its maximum value for $\theta = \theta_0$. Figure 2.10 displays normalized example beam patterns illustrating this, with the case $\theta_0 = 0°$ shown in Figure 2.10(a) and a contour plot for θ_0 ranging from $-90°$ to $90°$ shown in Figure 2.10(b).

It can be noted that the beam pattern not only has a peak for $\theta = \theta_0$, the main lobe, but also smaller peaks symmetrically placed around it, the sidelobes. Sidelobes

are a characteristic feature of directional antennas and a direct consequence of the antenna geometry [6].

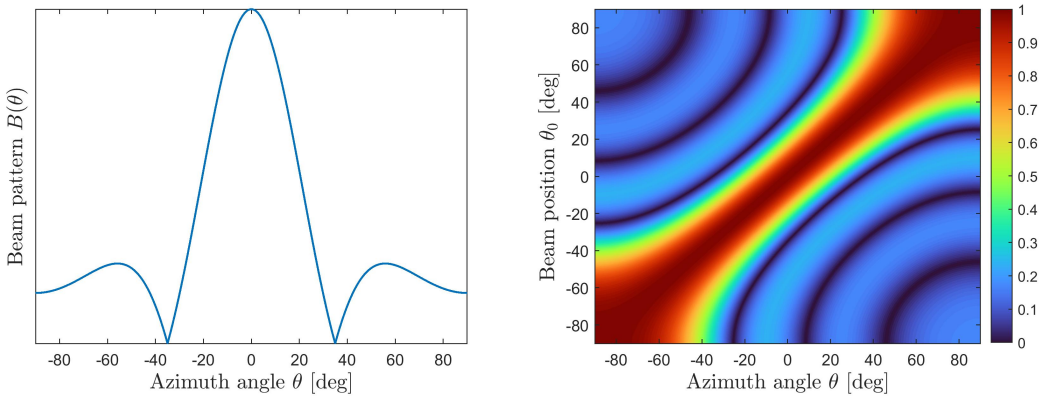

(a) **(b)**

Figure 2.10: Example beam patterns with conventional beamforming. Note that this corresponds to the Σ channel in a Σ/Δ system. **(a)** The case $\theta_0 = 0°$. **(b)** Contour plot for θ_0 ranging from $-90°$ to $90°$.

Note that in the case of a Σ/Δ system described in Section 2.5, the definition of $\boldsymbol{w}$ in Equation (2.9) only holds for the Σ channel. For the Δ channel, the beam pattern of first half of the elements, B_{Left}, should be subtracted from the second half, B_{Right}, according to Equation (2.7). Therefore, the nth component of the weight vector can in this case be defined according to

$$[\boldsymbol{w}]_n = \begin{cases} -[\boldsymbol{v}(\theta_0)]_n & \text{if } n = 1, \ldots, N/2 \\ +[\boldsymbol{v}(\theta_0)]_n & \text{if } n = N/2+1, \ldots, N \end{cases} = (-1)^{n \leq N/2} [\boldsymbol{v}(\theta_0)]_n.$$

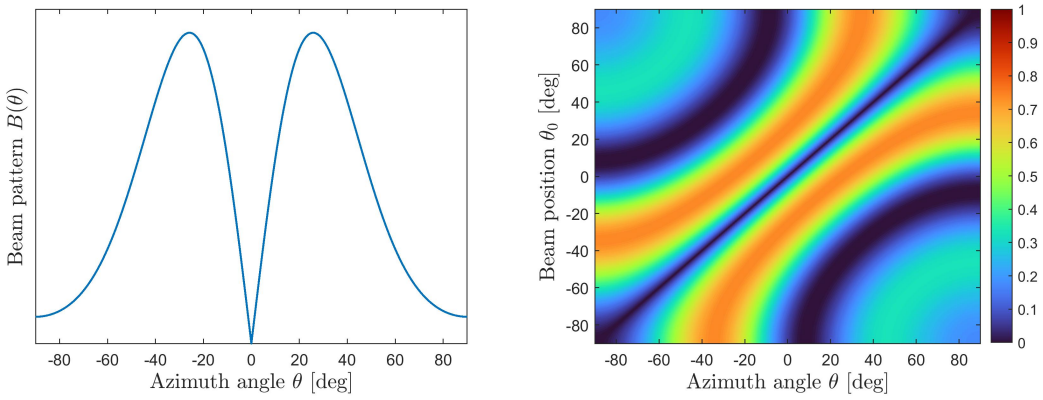

(a) **(b)**

Figure 2.11: Example beam patterns with conventional beamforming for the Δ channel in a Σ/Δ system. **(a)** The case $\theta_0 = 0$. **(b)** Contour plot for θ_0 ranging from $-90°$ to $90°$.

Figure 2.11 displays normalized example beam patterns for the Δ channel, similar to ones shown in Figure 2.10. Note that the beam pattern has its minimum for the beam position $\theta = \theta_0$.

Note that conventional beamforming can be either analog or digital. As described in Section 2.5, the Σ/Δ system applies analog beamforming. The multi-channel system, on the other hand, digitizes the phase shifters and consequently applies digital beamforming.

2.6.2 Adaptive beamforming

In the case of conventional beamforming described above, the beam positions, and therefore weights $\boldsymbol{w}$, are fixed. Despite its simplicity, conventional beamforming has its limitations. One significant disadvantage is that it does not account for interfering signals. If an interfering signal is present at a main lobe or sidelobe in the beam pattern, there is a risk of this signal being amplified at the expense of the SOI.

Moreover, the coverage is limited given a finite number of beam positions. Even in the case of digital beamforming, where it is possible to control multiple beams with different θ_0 simultaneously, there is a decrease in amplitude between the different beams. In a scenario where an SOI is located in such a gap, this could impair the probability to detect it.

For data-dependent beamforming, or adaptive beamforming, the complex weights are instead determined by optimizing a certain quantity based on the input data [6]. As indicated by the name, these beamformers can adapt to different signal scenarios, including accounting for interfering signals.

As previously stated, the optimal weights are calculated using input data to the system. However, before analyzing the incoming data, optimal beamformers must be derived. In this thesis, three different optimal beamformers are analyzed: The minimum power distortionless response (MPDR) beamformer, followed by two different modifications of it: the linear constraint minimum power (LCMP) beamformer and the principal component (PC) beamformer.

2.6.2.1 MPDR beamformer

In the MPDR beamformer, the goal is to minimize the total received power, while maintaining a distortionless response in the direction of the SOI [5], [6]. In the time domain, the received signal in each element can be written as $\boldsymbol{x}(t) \in \mathbb{C}^N$. After processing this signal with weights, $\boldsymbol{w}$, the output signal, $y(t)$, is given by

$$y(t) = \boldsymbol{w}^{\mathrm{H}}\boldsymbol{x}(t).$$

The total output power can then, per definition, be obtained as the expected value of the squared magnitude of $y(t)$ according to

$$P_{\text{out}} = \mathbb{E}[|y|^2] = \mathbb{E}[|\boldsymbol{w}^{\mathrm{H}}\boldsymbol{x}|^2] = \mathbb{E}[\boldsymbol{w}^{\mathrm{H}}\boldsymbol{x}\boldsymbol{x}^{\mathrm{H}}\boldsymbol{w}] = \boldsymbol{w}^{\mathrm{H}}\mathbb{E}[\boldsymbol{x}\boldsymbol{x}^{\mathrm{H}}]\boldsymbol{w}.$$

It is now convenient to define the signal covariance matrix between the different antenna elements as

$$\boldsymbol{R}_x = \mathbb{E}[\boldsymbol{x}\boldsymbol{x}^{\mathrm{H}}].$$

This matrix captures the statistical properties of the received signal, and plays an important role in adaptive beamforming. The output power can therefore be written as $P_{\text{out}} = \boldsymbol{w}^{\mathrm{H}}\boldsymbol{R}_x\boldsymbol{w}$.

To maintain a distortionless response in the desired direction of arrival, θ_{SOI}, a constraint of unit gain in this direction can be imposed, according to $\boldsymbol{w}^{\mathrm{H}}\boldsymbol{v}(\theta_{\text{SOI}}) = 1$. This leads to the optimization problem

$$\begin{cases} \min\limits_{\boldsymbol{w}} & \boldsymbol{w}^{\mathrm{H}}\boldsymbol{R}_x\boldsymbol{w} \\ \text{s.t.} & \boldsymbol{w}^{\mathrm{H}}\boldsymbol{v}(\theta_{\text{SOI}}) = 1. \end{cases}$$

This problem can be solved using complex Lagrangian relaxation. Introducing Lagrangian parameter $\lambda_{\mathcal{L}}$, this gives

$$\mathcal{L}(\boldsymbol{w}, \lambda_{\mathcal{L}}) = \boldsymbol{w}^{\mathrm{H}}\boldsymbol{R}_x\boldsymbol{w} + \lambda_{\mathcal{L}}(\boldsymbol{w}^{\mathrm{H}}\boldsymbol{v}(\theta_{\text{SOI}}) - 1) + \lambda_{\mathcal{L}}^{\mathrm{H}}(\boldsymbol{v}^{\mathrm{H}}(\theta_{\text{SOI}})\boldsymbol{w} - 1).$$

Note that the conjugate of the constraint is included, since this complex optimization problem effectively has two constraints: one for the real part and one for the imaginary. Also note that $\boldsymbol{w}$ and $\boldsymbol{w}^{\mathrm{H}}$ can be treated as two independent variables. More details about the complex optimization are explained in Appendix A.1. Taking the complex gradient with respect to $\boldsymbol{w}$ gives

$$\nabla_{\boldsymbol{w}}\mathcal{L}(\boldsymbol{w}, \lambda_{\mathcal{L}}) = \boldsymbol{w}^{\mathrm{H}}\boldsymbol{R}_x + \lambda_{\mathcal{L}}^{\mathrm{H}}\boldsymbol{v}^{\mathrm{H}}(\theta_{\text{SOI}}) = \boldsymbol{0}.$$

Solving for $\boldsymbol{w}^{\mathrm{H}}$ gives

$$\boldsymbol{w}^{\mathrm{H}} = -\lambda_{\mathcal{L}}^{\mathrm{H}}\boldsymbol{v}^{\mathrm{H}}(\theta_{\text{SOI}})\boldsymbol{R}_x^{-1}.$$

Note that the constraint now can be written as

$$\boldsymbol{w}^{\mathrm{H}}\boldsymbol{v}(\theta_{\text{SOI}}) = -\lambda_{\mathcal{L}}^{\mathrm{H}}\boldsymbol{v}^{\mathrm{H}}(\theta_{\text{SOI}})\boldsymbol{R}_x^{-1}\boldsymbol{v}(\theta_{\text{SOI}}) = 1,$$

resulting in

$$\lambda_{\mathcal{L}}^{\mathrm{H}} = -\frac{1}{\boldsymbol{v}^{\mathrm{H}}(\theta_{\text{SOI}})\boldsymbol{R}_x^{-1}\boldsymbol{v}(\theta_{\text{SOI}})}.$$

Note that $\boldsymbol{v}^{\mathrm{H}}(\theta_{\text{SOI}})\boldsymbol{R}_x^{-1}\boldsymbol{v}(\theta_{\text{SOI}})$ is a quadratic form and therefore a scalar. The optimal weight vector can now be written as

$$\boldsymbol{w}^{\mathrm{H}} = \frac{\boldsymbol{v}^{\mathrm{H}}(\theta_{\text{SOI}})\boldsymbol{R}_x^{-1}}{\boldsymbol{v}^{\mathrm{H}}(\theta_{\text{SOI}})\boldsymbol{R}_x^{-1}\boldsymbol{v}(\theta_{\text{SOI}})}. \tag{2.10}$$

By applying this weight, interfering signals can be suppressed using the information encoded in the covariance matrix $\boldsymbol{R}_x$, while the imposed constraint enables unit gain in the direction of the signal of interest [6]. Note that the numerator in Equation (2.10) describes the phase relation between the signals in the different elements when applying the weights. The denominator is effectively a constant scaling factor.

2.6.2.2 LCMP beamformer

There are several ways to generalize and develop the MPDR beamformer. One alternative is to include more linear constraints in the optimization problem. This leads to the linear constraint minimum power (LCMP) beamformer [6]. For N_c number of constraints, the problem can be written as

$$\begin{cases} \min\limits_{\boldsymbol{w}} & \boldsymbol{w}^\mathrm{H}\boldsymbol{R}_x\boldsymbol{w} \\ \text{s.t.} & \boldsymbol{w}^\mathrm{H}\boldsymbol{C} = \boldsymbol{g}^\mathrm{H}, \end{cases}$$

where $\boldsymbol{C} \in \mathbb{C}^{N\times N_\mathrm{c}}$ is a constraint matrix and $\boldsymbol{g} \in \mathbb{C}^{N_\mathrm{c}}$ is a vector representing the signal gains set by the constraints.

Following the same steps as in previous section, the Lagrangian can now be written as

$$\mathcal{L}(\boldsymbol{w}, \lambda_\mathcal{L}) = \boldsymbol{w}^\mathrm{H}\boldsymbol{R}_x\boldsymbol{w} + \lambda_\mathcal{L}(\boldsymbol{w}^\mathrm{H}\boldsymbol{C} - \boldsymbol{g}^\mathrm{H}) + \lambda_\mathcal{L}^\mathrm{H}(\boldsymbol{C}^\mathrm{H}\boldsymbol{w} - \boldsymbol{g}).$$

The complex gradient with respect to $\boldsymbol{w}$ gives

$$\nabla_{\boldsymbol{w}}\mathcal{L}(\boldsymbol{w}, \lambda_\mathcal{L}) = \boldsymbol{w}^\mathrm{H}\boldsymbol{R}_x + \lambda_\mathcal{L}^\mathrm{H}\boldsymbol{C}^\mathrm{H} = \boldsymbol{0}.$$

Solving for $\boldsymbol{w}^\mathrm{H}$ gives

$$\boldsymbol{w}^\mathrm{H} = -\lambda_\mathcal{L}^\mathrm{H}\boldsymbol{C}^\mathrm{H}\boldsymbol{R}_x^{-1},$$

resulting in

$$\boldsymbol{w}^\mathrm{H}\boldsymbol{C} = -\lambda_\mathcal{L}^\mathrm{H}\boldsymbol{C}^\mathrm{H}\boldsymbol{R}_x^{-1}\boldsymbol{C} = \boldsymbol{g}^\mathrm{H},$$

and

$$\lambda_\mathcal{L}^\mathrm{H} = -\boldsymbol{g}^\mathrm{H}(\boldsymbol{C}^\mathrm{H}\boldsymbol{R}_x^{-1}\boldsymbol{C})^{-1}.$$

The optimal LCMP weights are therefore given by

$$\boldsymbol{w}^\mathrm{H} = \boldsymbol{g}^\mathrm{H}(\boldsymbol{C}^\mathrm{H}\boldsymbol{R}_x^{-1}\boldsymbol{C})^{-1}\boldsymbol{C}^\mathrm{H}\boldsymbol{R}_x^{-1}.$$

In the case of imposing direct constraints on the gain for an SOI and D interfering signals, the constraint matrix can be written as

$$\boldsymbol{C} = \begin{bmatrix} \boldsymbol{v}(\theta_\mathrm{SOI}) & \boldsymbol{v}(\theta_1) & \boldsymbol{v}(\theta_2) & \dots & \boldsymbol{v}(\theta_D) \end{bmatrix},$$

where θ_SOI is the direction of arrival for the SOI and $\theta_1, \theta_2, \dots, \theta_D$ are the directions of arrival for the D interfering signals. For example, imposing a unit gain constraint for the SOI and null constraints for the interfering signals gives $\boldsymbol{g} = \begin{bmatrix} 1 & 0 & 0 & \dots & 0 \end{bmatrix}^\mathrm{T}$.

2.6.2.3 PC beamformer

Another variation of the MPDR is the principal component (PC) beamformer [6]. The idea here is to perform an eigendecomposition of $\boldsymbol{R}_x$ according to

$$\boldsymbol{R}_x = \boldsymbol{U}\boldsymbol{\Lambda}\boldsymbol{U}^\mathrm{H} = \sum_{i=1}^{N} \lambda_i \boldsymbol{\Phi}_i \boldsymbol{\Phi}_i^\mathrm{H},$$

where $\boldsymbol{U}$ is an $N \times N$ matrix with $\boldsymbol{R}_x$ eigenvectors $\boldsymbol{\Phi}_i$ as columns, and $\boldsymbol{\Lambda}$ is a diagonal matrix with corresponding eigenvalues λ_i. Since $\boldsymbol{R}_x$ is symmetric, its inverse is given by

$$\boldsymbol{R}_x^{-1} = \boldsymbol{U}\boldsymbol{\Lambda}^{-1}\boldsymbol{U}^{\mathrm{H}} = \sum_{i=1}^{N} \frac{1}{\lambda_i}\boldsymbol{\Phi}_i\boldsymbol{\Phi}_i^{\mathrm{H}}.$$

Using principal component analysis, it is then possible to reduce the dimensionality of the data by identifying the components with the largest variance contribution. This can be done by analyzing the eigenvalues λ_i. The eigenvectors with the largest corresponding eigenvalues represent the directions in which the data has its largest variance. Note that the variance reflects the signal power of the different components.

For the case with an SOI and D interfering signals, the principal components can be chosen as the eigenvectors with the $D+1$ largest corresponding eigenvalues. From this, the signal-plus-interference subspace can be defined as the vector space spanned by the eigenvectors of the principal components, according to

$$\boldsymbol{U}_{\mathrm{S+I}} = \begin{bmatrix} \boldsymbol{\Phi}_1 & \boldsymbol{\Phi}_2 & \dots & \boldsymbol{\Phi}_{D+1} \end{bmatrix}.$$

Similarly, the noise subspace can be defined as the span of the remaining eigenvectors, corresponding to the $N-(D+1)$ smallest eigenvalues. Note that for the noise subspace to be non-trivial, this requires $D+1 < N$. Assuming the noise is uncorrelated to the signals, the eigendecomposition of $\boldsymbol{R}_x^{-1}$ can now be written as

$$\boldsymbol{R}_x^{-1} = \boldsymbol{U}_{\mathrm{S+I}}\boldsymbol{\Lambda}_{\mathrm{S+I}}^{-1}\boldsymbol{U}_{\mathrm{S+I}}^{\mathrm{H}} + \boldsymbol{U}_{\mathrm{noise}}\boldsymbol{\Lambda}_{\mathrm{noise}}^{-1}\boldsymbol{U}_{\mathrm{noise}}^{\mathrm{H}}.$$

Because of the symmetry of $\boldsymbol{R}_x$, its eigenvectors are orthogonal. This implies that the signal-plus-interference subspace and the noise subspace are orthogonal complements. Since the signal steering vector $\boldsymbol{v}(\theta_{\mathrm{SOI}})$ belong to the signal-plus-interference subspace, $\boldsymbol{v}^{\mathrm{H}}(\theta_{\mathrm{SOI}})\boldsymbol{\Phi}_i = 0$ for $i = D+2, \dots, N$. Consequently, the MPDR weights in Equation (2.10) can be reduced to

$$\boldsymbol{w}^{\mathrm{H}} = \frac{\boldsymbol{v}^{\mathrm{H}}(\theta_{\mathrm{SOI}})\boldsymbol{U}_{\mathrm{S+I}}\boldsymbol{\Lambda}_{\mathrm{S+I}}^{-1}\boldsymbol{U}_{\mathrm{S+I}}^{\mathrm{H}}}{\boldsymbol{v}^{\mathrm{H}}(\theta_{\mathrm{SOI}})\boldsymbol{U}_{\mathrm{S+I}}\boldsymbol{\Lambda}_{\mathrm{S+I}}^{-1}\boldsymbol{U}_{\mathrm{S+I}}^{\mathrm{H}}\boldsymbol{v}(\theta_{\mathrm{SOI}})} = \left(\frac{\boldsymbol{v}_{\mathrm{S+I}}^{\mathrm{H}}(\theta_{\mathrm{SOI}})\boldsymbol{\Lambda}_{\mathrm{S+I}}^{-1}}{\boldsymbol{v}_{\mathrm{S+I}}^{\mathrm{H}}(\theta_{\mathrm{SOI}})\boldsymbol{\Lambda}_{\mathrm{S+I}}^{-1}\boldsymbol{v}_{\mathrm{S+I}}(\theta_{\mathrm{SOI}})}\right)\boldsymbol{U}_{\mathrm{S+I}}^{\mathrm{H}},$$

where $\boldsymbol{v}_{\mathrm{S+I}}(\theta_{\mathrm{SOI}}) = \boldsymbol{U}_{\mathrm{S+I}}^{\mathrm{H}}\boldsymbol{v}(\theta_{\mathrm{SOI}})$ is steering vector projected to the lower-dimensional signal-plus-interference subspace. In conclusion, the PC beamformer can be seen as a projection of the incoming signals into a $(D+1)$-dimensional subspace containing sufficient information to obtain the optimal weights $\boldsymbol{w}$. This reduction in dimensionality can be computationally beneficial.

2.7 Estimation of parameters

In the previous section, optimal beamformers are derived. In order to implement these in practice, several parameters need to be estimated from the input data. This includes the signal covariance matrix, $\boldsymbol{R}_x$, and the directions of arrival, θ.

2.7.1 Covariance matrix

In practical applications, the signal covariance matrix $\boldsymbol{R}_x$ has to be replaced by an estimate $\hat{\boldsymbol{R}}_x$. To this end, the sample matrix inversion (SMI) method can be applied [5], [6]. Assume K number of N-dimensional discrete time samples $\boldsymbol{x}_1, \boldsymbol{x}_2, \ldots, \boldsymbol{x}_K$, independently sampled from a complex normal distribution with zero mean and covariance matrix $\boldsymbol{R}_x$, $\boldsymbol{x} \sim \mathcal{CN}(\boldsymbol{0}, \boldsymbol{R}_x)$. The joint probability density, corresponding to the likelihood function, is then given by

$$\mathcal{L}(\boldsymbol{R}_x) = \prod_{k=1}^{K} \frac{1}{\pi^N \det(\boldsymbol{R}_x)} \exp(-\boldsymbol{x}_k^{\mathrm{H}} \boldsymbol{R}_x^{-1} \boldsymbol{x}_k),$$

in accordance with Equation (2.6). This results in the log-likelihood

$$\log \mathcal{L} = -K \log \det(\boldsymbol{R}_x) - \sum_{k=1}^{K} \boldsymbol{x}_k^{\mathrm{H}} \boldsymbol{R}_x^{-1} \boldsymbol{x}_k + \text{const} =$$

$$= -K \log \det(\boldsymbol{R}_x) - \operatorname{tr}\left(\boldsymbol{R}_x^{-1} \sum_{k=1}^{K} \boldsymbol{x}_k \boldsymbol{x}_k^{\mathrm{H}} \right) + \text{const}.$$

Note that the cyclic property of the trace is applied here. Using derivative operations for matrices, the matrix gradient of the log-likelihood is then given by

$$\nabla_{\boldsymbol{R}_x} \log \mathcal{L} = -K (\boldsymbol{R}_x^{-1})^{\mathrm{T}} + \left(\boldsymbol{R}_x^{-1} \sum_{k=1}^{K} \boldsymbol{x}_k \boldsymbol{x}_k^{\mathrm{H}} \boldsymbol{R}_x^{-1} \right)^{\mathrm{T}} = \boldsymbol{0}.$$

Solving for $\boldsymbol{R}_x$ then gives the maximum likelihood estimator

$$\hat{\boldsymbol{R}}_x = \frac{1}{K} \sum_{k=1}^{K} \boldsymbol{x}_k \boldsymbol{x}_k^{\mathrm{H}}.$$

Assuming an ergodic stochastic process, the time sample average above converges to the ensemble average $\mathbb{E}[\boldsymbol{x}\boldsymbol{x}^{\mathrm{H}}]$ as the number of samples increases. Therefore, $\hat{\boldsymbol{R}}_x$ converges to $\boldsymbol{R}_x$ as $K \to \infty$.

2.7.2 Directions of arrival

The derived formulas for the weights not only depend on the covariance matrix, but also on the steering vectors for the SOI and the interfering signals. Given that the antenna geometry and the wavelength of the incident waves are known, the only unknown parameter in the steering vector is the direction of arrival (DOA).

One algorithm commonly used to estimate DOAs is ESPRIT (Estimation of signal parameter via rotational invariance techniques). Like the PC beamformer derived in Section 2.6.2.3, this algorithm exploits the fact that the received signals can be decomposed into a signal-plus-interference subspace and a noise subspace [6]. Following this, the signal-plus-interference subspace can be divided into two subarray subspaces, $\boldsymbol{U}_1$, containing the first $N-1$ antenna elements, and $\boldsymbol{U}_2$, containing the last $N-1$ elements. A similar division can be made for the steering vectors. If

$\boldsymbol{V}$ denotes the matrix containing the steering vectors, $\boldsymbol{V}_1$ and $\boldsymbol{V}_2$ represent the steering vector matrices for the two subarrays. Since the steering vectors span the signal-plus-interference subspace, this gives

$$\begin{cases} \boldsymbol{U}_1 = \boldsymbol{V}_1\boldsymbol{T}, \\ \boldsymbol{U}_2 = \boldsymbol{V}_2\boldsymbol{T}, \end{cases}$$

where $\boldsymbol{T} \in \mathbb{C}^{(D+1)\times(D+1)}$ is a non-singular matrix. In other words, the steering vectors can be expressed as a linear combination of the eigenvectors of the covariance matrix, which span the signal-plus-interference subspace. Moreover, the fact that there is a constant phase shift between the elements can be utilized by writing $\boldsymbol{V}_2 = \boldsymbol{V}_1\boldsymbol{\Delta\Phi}$, where $\boldsymbol{\Delta\Phi}$ is a diagonal matrix containing the phase shift between the elements for the different signals according to

$$\boldsymbol{\Delta\Phi} = \operatorname{diag}\begin{bmatrix} \exp(i\Delta\varphi_1) & \exp(i\Delta\varphi_2) & \dots & \exp(i\Delta\varphi_{D+1}) \end{bmatrix}.$$

Recall that the phase shift between adjacent elements is given by

$$\Delta\varphi_i = \frac{2\pi d \sin\theta_i}{\lambda}.$$

Combining these expressions, this results in

$$\boldsymbol{U}_2 = \boldsymbol{V}_2\boldsymbol{T} = \boldsymbol{V}_1\boldsymbol{\Delta\Phi}\boldsymbol{T} = \boldsymbol{U}_1\boldsymbol{T}^{-1}\boldsymbol{\Delta\Phi}\boldsymbol{T}.$$

Defining $\boldsymbol{P} = \boldsymbol{T}^{-1}\boldsymbol{\Delta\Phi}\boldsymbol{T}$, eigencomposition gives that $\boldsymbol{\Delta\Phi}$ contains the eigenvalues of $\boldsymbol{P}$. By solving $\boldsymbol{U}_2 = \boldsymbol{U}_1\boldsymbol{P}$ and computing the eigenvalues of $\boldsymbol{P}$, the directions of arrival, θ_i, can therefore be estimated. The equation can for example be solved using the method of least squares, yielding

$$\boldsymbol{P} = (\boldsymbol{U}_1^{\mathrm{H}}\boldsymbol{U}_1)^{-1}\boldsymbol{U}_1^{\mathrm{H}}\boldsymbol{U}_2.$$

The full ESPRIT algorithm can be seen in Algorithm 1 below.

Algorithm 1 ESPRIT algorithm for DOA estimation

1: Collect measurements $\boldsymbol{x}_1, \boldsymbol{x}_2, \dots, \boldsymbol{x}_K$.
2: Estimate the covariance matrix $\hat{\boldsymbol{R}}_x$.
3: Perform eigendecomposition on $\hat{\boldsymbol{R}}_x$ according to $\hat{\boldsymbol{R}}_x = \boldsymbol{U}\boldsymbol{\Lambda}\boldsymbol{U}^{\mathrm{H}}$.
4: Find the signal-plus-interference subspace $\boldsymbol{U}_{\mathrm{S+I}}$.
5: Define $\boldsymbol{U}_1$ and $\boldsymbol{U}_2$ as the first and last $N-1$ rows of $\boldsymbol{U}_{\mathrm{S+I}}$, respectively.
6: Solve $\boldsymbol{U}_2 = \boldsymbol{U}_1\boldsymbol{P}$ for $\boldsymbol{P}$.
7: Calculate eigenvalues $\lambda_1, \lambda_2, \dots, \lambda_{D+1}$ of $\boldsymbol{P}$.
8: Obtain the phase shift from $\lambda_i = \exp(i\Delta\varphi_i) \Rightarrow \Delta\varphi_i = \arg\lambda_i$.
9: Calculate the DOA from $\Delta\varphi_i = 2\pi d\sin\theta_i/\lambda \Rightarrow \theta_i = \arcsin[\lambda\Delta\varphi_i/(2\pi d)]$.

Note that the implementation of this algorithm requires knowledge of the number of signals. This could for example be estimated by analyzing the eigenvalues of the covariance matrix, corresponding to the signal power, and require that their magnitude should be above some threshold.

3

Implementation

This chapter describes the different methods used in this thesis, based on the theory described in the previous chapter. It should be mentioned that no real data has been used in this project, but it has rather been generated using the theoretical models and approximations described below. Recall that the aim here is to estimate the probability of detection for ADS-B signals for different interference scenarios. This is done for digital multi-channel systems applying conventional as well as adaptive beamforming. The results are benchmarked against a two-channel Σ/Δ system using analog conventional beamforming.

3.1 Environment model

The simulations are performed in a square grid of area $A_{\text{grid}} = 10^6$ km^2. The spatial resolution is set to $A_{\text{pixel}} = 10 \times 10$ km^2, hence a grid consisting of 10,000 pixels. An example, with fewer pixels, is seen Figure 3.1. In the simulations, all pixels in the grid are systematically iterated over and a target of interest, i.e., an ADS-B signal, is assumed to be located in each pixel. The airborne SSR radar is assumed to be located at the origin.

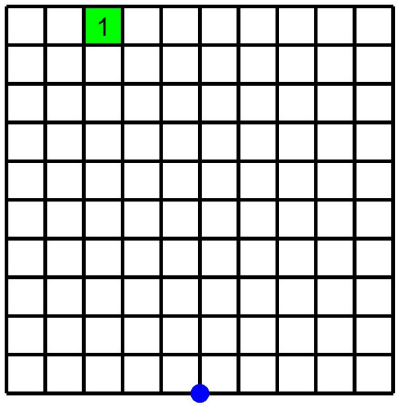

Figure 3.1: An example square grid. Note that this grid only has 100 pixels, compared to 10,000 pixels used in the simulations. The SSR, marked in blue, is placed at the origin. The green pixel with a "1" indicates that a target, in this case, has successfully been detected here.

The maximum distance limited by the horizon is set to 900 km. This is based on an approximation that the radar is placed on a platform flying at an altitude of $h = 12$ km. If two aircraft are at altitude h, the maximum possible line-of-sight distance, R_{LOS}, is given by

$$\left(\frac{R_{\text{LOS}}}{2}\right)^2 + (k_{\text{ar}} R_{\text{Earth}})^2 = (k_{\text{ar}} R_{\text{Earth}} + h)^2,$$

where $R_{\text{Earth}} \approx 6371$ km is the radius of the Earth [1]. Note that due to atmospheric refraction, radio waves are bent towards to surface of the Earth, thus increasing the effective radius by a factor k_{ar}. Assuming normal weather conditions, this factor is set to $k_{\text{ar}} = 4/3$ [23]. This gives

$$R_{\text{LOS}} = 2\sqrt{2k_{\text{ar}} R_{\text{Earth}} h + h^2} \approx 900 \text{ km}.$$

ADS-B signals are assumed to be transmitted at a rate of $f_{\text{squitter}} = 2$ Hz. The transponder output power is set to $P'_{\text{t,SOI}} = 21$ dBW ≈ 126 W. Note that this is the effective power transmitted from the transponders, including possible gains and internal losses. Similarly, the power from the interfering signals is set to $P'_{\text{t,int}} = 24$ dBW ≈ 251 W. This assumption is chosen to account for "pessimistic scenarios", such that the performance of the system is rather underestimated than overestimated. Regardless, the scenarios investigated remain realistic. The numbers are partly based on ICAO standards, regulating that the lowest allowed transponder output power is 24 dBW [4]. Hence, the effective power for the targets is chosen to include losses of 3 dB relative to the interfering signals.

In this study, the interfering signals are assumed to be Mode S Long and Mode S Short replies. As explained in Section 2.2, the number of interfering signals can be seen as a Poisson random variable. In this case, the Poisson parameters are $\lambda_{\text{Poi}}^{\text{long}} = t_{\text{Poi}}^{\text{long}} \mu_{\text{long}}$ and $\lambda_{\text{Poi}}^{\text{short}} = t_{\text{Poi}}^{\text{short}} \mu_{\text{short}}$. The time parameters are given by $t_{\text{Poi}}^{\text{long}} = t_{\text{ADS-B}} + t_{\text{int,long}} = 120 + 120$ µs $= 240$ µs and $t_{\text{Poi}}^{\text{short}} = t_{\text{ADS-B}} + t_{\text{int,short}} = 120 + 64$ µs $=$ 184 µs.

Analyzing the intensity of interfering signals, μ, the total number of interfering signals per second, this can be written as $\mu = \mu_{\text{t}} \rho A_{\text{grid}}$, where μ_{t} is the number of messages per individual transponder per second and ρ is the transponder density (number of transponders per km^2). Introducing $\gamma = \mu_{\text{t}} \rho$, this parameter describes the number of messages per second per km^2. Effectively, since γ is proportional to both the density of transponders and how often they transmit a message, this parameter can be thought of as a degree of disturbance.

In the simulations, the γ parameter ranges from $\gamma = 5 \times 10^{-3}$ s^{-1} km^{-2} to $\gamma = 2 \times 10^{-2}$ s^{-1} km^{-2}. This interval is chosen based on estimations on ρ and μ_{t}. Using Flightradar24, ρ is estimated to be in the order of 1×10^{-3} transponders per km^2 [24]. Note that this depends on the geographical location as well the air traffic at the given time. It is a bit challenging to estimate μ_{t} accurately, as it depends on several factors such as regulations for message rates and the number of interrogators covering the area. It is also affected by the fact that aircraft can interrogate each other through an airborne collision avoidance system (ACAS). Based on earlier

work, μ_t is estimated to be in the order of 10 messages per transponder per second [11], [12]. Consequently, γ is in the order of 1×10^{-2} s^{-1} km^{-2}. For simplicity, an equal distribution for Mode S Long and Mode S Short is assumed, meaning $\gamma_{\text{long}} = \gamma_{\text{short}} = \gamma/2$.

From this, three different values for γ are chosen: 5×10^{-3}, 1×10^{-2} and 2×10^{-2} s^{-1} km^{-2}. The corresponding Poisson parameter for Mode S Long replies are given by $\lambda_{\text{Poi}}^{\text{long}} = t_{\text{Poi}}^{\text{long}} \mu_{\text{long}} = t_{\text{Poi}}^{\text{long}} \gamma_{\text{long}} A_{\text{grid}}$. The calculation for Mode S Short is performed analogous to the one for Mode S Long. The different values for γ with corresponding Poisson parameters are shown in Table 3.1.

Table 3.1: The three different values used for the message rate per area γ, corresponding to the degree of disturbance. The corresponding Poisson parameters $\lambda_{\text{Poi}}^{\text{long}}$ and $\lambda_{\text{Poi}}^{\text{short}}$, describing the average number of received Mode S Long and Mode S Short replies, are also presented together with their sum.

γ [s^{-1} km^{-2}]	$\lambda_{\text{Poi}}^{\text{long}}$	$\lambda_{\text{Poi}}^{\text{short}}$	$\lambda_{\text{Poi}}^{\text{tot}}$
5×10^{-3}	0.60	0.46	1.06
1×10^{-2}	1.20	0.92	2.12
2×10^{-2}	2.40	1.84	4.24

The other parameters related to the environment model described above are summarized in Table 3.2 below.

Table 3.2: Values for the parameters used when modelling the physical environment experienced by the simulated SSR system. This includes geographical parameters as well as properties of the incoming signals.

Parameter	Notation	Value
Grid size	A_{grid}	1000×1000 km^2
Spatial resolution	A_{pixel}	10×10 km^2
Altitude	h	12 km
Maximum line-of-sight distance	R_{LOS}	900 km
Target effective output power	$P'_{\text{t,SOI}}$	21 dBW
Interfering target effective output power	$P'_{\text{t,int}}$	24 dBW
ADS-B squitter frequency	f_{squitter}	2 Hz
Duration of ADS-B signal	$t_{\text{ADS-B}}$	120 µs
Duration of Mode S Long reply	$t_{\text{int,long}}$	120 µs
Duration of Mode S Short reply	$t_{\text{int,short}}$	64 µs

3.2 Antenna model

A uniform linear array with $N = 6$ antenna elements is used in this model. The distance between the elements is set to $d = 80$ mm. For the cases where conventional beamforming is applied, a fixed set of seven beam positions are used, namely

$\begin{bmatrix}0° & \pm15° & \pm30° & \pm45°\end{bmatrix}$. Figure 3.2 displays beam patterns in polar coordinates for the different beam positions.

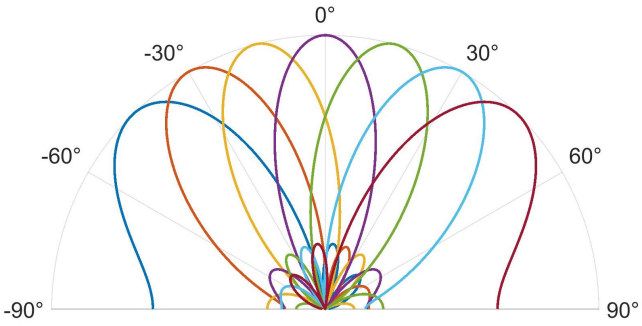

Figure 3.2: Beam patterns in polar coordinates for the seven different beam positions, 0°, ±15°, ±30° and ±45°, used for conventional beamforming.

The bandwidth of the system is set to $W = 10$ MHz. The simulated time is set to $t_{\text{sim}} = 1$ s. Note that in the case of analog beamforming, this corresponds to the sweep time, i.e., the time it takes for the antenna to step through the beam positions. The physical area of the antenna is approximated as $A_{\text{physical}} = ((N-1)d + d)^2 = (Nd)^2 \approx 0.23$ m^2, assuming a spacing of d between N antenna elements and a spacing of $d/2$ at both ends. The effective aperture area is approximated according to $A_{\text{eff}} = A_{\text{physical}} \cos\theta$ in accordance with Equation (2.4). This results in a maximum antenna gain

$$G(\theta) \leq G_{\max}(\theta) = \frac{4\pi}{\lambda^2} A_{\text{eff}}(\theta) = \frac{4\pi}{\lambda^2}(Nd)^2 \cos\theta.$$

Note that the wavelength λ is given by $\lambda = c/f \approx 27.5$ cm, where c is the speed of light and $f = 1090$ MHz is the frequency of the wave. In order to relate the assumed maximum gain to the beam pattern, $B(\theta) = \boldsymbol{w}^{\text{H}}\boldsymbol{v}(\theta)$, the gain as a function of azimuth is approximated as

$$G(\theta) = \frac{|B(\theta)|^2}{\max\limits_{\theta}|B(\theta)|^2} G_{\max}(\theta). \tag{3.1}$$

From this, the maximum possible detection range can be calculated using Friis transmission equation (2.5), and setting the received power at the minimum detection level (MDL). This gives

$$R_{\max}(\theta) = \frac{\lambda}{4\pi}\sqrt{\frac{P_{\text{t}}' G_{\max}(\theta)}{\text{MDL}}} = \frac{\lambda}{4\pi} 10^{(P_{\text{t}}'^{[\text{dBW}]} + G_{\max}^{[\text{dBi}]}(\theta) - \text{MDL}^{[\text{dBW}]})/20}.$$

The minimum signal-to-interference threshold is set to $\text{SIR}_{\min} = 6$ dB. The minimum detection level set to $\text{MDL} = -115$ dBW, based on the ICAO requirement of minimum detection level for interrogator systems [4]. The minimum signal-to-noise is set to $\text{SNR}_{\min} = 10$ dB, which gives the total noise variance

$$P_{\text{n}} = 2\sigma_{\text{n}}^2 = \text{MDL}^{[\text{dBW}]} - \text{SNR}_{\min}^{[\text{dB}]} = -125\,\text{dBW}.$$

The parameters related to the antenna model described are summarized in Table 3.3.

Table 3.3: Values for the parameters used when modelling the simulated ULA antenna in the SSR system.

Parameter	Notation	Value
Number of antenna elements	N	6
Distance between elements	d	80 mm
Physical area	$\mathrm{A}_{\mathrm{physical}}$	0.23 m^2
Beam positions	θ_0	$\begin{bmatrix}0^\circ & \pm 15^\circ & \pm 30^\circ & \pm 45^\circ\end{bmatrix}$
Bandwidth	W	10 MHz
Simulated time	t_{sim}	1 s
Wavelength	λ	27.5 cm
Maximum gain in antenna normal	$G_{\max}(0^\circ)$	15.8 dBi
Maximum range in antenna normal	$R_{\max}(0^\circ)$	850 km
Signal-to-interference threshold	$\mathrm{SIR}_{\min}$	6 dB
Minimum detection level	MDL	-115 dBW
Signal-to-noise threshold	$\mathrm{SNR}_{\min}$	10 dB
Noise power	P_{n}	-125 dBW

3.3 Signal model

The ADS-B signal of interest is generated together with potential interfering signals. The preamble is simulated given the ICAO standard for Mode S. The data block that follows is then randomized with ones and zeros. Recall that the signal waveform $a(t)$ is given by Equation (2.1). A signal reaching the antenna is then modelled as

$$s(t) = \sqrt{P_{\mathrm{r}}} a(t) \exp(i2\pi f t),$$

where P_{r} is the received power calculated using Friis transmission equation (2.5) and f is the frequency of the signal. As per ICAO standards, $f = 1090 \pm 1$ MHz [4]. For simplicity, a downconversion to $f = 0 \pm 1$ MHz is assumed here.

Assuming D interfering signals, there are $D+1$ signals in total. The total incoming signal can then be written as the vector $\boldsymbol{s}(t) \in \mathbb{C}^{D+1}$. The received signal in each antenna element is then given by

$$\boldsymbol{x}(t) = \boldsymbol{A}\boldsymbol{s}(t) + \boldsymbol{n}(t),$$

where $\boldsymbol{x}(t) \in \mathbb{C}^N$ is the received signal [6]. $\boldsymbol{n}(t) \in \mathbb{C}^N$ is noise, which is assumed to be sampled from a complex normal distribution as $\boldsymbol{n} \sim \mathcal{CN}(\boldsymbol{0}, 2\sigma_{\mathrm{n}}^2 \boldsymbol{I}_N)$. $\boldsymbol{A} \in \mathbb{C}^{N \times (D+1)}$ is a matrix containing the steering vectors for the different signals according to

$$\boldsymbol{A} = \begin{bmatrix}\boldsymbol{v}(\theta_{\mathrm{SOI}}) & \boldsymbol{v}(\theta_1) & \boldsymbol{v}(\theta_2) & \dots & \boldsymbol{v}(\theta_D)\end{bmatrix}.$$

Note that the incoming signals are assumed to be in the far field relative to the receiving antenna. Hence, the plane wave approximation is assumed to hold. The

validity of this can be analyzed by looking at $d_{\mathrm{F}} > 2D_{\mathrm{F}}^2/\lambda$, where d_{F} is the Fraunhofer distance, describing the limit between near and far field [16]. D_{F} is the largest dimension of the receiving antenna, which in this case is Nd. Using the parameters defined above, this gives $d_{\mathrm{F}} \approx 1.7$ m. Since the signals are coming from targets located tens or hundreds of kilometers away, they are consequently in the far field relative to the receiving antenna.

Moreover, the signals are assumed to be narrowband signals. This assumption holds if $W\Delta T_{\max} \ll 1$, where W is the bandwidth of the system and $\Delta T_{\max}$ is the maximum travel time between two elements in the ULA [6]. $W = 10$ MHz and $\Delta T_{\max} = (N-1)d/c$ gives $W\Delta T_{\max} \approx 0.01$. Therefore, the narrowband assumption can be regarded as valid.

3.4 Analysis of adaptive beamforming

Implementing adaptive beamforming, the three different optimal beamformers described in Section 2.6.2 are analyzed: the MPDR, the LCMP and the PC. For the LCMP, a unit gain constraint for the SOI is imposed, with null constraints for the interfering signals.

To obtain the statistically optimal weights, the covariance matrix $\hat{\boldsymbol{R}}_x$ is estimated. The sample matrix inversion method described in Section 2.7.1 is applied here. Note that a sample frequency of 10 MHz is assumed, corresponding to the bandwidth of the system. This is in accordance with the Nyquist−Shannon sampling theorem, stating that $f_{\text{sampling}} > 2W$, where W is the bandwidth [5]. Since both a real and an imaginary data point are sampled in this case, the effective sampling rate is twice as high, thus satisfying the theorem.

Estimates for the directions of arrival, and consequently the steering vectors, for the different signals are obtained by implementing the ESPRIT algorithm described in Section 2.7.2. To obtain the dimension of the signal-plus-interference subspace, used for both the ESPRIT algorithm and in the implementation of the PC beamformer, the total number of signals, $D+1$, has to be estimated. This is done by requiring that the eigenvalues of $\hat{\boldsymbol{R}}_x$ should be 1 dB above the noise floor. Note that the MDL (10 dB over the noise floor) would be too strict a requirement here, as the SOI could still be amplified after obtaining the optimal weights. This method of determining the subspace dimension effectively leads to the assumption that the total number of signals is at most the number of elements, $D+1 \leq N$. The plausibility of this assumption is discussed further in Section 5.2.

3.5 Probability of detection

The probability of detecting an ADS-B signal of interest is modelled based on two main criteria. In order to successfully detect the signal, and therefore be able to decode the information it contains, the following should hold:

1. The signal power of the target of interest at the receiving antenna should be strong enough to reach SNR_{min} above the noise floor, i.e., reach the minimum detection level (MDL).
2. The signal power of the target at the receiving antenna should be SIR_{min} above the maximum of the sum of the signal power of the interfering signals.

By taking these two criteria into account, both the signal power of the SOI and its relation to the strength of the interfering signals are considered. From these two criteria, a detection binary random variable X_{d} can be defined as

$$X_{\text{d}} = \begin{cases} 1 & \text{if target deteced,} \\ 0 & \text{if target not detected.} \end{cases}$$

Mathematically, this assumption can, in linear units, be expressed as the joint probability

$$\mathbb{P}(X_{\text{d}} = 1) = \mathbb{P}\left(P_{\text{SOI}}(r_{\text{SOI}}, \theta_{\text{SOI}}) > \text{MDL}, \frac{P_{\text{SOI}}(r_{\text{SOI}}, \theta_{\text{SOI}})}{\max\limits_{t} \left[\sum_{k=1}^{D} P_k(r_k, \theta_k)\right](t)} > \text{SIR}_{\text{min}} \right).$$

Expressed more explicitly, in terms of the effective radiated power P'_{t} from the transmitting antennas in the transponders, the path loss $L_{\text{p}}(r)$ and the gain $G(\theta)$ of the receiving antenna, this can be written as

$$\mathbb{P}(X_{\text{d}} = 1) = \mathbb{P}\left(\frac{P'_{\text{t,SOI}} G(\theta_{\text{SOI}})}{L_{\text{p}}(r_{\text{SOI}})} > \text{MDL}, \frac{P'_{\text{t,SOI}} G(\theta_{\text{SOI}}) / L_{\text{p}}(r_{\text{SOI}})}{\max\limits_{t} \left[\sum_{k=1}^{D} P'_{\text{t},k} G(\theta_k) / L_{\text{p}}(r_k)\right](t)} > \text{SIR}_{\text{min}} \right).$$

From this, the probability of detection can be defined as $p_{\text{d}} = \mathbb{P}(X_{\text{d}} = 1)$. This probability is estimated for every point (x, y) in the spatial grid, using a sample mean $\hat{p}_{\text{d}}$ from Monte Carlo simulations. This is descried in more detail in Section 3.6 below.

3.6 Monte Carlo simulations

To estimate the probability of detection for every point in the grid, Monte Carlo simulations in MATLAB are performed. This method is preferred given the considerable complexity of the problem, with several random variables involved, making analytical solutions impractical to achieve. The random variables involved in the simulations are:

- The number of interfering signals: A Poisson distribution is assumed according to Equation (2.2). This gives $D_{\text{long}} \sim \text{Poi}(\lambda_{\text{Poi}}^{\text{long}})$ interfering Mode S Long signals and $D_{\text{short}} \sim \text{Poi}(\lambda_{\text{Poi}}^{\text{short}})$ interfering Mode S Short signals.
- Spatial position of interfering signals: Uniformly distributed points in a half-circle with radius R_{LOS}, centered at the SSR in the origin.
- Temporal position of interfering signals: Uniformly distributed in the interval $[120 - t_{\text{int}}, 240]$ µs, where t_{int} is the duration of the interfering signal. Note that this assumes that the SOI begins at $t = 120$ µs.

- Downconverted signal frequency: Normal distribution assumed according to $f \sim \mathcal{N}(0, \sigma_\mathrm{f}^2)$. Setting $\sigma_\mathrm{f} = 1/3$ MHz assures the requirement of 0 ± 1 MHz with 99.7 % certainty.
- Data block in the waveforms: Uniformly randomized order of ones and zeros.
- Noise: Complex normally distributed according to $\boldsymbol{n} \sim \mathcal{CN}(\boldsymbol{0}, 2\sigma_\mathrm{n}^2 \boldsymbol{I}_N)$.

For the two-channel Σ/Δ system, there is an additional random variable, namely the beam position which is active for the first ADS-B squitter. If there are N_beams beam positions and $N_\mathrm{squitters}$ squitters during the sweep time, the first squitter occurs somewhere during the first $\Delta t_\mathrm{squitter} = 1/f_\mathrm{squitter} = 0.5$ seconds, corresponding to one of the first $\lceil N_\mathrm{beams} \Delta t_\mathrm{squitter} / t_\mathrm{sim} \rceil = \lceil N_\mathrm{beams} / N_\mathrm{squitters} \rceil$ beam positions. The active beam position for the following squitter is then determined from this using the fixed squitter frequency of 2 Hz.

Pseudocode for the Monte Carlo simulations for the Σ/Δ system can be found in Algorithm 2 below.

Algorithm 2 Monte Carlo simulation, Σ/Δ system

```
for all iterations do
    for all positions in the grid do
        Assume a target is located at the given position.
        Calculate r_SOI and θ_SOI.
        Set X_d = 0 if r_SOI > R_max(θ_SOI).
        Draw beam position for first ADS-B squitter. Choose the beam positions
        for the next squitters accordingly.
        for all beam positions θ_0 with a squitter do
            Draw D_long ~ Poi(λ_Poi^long) interfering Mode S Long signals.
            Draw D_short ~ Poi(λ_Poi^short) interfering Mode S Short signals.
            Draw positions in space and time for the D = D_long + D_short interfering
            signals.
            Calculate G_Σ(θ) ∝ |v^H(θ_0)v(θ)|^2 and G_Δ(θ) ∝ |(−1)^{n≤N/2} v^H(θ_0)v(θ)|^2
            for SOI and interfering signals.
            Calculate received power P_SOI from SOI and P_k from interfering signals.
            Calculate SIR.
            if P_SOI > MDL and SIR > SIR_min for Σ or Δ channel then
                Target detected, X_d = 1.
                break
            end if
        end for
    end for
end for
```

Pseudocode for the Monte Carlo simulations for the multi-channel system with conventional beamforming can be found in Algorithm 3. Compared to Algorithm 2, there is no Δ channel here, as explained in Section 2.5. Since there are multiple independent beams active simultaneously, there is no random variable for which beam

position is active when the first squitter from the ADS-B target arrives. Thus, for every squitter, there is a chance to detect the signal in all beam positions.

Algorithm 3 Monte Carlo simulation, multi-channel system with conventional beamforming

for all iterations **do**
  for all positions in the grid **do**
    Assume a target is located at the given position.
    Calculate r_{SOI} and θ_{SOI}.
    Set $X_{\text{d}} = 0$ if $r_{\text{SOI}} > R_{\max}(\theta_{\text{SOI}})$.
    for all squitters **do**
      Draw $D_{\text{long}} \sim \text{Poi}(\lambda_{\text{Poi}}^{\text{long}})$ interfering Mode S Long signals.
      Draw $D_{\text{short}} \sim \text{Poi}(\lambda_{\text{Poi}}^{\text{short}})$ interfering Mode S Short signals.
      Draw positions in space and time for the $D = D_{\text{long}} + D_{\text{short}}$ interfering signals.
      for all beam positions θ_0 **do**
        Calculate $G(\theta) \propto |\boldsymbol{v}^{\text{H}}(\theta_0)\boldsymbol{v}(\theta)|^2$ for SOI and interfering signals.
        Calculate received power P_{SOI} from SOI and P_k from interfering signals.
        Calculate SIR.
        if $P_{\text{SOI}} >$ MDL **and** SIR $>$ SIR$_{\min}$ **then**
          Target detected, $X_{\text{d}} = 1$.
          break
        end if
      end for
    end for
  end for
end for

Pseudocode for the Monte Carlo simulations for the multi-channel system with adaptive beamforming can be seen in Algorithm 4. The noticeable difference compared to Algorithms 2 and 3 is that there are no predetermined beam positions θ_0. Instead, the optimal weight vector, $\boldsymbol{w}$, is determined using the input signal $\boldsymbol{x}(t)$. Even though the digital multi-channel system allows for several simultaneous beam positions, only one is used here, as the obtained $\boldsymbol{w}$ should be the statistically optimal one.

Note that a DOA estimation $\hat{\theta}$ is obtained for all distinguishable signals, each yielding a separate $\boldsymbol{w}$. Instead of looping through all $\boldsymbol{w}$, the one resulting in the smallest absolute error relative to the true value is chosen. That is, $\hat{\theta}_{\text{SOI}} = \min |\hat{\theta}_i - \theta_{\text{SOI}}|$, where i counts the number of estimated signals.

Algorithm 4 Monte Carlo simulation, multi-channel system with adaptive beamforming

for all iterations **do**
  for all positions in the grid **do**
    Assume a target is located at the given position.
    Calculate r_{SOI} and θ_{SOI}.
    Set $X_{\text{d}} = 0$ if $r_{\text{SOI}} > R_{\max}(\theta_{\text{SOI}})$.
    for all squitters **do**
      Draw $D_{\text{long}} \sim \text{Poi}(\lambda_{\text{Poi}}^{\text{long}})$ interfering Mode S Long signals.
      Draw $D_{\text{short}} \sim \text{Poi}(\lambda_{\text{Poi}}^{\text{short}})$ interfering Mode S Short signals.
      Draw positions in space and time for the $D = D_{\text{long}} + D_{\text{short}}$ interfering signals.
      Simulate the input signal $\boldsymbol{x}(t)$.
      Estimate the sample covariance matrix $\hat{\boldsymbol{R}}_x$ and directions of arrival.
      Determine the optimal weight vector $\boldsymbol{w}$.
      Calculate $G(\theta) \propto |\boldsymbol{w}^{\text{H}}\boldsymbol{v}(\theta)|^2$ for SOI and interfering signals.
      Calculate received power P_{SOI} from SOI and P_k from interfering signals.
      Calculate SIR.
      if $P_{\text{SOI}} >$ MDL **and** SIR $>$ SIR$_{\min}$ **then**
        Target detected, $X_{\text{d}} = 1$.
        break
      end if
    end for
  end for
end for

When performing Monte Carlo simulations, it is of great importance to determine the number of iterations sufficient to obtain good statistics. The simulation has to be run long enough such that a large part of the probability space can be explored. On the other hand, the computational time must also be considered. To estimate the proper number of iterations, tests are performed for five randomly selected points in the grid, which can be found in Table 3.4.

If $X_{\text{d},1}, X_{\text{d},2}, \ldots, X_{\text{d},n}$, obtained from each run in the Monte Carlo simulation, are assumed to be independent and identically distributed random variables, the law of large numbers gives the sample average

$$\hat{p}_{\text{d}} = \overline{X}_{\text{d}} = \frac{1}{n}(X_{\text{d},1} + X_{\text{d},2} + \cdots + X_{\text{d},n}).$$

As $n \to \infty$, the sample average converges to the actual expected value of X_{d}, according to $\overline{X}_{\text{d}} \to \mathbb{E}(X_{\text{d},1}) = \mathbb{E}(X_{\text{d},2}) = \cdots = p_{\text{d}}$ [13]. Therefore, the sample average can be used as an estimator for p_{d}. Analyzing the variance, it is given by

$$\text{Var}(\overline{X}_{\text{d}}) = \text{Var}(\hat{p}_{\text{d}}) = \frac{\sigma_{\text{d}}^2}{n},$$

where $\mathrm{Var}(X_{\mathrm{d},i}) = \sigma_{\mathrm{d}}^2$. It can be noted that $\mathrm{Var}(\hat{p}_{\mathrm{d}}) \to 0$ as $n \to \infty$. As the number of Monte Carlo samples increases, the estimation for p_{d} becomes less uncertain.

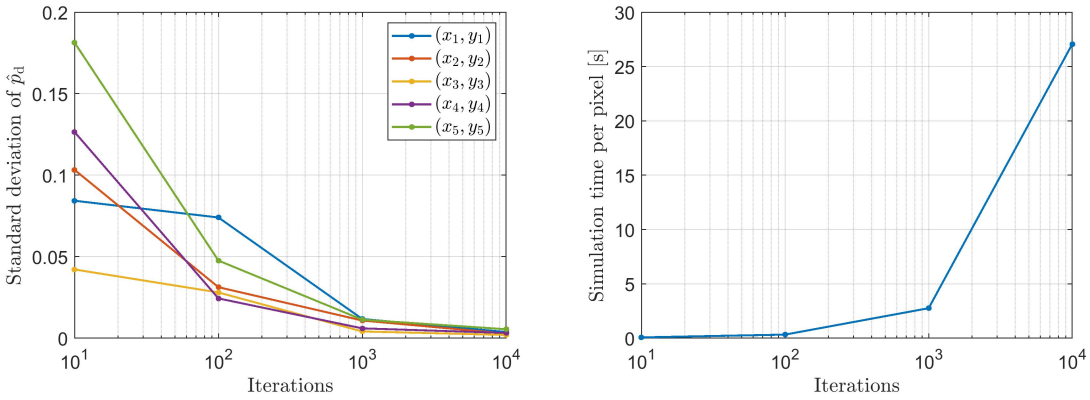

(a) **(b)**

Figure 3.3: **(a)** The standard deviation of $\hat{p}_{\mathrm{det}}$ as a function of the number of Monte Carlo iterations for five randomly selected points. Note that $\hat{p}_{\mathrm{d}}$ corresponds to the sample mean $\overline{X}_{\mathrm{d}}$ of the number of Monte Carlo iterations. **(b)** The simulation time per pixel as a function of the number of iterations.

Figure 3.3(a) displays the standard deviation of $\hat{p}_{\mathrm{d}}$, $\sqrt{\mathrm{Var}(\hat{p}_{\mathrm{d}})}$, as a function of the number of Monte Carlo iterations for the five randomly selected points. Note that the standard deviation is approximated based on ten separate runs for each point. Figure 3.3(b) displays the average simulation time per pixel as a function of the number of iterations.

Table 3.4: Coordinates and standard deviations of $\hat{p}_{\mathrm{det}}$ for the five randomly selected points. The results are displayed for 10, 100, 1,000 and 10,000 iterations.

		Standard deviation of $\hat{p}_{\mathrm{d}}$			
Point	Coordinate [km]	10^1	10^2	10^3	10^4
1	$(170, 40)$	8.4×10^{-2}	7.4×10^{-2}	1.2×10^{-2}	3.8×10^{-3}
2	$(330, 660)$	1.0×10^{-1}	3.1×10^{-2}	1.1×10^{-2}	2.8×10^{-3}
3	$(10, 180)$	4.2×10^{-2}	2.8×10^{-2}	4.1×10^{-3}	2.0×10^{-3}
4	$(-10, 240)$	1.3×10^{-1}	2.4×10^{-2}	6.0×10^{-3}	3.2×10^{-3}
5	$(-40, 500)$	1.8×10^{-1}	4.8×10^{-2}	1.1×10^{-2}	5.5×10^{-3}

Table 3.4 displays the coordinates for the different points, together with the approximated standard deviations for the different number of Monte Carlo iterations.

From Figure 3.3 and Table 3.4, it can be noted that the standard deviation is in the order of around 10^{-2} for $n = 10^3$ iterations. For $n = 10^4$ iterations, the standard deviation is reduced with around 60 %, while the simulation time increases with nearly 900 %.

The standard deviation can be used to estimate a confidence interval [13]. Assuming a standard deviation of the sample mean $\hat{p}_\mathrm{d}$ of 0.01, a 95 % confidence interval is given by

$$\left[\hat{p}_\mathrm{d} - 1.96\frac{\sigma_\mathrm{d}}{\sqrt{n}}, \hat{p}_\mathrm{d} + 1.96\frac{\sigma_\mathrm{d}}{\sqrt{n}}\right] \approx \hat{p}_\mathrm{d} \pm 0.02.$$

For this study, this is regarded as a sufficient level of accuracy for estimating the probability in each point of the grid. With regards to this, as well as the simulation time, 1,000 Monte Carlo iterations are deemed sufficient.

4

Results and analysis

In this chapter, the results obtained from implementing the methods described in the previous chapter are presented.

4.1 Probability of detection

Figures 4.1, 4.2, 4.3, 4.4 and 4.5 display the estimated probability of detection $\hat{p}_{\mathrm{d}}$ for each pixel in the grid for the different algorithms implemented: analog conventional Σ/Δ, digital conventional multi-channel (CMC), adaptive minimum power distortionless response (MPDR) multi-channel, adaptive linear constraint minimum power (LCMP) multi-channel and adaptive principal component (PC) multi-channel. A summary of these algorithms can be seen in Table 4.1 below.

Table 4.1: The different algorithms analyzed. The second column describes the number of digitized channels. In the case of Σ/Δ, the output Σ and Δ channel are the two digital channels. In the other cases, all six antenna elements are digitized separately. The third column describes whether analog or digital phase shifters are used, resulting in different types of beamforming.

Algorithm	Digitized channels	Phase shifters	Beamforming type
Σ/Δ	2	Analog	Conventional
CMC	6	Digital	Conventional
MPDR	6	Digital	Adaptive
LCMP	6	Digital	Adaptive
PC	6	Digital	Adaptive

The configuration of analog and digital systems is described in Section 2.5. Conventional and adaptive beamforming are described in Section 2.6.

The results are presented for three different values for the disturbance parameter γ: 5×10^{-3}, 1×10^{-2} and 2×10^{-2} s^{-1} km^{-2}. As seen in Table 3.1, this corresponds to expected values of approximately 1.1, 2.1 and 4.2 number of interfering signals, respectively.

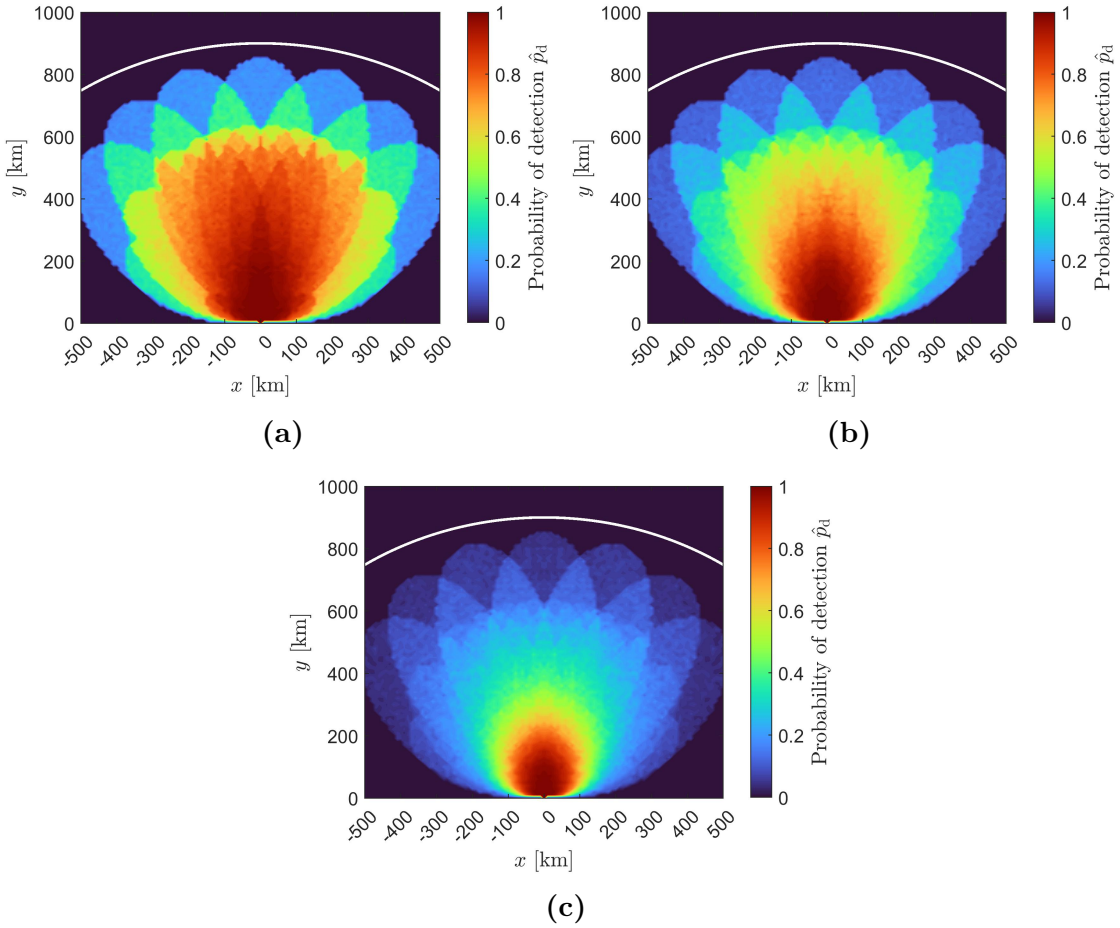

Figure 4.1: Estimated probability of detection for the Σ/Δ system with analog conventional beamforming. **(a)** The case $\gamma = 5 \times 10^{-3}$ s^{-1} km^{-2}. **(b)** The case $\gamma = 1 \times 10^{-2}$ s^{-1} km^{-2}. **(c)** The case $\gamma = 2 \times 10^{-2}$ s^{-1} km^{-2}. Red tones indicate higher probability, while blue tones indicate a lower probability. Note that the maximum line-of-sight distance at 900 km is marked by a white line.

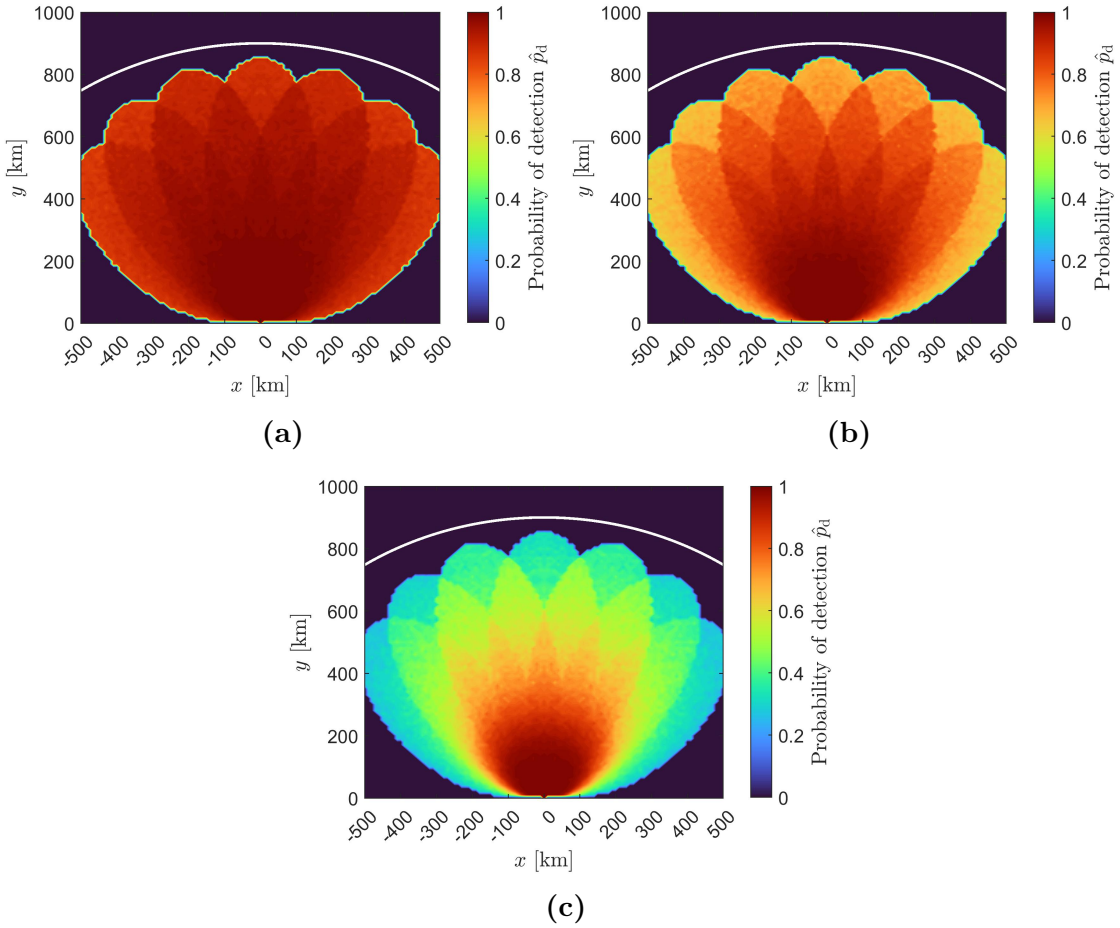

Figure 4.2: Estimated probability of detection for the multi-channel system with digital conventional beamforming (CMC). **(a)** The case $\gamma = 5 \times 10^{-3}$ s^{-1} km^{-2}. **(b)** The case $\gamma = 1 \times 10^{-2}$ s^{-1} km^{-2}. **(c)** The case $\gamma = 2 \times 10^{-2}$ s^{-1} km^{-2}. Red tones indicate higher probability, while blue tones indicate a lower probability. Note that the maximum line-of-sight distance at 900 km is marked by a white line.

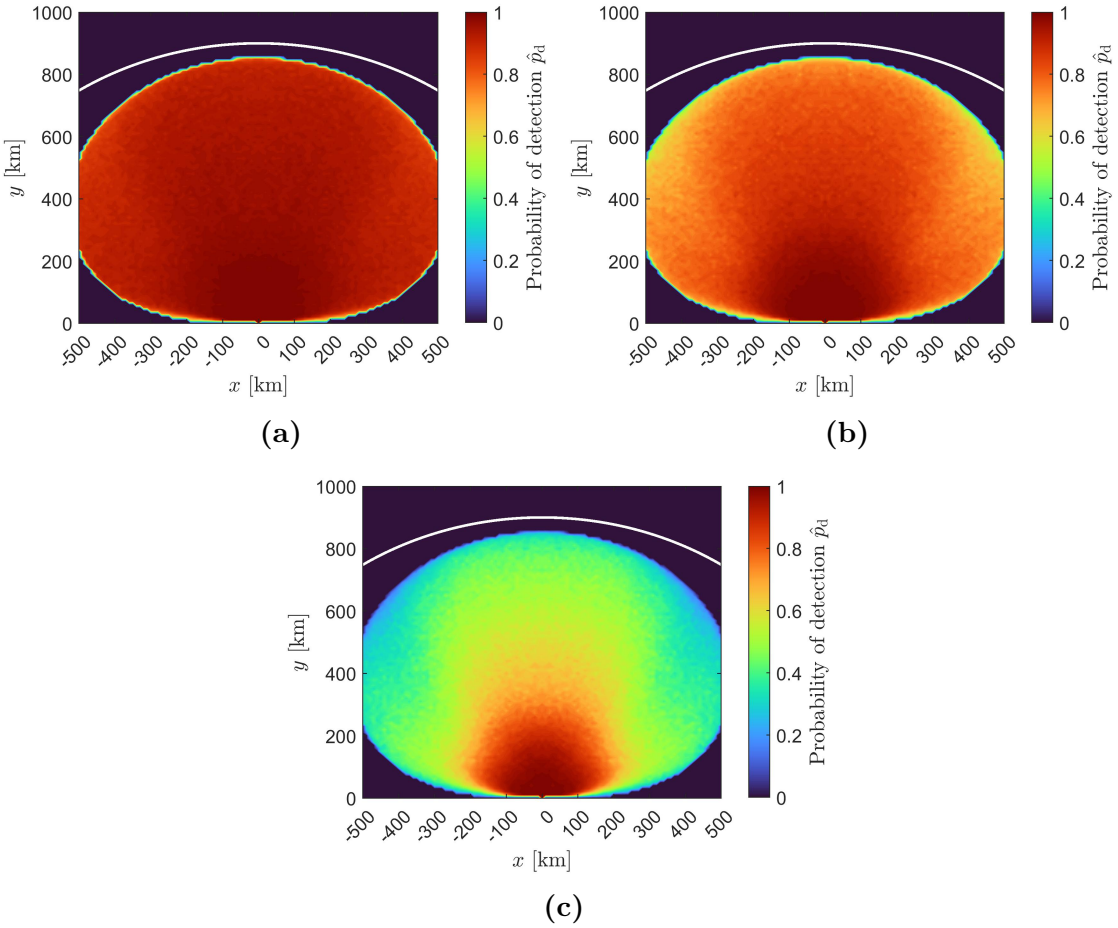

Figure 4.3: Estimated probability of detection for the multi-channel system with adaptive MPDR beamforming. **(a)** The case $\gamma = 5 \times 10^{-3}$ s^{-1} km^{-2}. **(b)** The case $\gamma = 1 \times 10^{-2}$ s^{-1} km^{-2}. **(c)** The case $\gamma = 2 \times 10^{-2}$ s^{-1} km^{-2}. Red tones indicate higher probability, while blue tones indicate a lower probability. Note that the maximum line-of-sight distance at 900 km is marked by a white line.

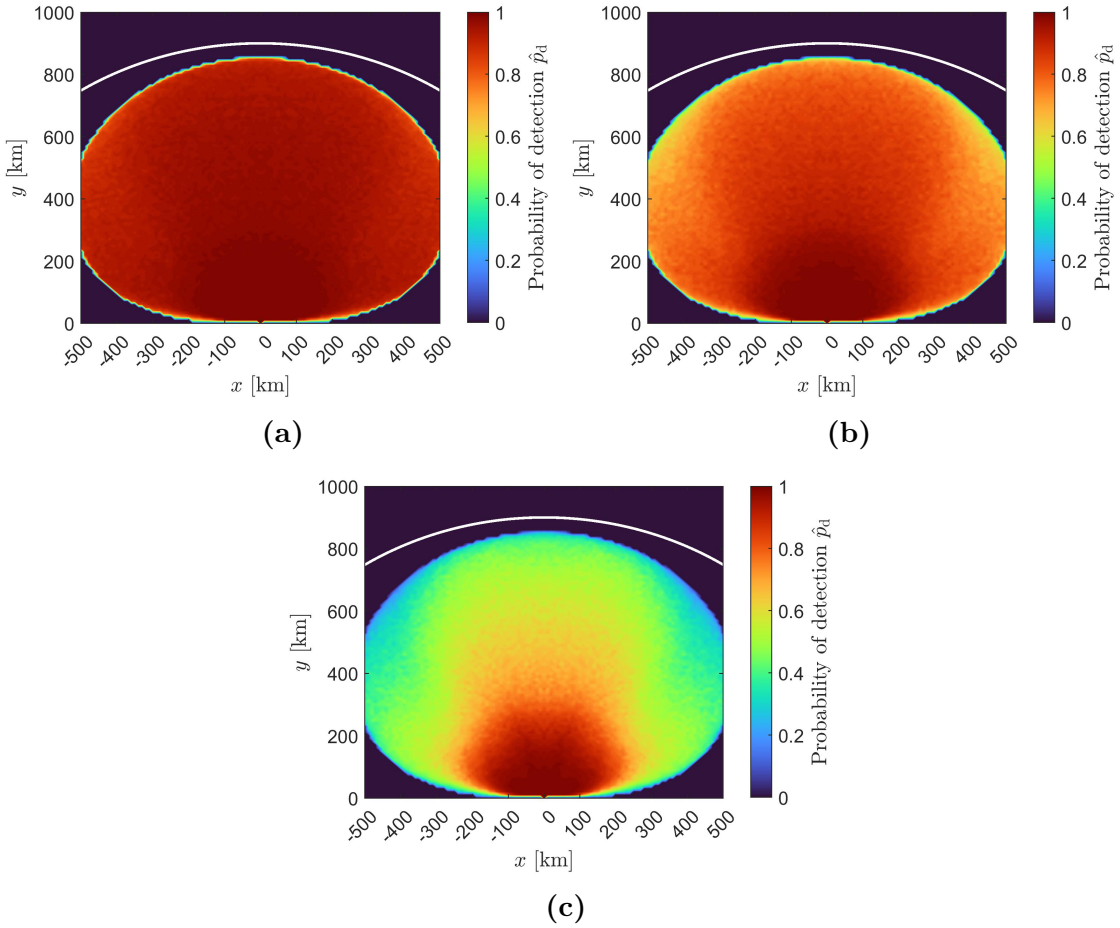

Figure 4.4: Estimated probability of detection for the multi-channel system with adaptive LCMP beamforming. **(a)** The case $\gamma = 5 \times 10^{-3}$ s^{-1} km^{-2}. **(b)** The case $\gamma = 1 \times 10^{-2}$ s^{-1} km^{-2}. **(c)** The case $\gamma = 2 \times 10^{-2}$ s^{-1} km^{-2}. Red tones indicate higher probability, while blue tones indicate a lower probability. Note that the maximum line-of-sight distance at 900 km is marked by a white line.

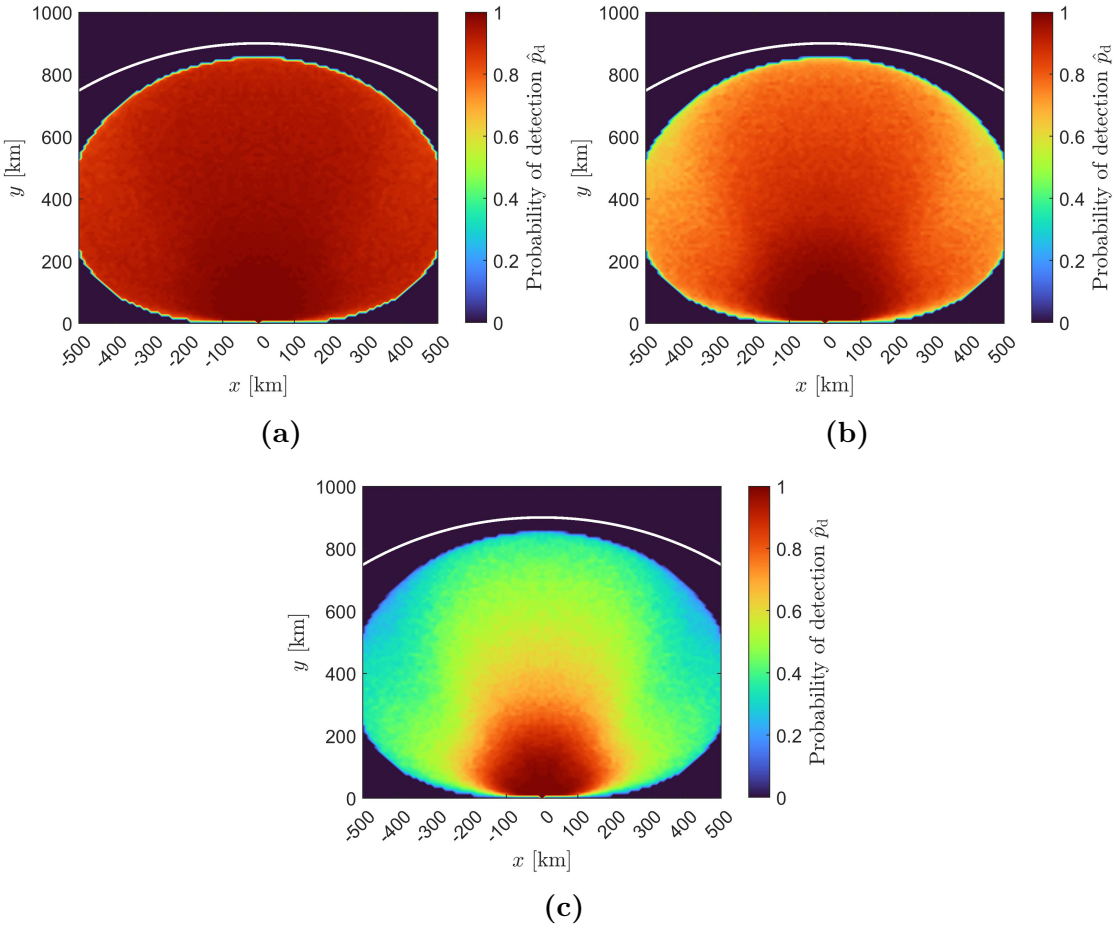

Figure 4.5: Estimated probability of detection for the multi-channel system with adaptive PC beamforming. **(a)** The case $\gamma = 5 \times 10^{-3}$ s^{-1} km^{-2}. **(b)** The case $\gamma = 1 \times 10^{-2}$ s^{-1} km^{-2}. **(c)** The case $\gamma = 2 \times 10^{-2}$ s^{-1} km^{-2}. Red tones indicate higher probability, while blue tones indicate a lower probability. Note that the maximum line-of-sight distance at 900 km is marked by a white line.

To numerically analyze how the probability of detection depends on the γ parameter, as well as the distance to the SSR in the origin, the probability can be calculated in different subareas. Three subareas are defined by the distance from the SSR to the target: 0−300 km, 300−600 km and 600−900 km. The three regions are displayed in Figure 4.6.

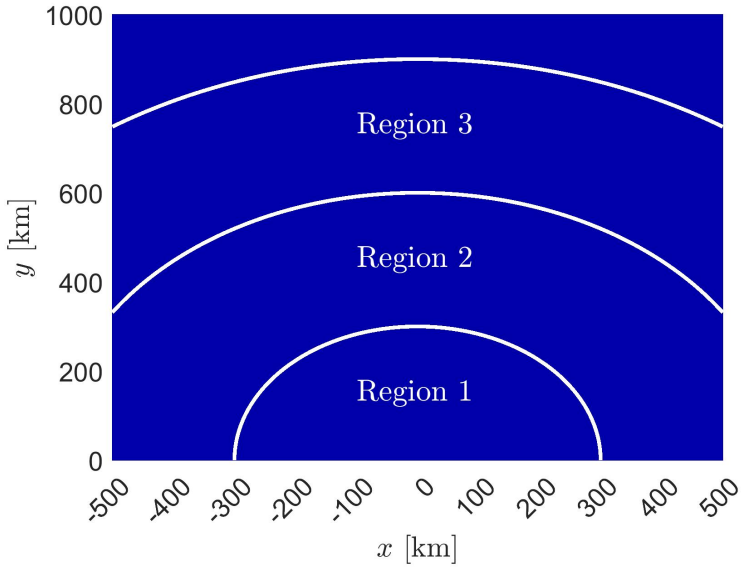

Figure 4.6: The three different subareas defined by the distance between the target and the SSR. Region 1: 0−300 km. Region 2: 300−600 km. Region 3: 600−900 km.

As mentioned in Section 3.5, the probability of detection in a point (x, y) is given by

$$p_{\mathrm{d}} = \mathbb{P}(X_{\mathrm{d}} = 1|(x, y)),$$

where

$$X_{\mathrm{d}} = \begin{cases} 1 & \text{if target deteced,} \\ 0 & \text{if target not detected.} \end{cases}$$

Denote the probability of detection, given a target located in Region k, as $p_{\mathrm{d}}(k) = \mathbb{P}(X_{\mathrm{d}} = 1|k)$. From the law of total probability, this can be calculated according to

$$p_{\mathrm{d}}(k) = \mathbb{P}(X_{\mathrm{d}} = 1|k) = \sum_{(x_i,y_i)} \mathbb{P}(X_{\mathrm{d}} = 1|k, (x_i, y_i))\mathbb{P}((x_i, y_i)|k) =$$

$$= \sum_{\substack{(x_i,y_i) \in \\ \text{Region } k}} \mathbb{P}(X_{\mathrm{d}} = 1|(x_i, y_i))\mathbb{P}((x_i, y_i)|k).$$

Note that for a uniform distribution of targets, $\mathbb{P}((x_i, y_i)|k) = 1/(\text{Number of pixels in Region } k)$. Hence, the total probability of detection given a target in a specific region can be seen as an average probability [13].

Figure 4.7 displays the average probability of detection as a function of the γ parameter for the different systems in the three different subareas. The probability

values are also displayed in Table 4.2. As explained in Section 3.6, the estimated probability in each pixel has an inherent uncertainty given by the number of iterations used for the Monte Carlo simulations. For example, a 95 % confidence interval gives an error margin of approximately ±0.02.

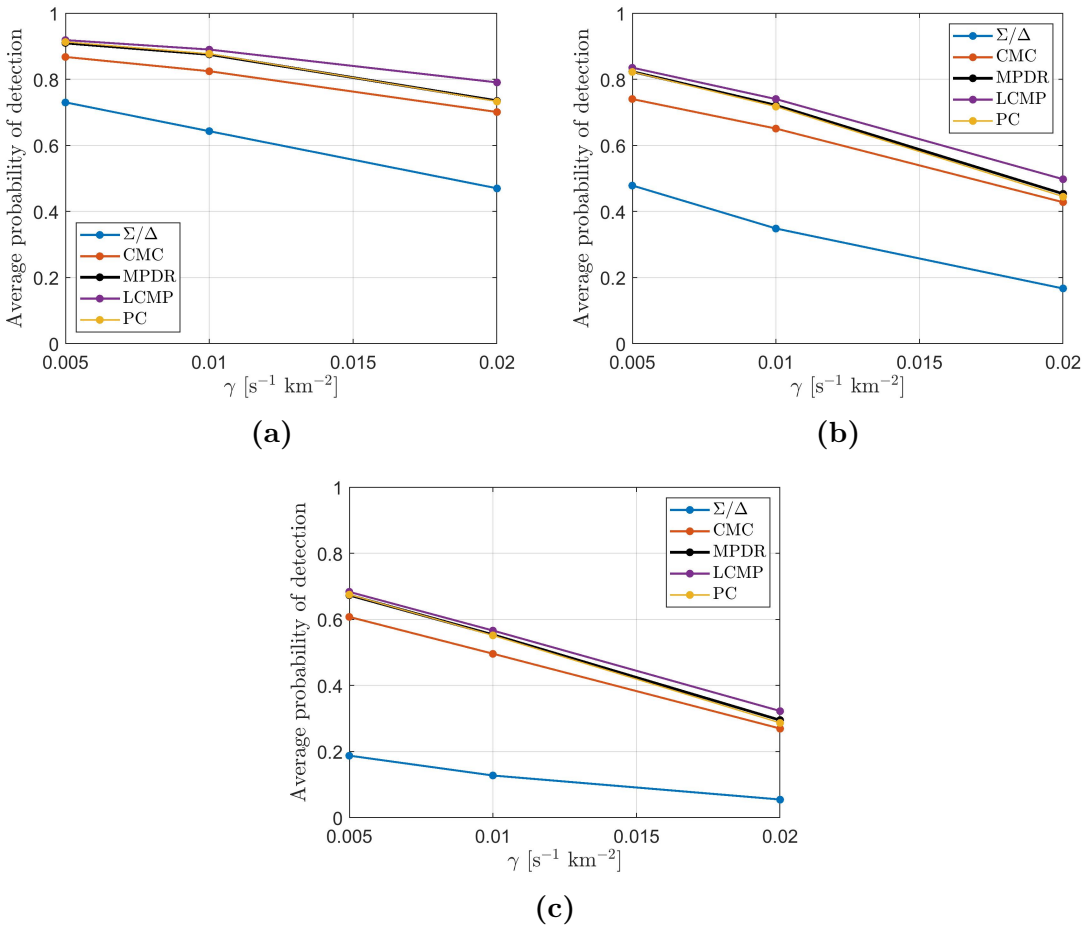

Figure 4.7: Average probability of detection as a function of the message rate per area γ [s^{-1} km^{-2}] for the different systems in different subareas. **(a)** Targets at a distance of 0−300 km. **(b)** 300−600 km. **(c)** 600−900 km.

Table 4.2: The average probability of detection shown in Figure 4.7 displayed in table form.

Algorithm	Distance [km] / γ [s^{-1} km^{-2}]	0−300	300−600	600−900
Σ/Δ	5×10^{-3}	0.73	0.48	0.19
	1×10^{-2}	0.64	0.35	0.13
	2×10^{-2}	0.47	0.17	0.05
CMC	5×10^{-3}	0.87	0.74	0.61
	1×10^{-2}	0.82	0.65	0.50
	2×10^{-2}	0.70	0.43	0.27
MPDR	5×10^{-3}	0.91	0.82	0.67
	1×10^{-2}	0.88	0.72	0.55
	2×10^{-2}	0.74	0.45	0.29
LCMP	5×10^{-3}	0.92	0.84	0.68
	1×10^{-2}	0.89	0.74	0.57
	2×10^{-2}	0.79	0.50	0.32
PC	5×10^{-3}	0.91	0.82	0.68
	1×10^{-2}	0.88	0.72	0.55
	2×10^{-2}	0.73	0.45	0.29

Analyzing Figures 4.1, 4.2, 4.3, 4.4 and 4.5, as well the average probability shown in Figure 4.7 and Table 4.2, several observations can be made. It can be noted that the Σ/Δ system exhibits the lowest probability of detection. The CMC has 1.2−1.5 times higher average probability in Region 1 and 3.2−4.9 higher in Region 3. It can also be noted that the relative performance difference between the cases increases with higher γ. This indicates that the performance of the CMC, compared to the Σ/Δ, improves progressively as both the distance to the targets and the amount of disturbance in the air increases.

Comparing these results to the adaptive algorithms, the MPDR has in general around 5−12 % higher probability compared to the CMC. The difference between the two is more noticeable in Region 3, indicating that the MPDR is more successful in suppressing interfering signals further out compared to the CMC. It can be noted that the PC algorithm displays nearly identical results compared to the MPDR. This could indicate that the dimensionality reduction performed, described in Section 2.6.2.3, in this case works satisfactory.

The LCMP displays the best performance. Compared to the CMC, the probability of detection is between around 6−13 % higher in Region 1 and 12−20 % in Region 3. The most noticeable difference is for targets in Region 3 with high disturbance, which could indicate that the LCMP, as a result of the imposed null constraints, handles the interfering signals more efficient than the CMC. The larger difference in Region 3 is also reasonable given that the conventional beamforming is performed for a finite set of seven beam positions. This lowers the gain, and hence the detection range, in the gap between the beams, creating the leaf-like shapes in Figures 4.1 and 4.2.

4.2 Beamforming examples

In order to understand the results presented in Section 4.1 on a deeper level, some illustrative test cases are presented here.

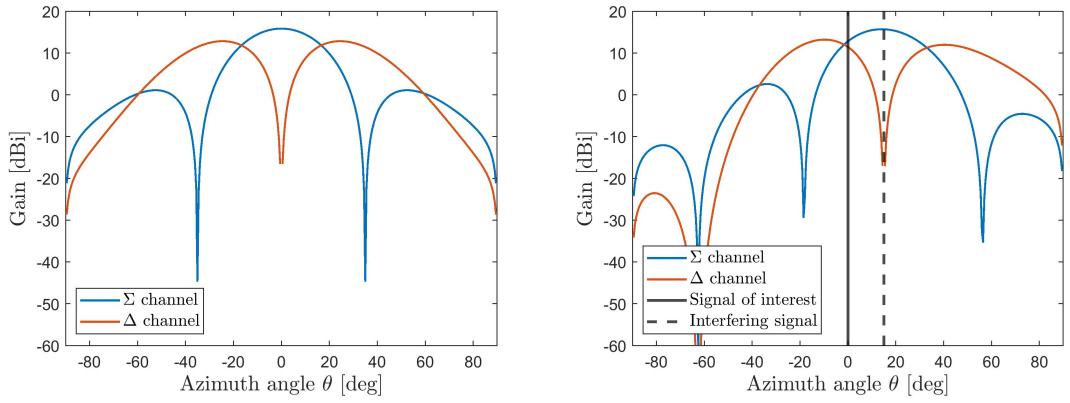

(a) **(b)**

Figure 4.8: Antenna pattern for the Σ/Δ system, where the beam position θ_0 steps from $-45°$ to $45°$. **(a)** $\theta_0 = 0°$, with no signal of interest present. **(b)** $\theta_0 = 15°$, where a signal of interest (solid line) is present at $0°$ together with one interfering signal (dashed line) at $15°$.

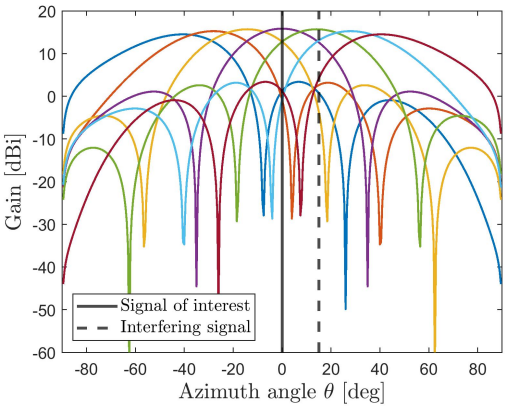

Figure 4.9: Antenna pattern for a multi-channel system with reception in simultaneous active beam positions $\theta_0 = 0°, \pm 15°, \pm 30°, \pm 45°$. Each beam is indicated by a unique color. A signal of interest is present at $0°$, together with one interfering signals at $15°$.

Figure 4.8 displays antenna patterns, showing the gain as a function of azimuth angle, for the Σ/Δ system. The Σ channel is shown in blue, while the Δ channel is shown in red. Figures 4.8(a) and 4.8(b) illustrate the inherent problem with the analog beamforming applied here. Assuming a signal of interest is present at $0°$, there is always a possibility that this does not match the active beam position θ_0. In this case, the probability of obtaining an incoming SOI, corresponding

to an ADS-B squitter, in a given beam position is given by $N_{\text{squitters}}/N_{\text{beams}} = (t_{\text{sim}} f_{\text{squitter}})/N_{\text{beams}} \approx 0.29$. Recall that $t_{\text{sim}} = 1$ s, $f_{\text{squitter}} = 2$ Hz and $N_{\text{beams}} = 7$ is used in the simulations. As shown in Figure 4.8(b), this could result in an interfering signal (here located at $+15°$) receiving higher gain than the signal of interest. This lowers the signal-to-interferece ratio, making it more difficult to detect the target.

For example, detection in the Σ channel in beam position $0°$ would give a gain of 15.8 dBi for the SOI, with the interfering signal at 12.6 dBi. Detection at $\theta_0 = 15°$ instead gives 12.8 dBi for the SOI, with 15.7 dBi for the interfering signal. In this particular case, it would be advantageous to detect the signal in the Δ channel, but this still results in a lower gain in the direction of the SOI compared to the case in Figure 4.8(a).

Figure 4.9 displays antenna patterns for the CMC. In this case, all beam positions ($\theta_0 = 0°, \pm 15°, \pm 30°, \pm 45°$) are active simultaneously. Consequently, each beam position is active during the time t_{sim}, rather than during $t_{\text{sim}}/N_{\text{beams}}$. Having several beam positions active at once reduces the risk of having a disadvantageous beam position active when the signal arrives, hence illustrating the profit of applying digital beamforming.

4.2.1 Comparison to adaptive beamforming

The systems using conventional beamforming, independently if analog or digital, does not adapt to the properties of the incoming signal. To compare the conventional beamforming results to adaptive beamforming, five different test cases are used. Cases 1a and 1b have one interfering signal, Cases 2a and 2b have two and Case 3 has four. Note that these cases represent the three different values of the γ parameter. For example, $\gamma = 1 \times 10^{-2}$ s^{-1} km^{-2} gives an average of $\lambda_{\text{Poi}}^{\text{long}} = 1.2$ Mode S Long replies and $\lambda_{\text{Poi}}^{\text{short}} = 0.92$ Mode S Short replies. For the different values of γ and λ_{Poi}, see Table 3.1.

For all cases, the target of interest is located at a distance of $r = 500$ km with angle $\theta = 0°$. The interfering targets are located at a distance of $r = 706$ km, thus comparing signals of equal strength at the receiving antenna. In Cases 1a and 1b, the single interfering signal is assumed to be of type Mode S Long and start 80 µs after the SOI. In Cases 2a and 2b, a Mode S Short signal is added 24 µs before the SOI. This implies that two thirds of the SOI is covered, see Figure 4.10. In Case 3, two additional signals are added with the same relative time difference as the first two. Directions of arrival for the interfering signals in the different cases are presented in Table 4.3.

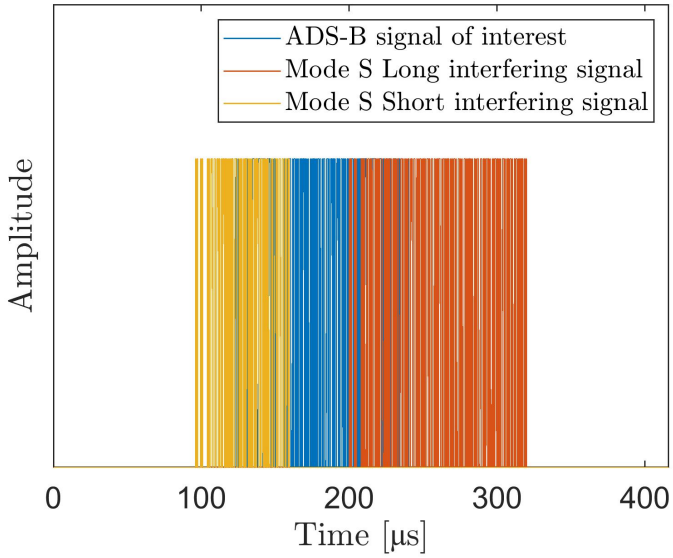

Figure 4.10: An ADS-B signal of interest interfered by a Mode S Long interfering signal, starting 80 µs after the SOI, and a Mode S Short interfering signal, starting 24 µs before the SOI. This corresponds to Cases 2a and 2b in Table 4.3.

Table 4.3: Directions of arrival for the interfering signals in the five different test cases used for comparing the adaptive algorithms. The subscript "L" denotes a Mode S Long signal, while "S" denotes a Mode S Short signal.

Case	θ_1	θ_2	θ_3	θ_4
1a	$+45°$ L			
1b	$+15°$ L			
2a	$+45°$ L	$-45°$ S		
2b	$+15°$ L	$-15°$ S		
3	$+45°$ L	$-45°$ L	$+15°$ S	$-15°$ S

Figures 4.11, 4.12 and 4.13 display antenna patterns for the different algorithms for the different test cases presented in Table 4.3. As before, the SOI is marked by a black solid line and the interfering signals are marked by black dashed lines. The gain values in dBi for both signal of interest and interfering signals, together with the obtained signal-to-interference ratio, are displayed in Table 4.4.

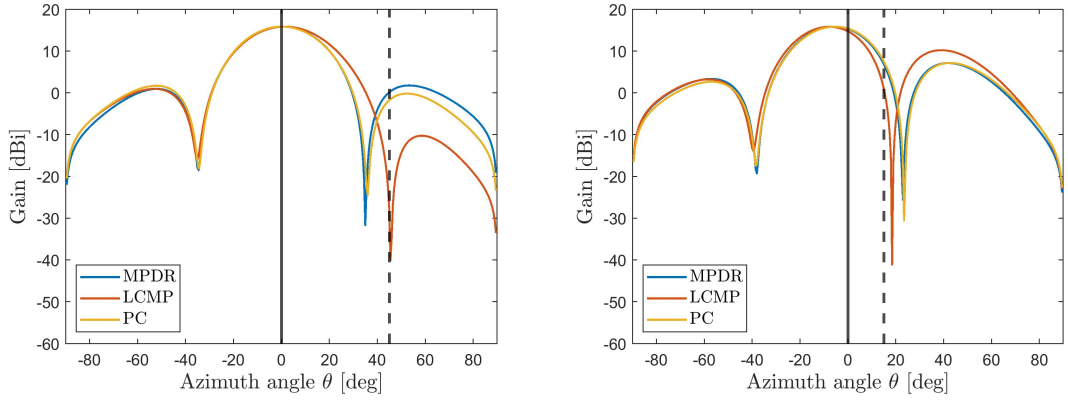

(a) **(b)**

Figure 4.11: Antenna patterns for Case 1a in **(a)**, with one interfering signal at +45°, and for Case 1b in **(b)**, with one interfering signal at +15°.

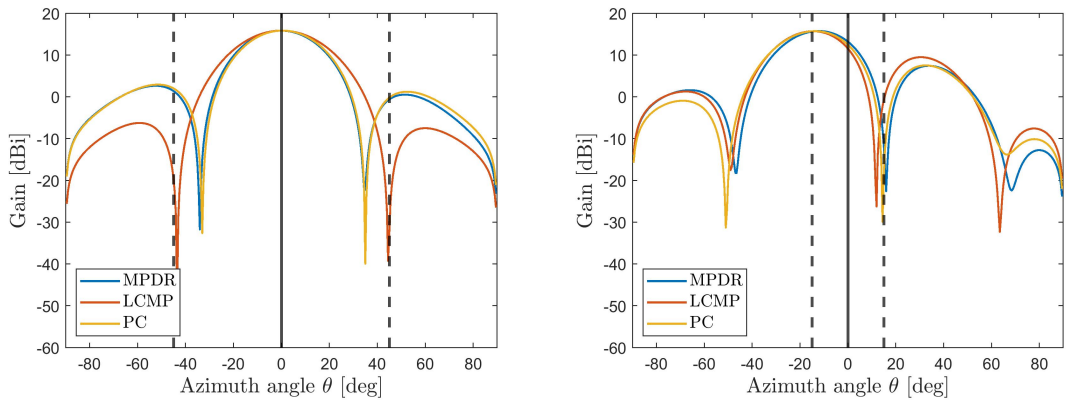

(a) **(b)**

Figure 4.12: Antenna patterns for Case 2a in **(a)**, with two interfering signals at ±45°, and for Case 2b in **(b)**, with two interfering signals at ±15°.

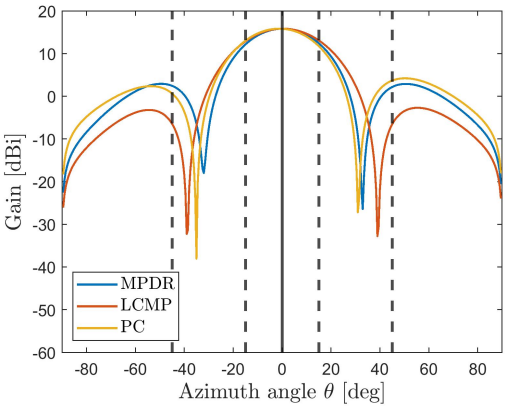

Figure 4.13: Antenna pattern for Case 3, with four interfering signals at ±45° and ±15°.

Table 4.4: The gain evaluated in the directions of the SOI and the interfering signals for the different cases and algorithms. The gain values are displayed in the unit dBi. Note that the numbers presented here correspond to the antenna patterns presented in Figures 4.11, 4.12 and 4.13. The case with conventional beamforming in a Σ channel at beam position $\theta_0 = 0°$ is included as a comparison.

Algorithm	Case	$G(\theta_{\text{SOI}})$	$G(\theta_1)$	$G(\theta_2)$	$G(\theta_3)$	$G(\theta_4)$	SIR [dB]
MPDR	1a	15.8	0.1				15.7
	1b	15.3	6.9				8.4
	2a	15.8	−0.6	1.4			14.5
	2b	13.2	−11.3	15.6			−2.4
	3	15.8	3.2	3.0	12.1	12.2	0.6
LCMP	1a	15.8	−28.0				43.8
	1b	14.7	1.0				13.7
	2a	15.8	−33.1	−19.4			35.3
	2b	11.6	−0.9	15.7			−4.1
	3	15.8	−5.9	−3.7	13.0	12.7	−0.1
PC	1a	15.8	−1.8				17.6
	1b	15.4	7.5				7.8
	2a	15.8	−0.2	2.0			13.8
	2b	12.6	−22.3	15.7			−3.2
	3	15.8	3.3	2.1	12.1	12.6	0.4
$\Sigma(0°)$	1a	15.8	−0.3				16.1
	1b	15.8	12.6				3.2
	2a	15.8	−0.3	−0.3			16.1
	2b	15.8	12.6	12.6			3.2
	3	15.8	−0.3	−0.3	12.6	12.6	0.2

It can be noted that the LCMP gives a large signal-to-interference ratio for Cases 1a and 2a, where the interfering signals is further away in terms of azimuth angle. This indicates that the null constraint imposed in the optimization, together with the direction estimation with the ESPRIT algorithm, works well. As observed before, the MPDR and PC exhibit similar performance. Compared to the LCMP, the MPDR does not display the same distinct decrease in gain in the direction of the interfering signals. However, it still exhibits a gain decrease in the vicinity of the interfering signals. This is due to the fundamental functionality of the MPDR, where nulls are implicitly placed in the direction of interfering signals, rather than imposing explicit constraints.

For Case 1b, it can be noted that the LCMP does not display the same accuracy. This could indicate that the ESPRIT algorithm is not as accurate in the case when the interfering signal is closer to the SOI. This is even more noticeable for Cases 2b and 3. In Case 2b, the SOI cannot be distinguished from the interfering signals. This results in a maximum gain at $-15°$ instead of $0°$. In Case 3, the interfering signals at $\pm 15°$ cannot be distinguished from the SOI for any of the algorithms.

Note that the SIR values presented here is calculated without considering the noise

floor level. For example, an SIR value at 43.8 dB, as for LCMP in Case 1a, is not necessary here. A maximum "efficient SIR" is instead given by an SOI with maximum possible gain and an interfering signal suppressed to the noise floor, resulting in approximately 14.6 dB.

4.2.2 Beamforming in the time domain

The beamforming process can also be studied in the time domain. A test case with a target at $r = 100$ km and $\theta = 0°$ is presented here, with one Mode S Long interfering signal at $r = 141$ km and $\theta = 15°$. The interfering signal starts 60 µs after the SOI, making it half-covered. Figure 4.14 displays the incoming signal $\boldsymbol{x}(t)$ before any processing.

Figures 4.15 and 4.16 display the signal obtained from applying the MPDR and LCMP beamforming algorithm, respectively. Figure 4.17 displays the signal obtained from instead applying conventional beamforming with a Σ channel at beam position $\theta_0 = 0°$. Note that the right panel displays a simplified image, more clearly highlighting the signals and their amplitude after processing. These figures also include the MDL threshold at -115 dBW and the SIR threshold 6 dB below the power of the SOI. For the SOI to be detected, it should be above the MDL threshold (in black), while the interfering signal should be below the SIR threshold (in cyan).

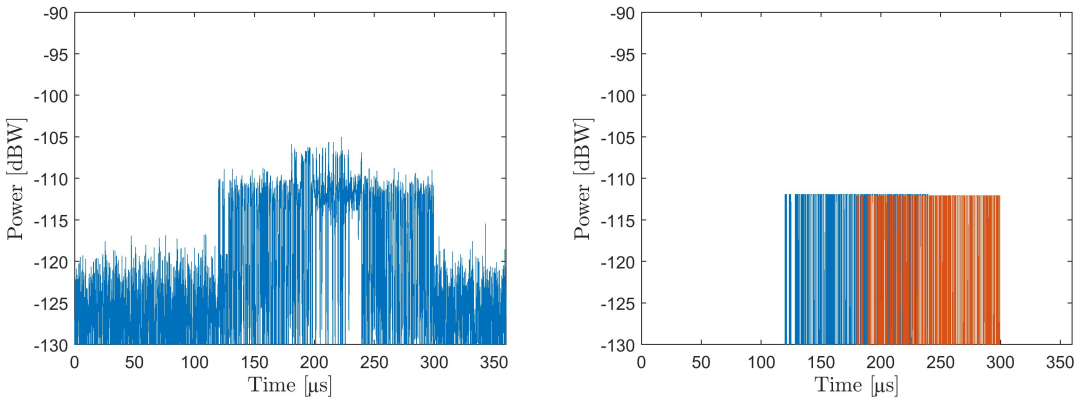

(a) **(b)**

Figure 4.14: The incoming signal $\boldsymbol{x}(t)$ before any processing. **(a)** The actual simulated signal. **(b)** A simplified image, highlighting the SOI (in blue) and the interfering signal (in red).

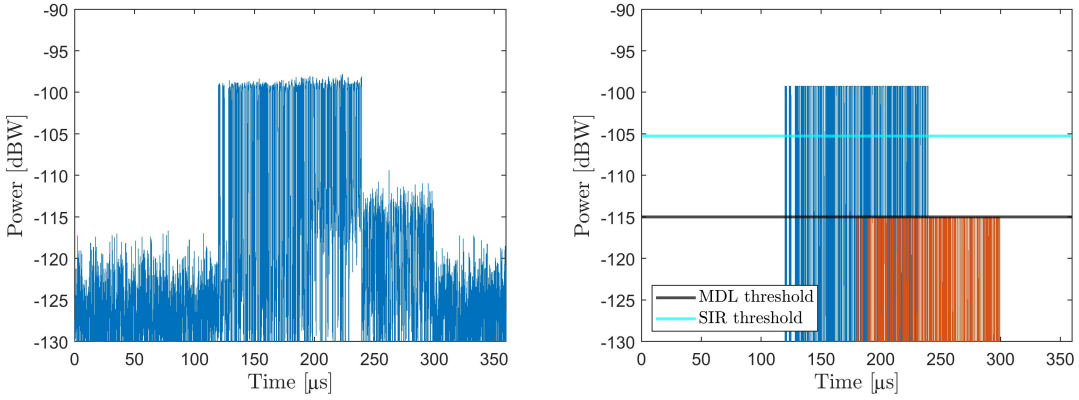

(a) **(b)**

Figure 4.15: The signal obtained from applying the MPDR algorithm. **(a)** The actual simulated signal. **(b)** A simplified image, highlighting the SOI (in blue) and the interfering signal (in red). The MDL threshold is shown in black and the SIR threshold is shown in cyan. In this case, the SOI is detected.

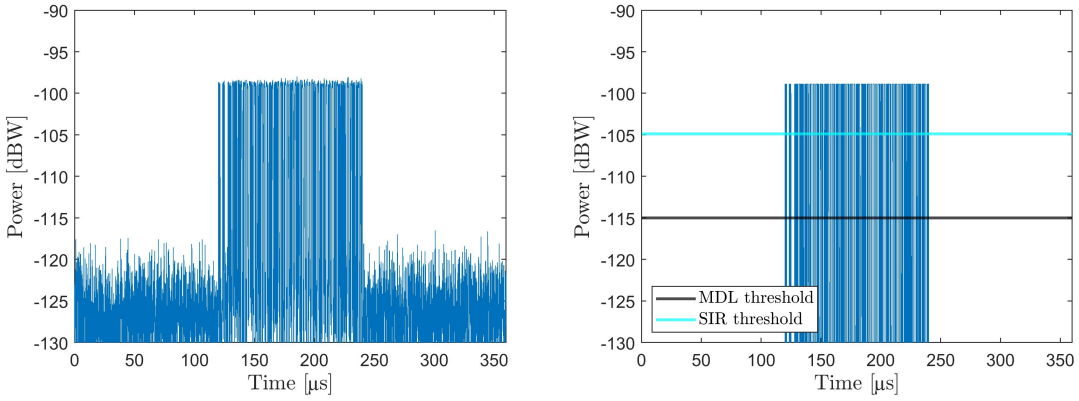

(a) **(b)**

Figure 4.16: The signal obtained from applying the LCMP algorithm. **(a)** The actual simulated signal. **(b)** A simplified image, highlighting the SOI (in blue) and the interfering signal (in red). The MDL threshold is shown in black and the SIR threshold is shown in cyan. In this case, the SOI is detected.

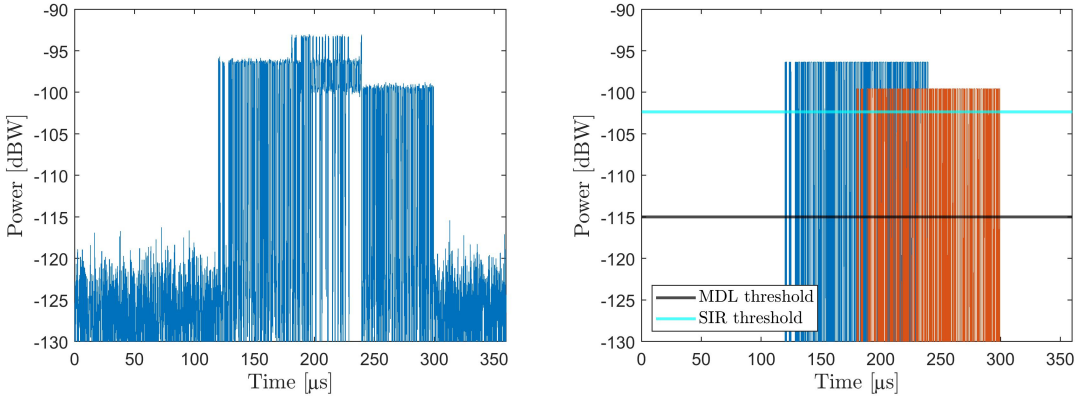

(a) **(b)**

Figure 4.17: The signal obtained from applying conventional beamforming (Σ channel with beam position $\theta_0 = 0°$). **(a)** The actual simulated signal. **(b)** A simplified image, highlighting the SOI (in blue) and the interfering signal (in red). The MDL threshold is shown in black and the SIR threshold is shown in cyan. In this case, the SOI is not detected.

Similar to the results presented in Section 4.2.1, it can be observed that the LCMP (see Figure 4.16) performs well, suppressing the interfering signal below the noise floor and obtaining a rather clear ADS-B signal. The MPDR (see Figure 4.15), not imposing a null constraint, still displays traces of the interfering signal, but can still suppress it relatively well. The example with conventional beamforming (see Figure 4.17) does not generate as satisfactory results, hardly suppressing the interfering signal.

It can be noted that, based on the criteria to classify a successful detection, the adaptive MPDR and LCMP can detect the signal in this case. The conventional system achieves a high gain for the SOI, but the interfering signal power remains too high to meet the signal-to-interference criterion. Thus, the information contained in the ADS-B signal cannot be decoded.

4.3 Further analysis of adaptive algorithms

To further analyze the performance of the adaptive algorithms, the accuracy of the ESPRIT estimation can be studied. Figure 4.18 displays the mean absolute error (MAE) for the DOA estimation $\hat{\theta}_{\text{SOI}}$ of the signal of interest as a function of the true direction θ_{SOI}. The results are shown for the three cases $\gamma = \gamma_1 = 5 \times 10^{-3}$ s^{-1} km^{-2}, $\gamma = \gamma_2 = 1 \times 10^{-2}$ s^{-1} km^{-2} and $\gamma = \gamma_3 = 2 \times 10^{-2}$ s^{-1} km^{-2}. Note that given the symmetry of the problem, only $0° \leq \theta_{\text{SOI}} \leq 90°$ are included.

It can be noted that the MAE is relatively constant for $0° \leq \theta_{\text{SOI}} \leq 70°$. For angles closer to 90°, the received power from the SOI becomes to low, impairing the estimation and increasing the error. The MAE is higher for larger γ, which is reasonable since more signals makes it more difficult to distinguish the SOI and

accurately estimate its direction. For $0° \leq \theta_{\text{SOI}} \leq 70°$, the MAE is around 1.8° for γ_1, 3.1° for γ_2 and 4.9° for γ_3. Even though this can be seen as a relatively accurate estimation, this error can result in problems depending on the interference scenario.

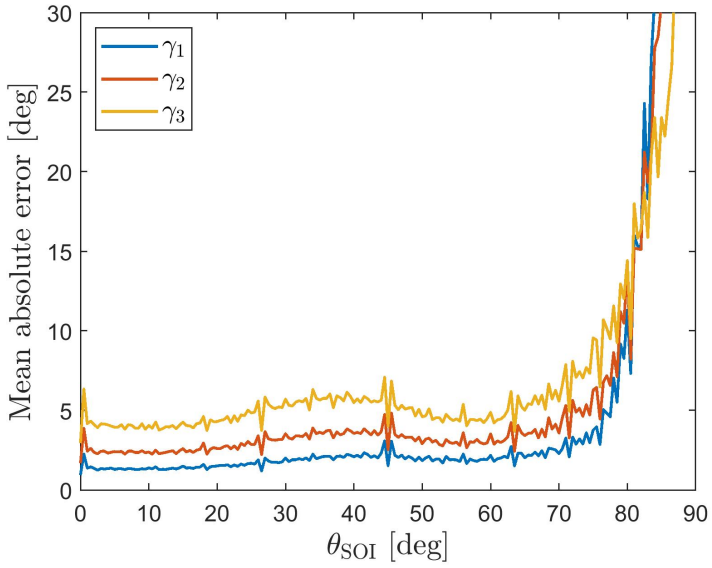

Figure 4.18: The mean absolute error of the DOA estimation with the ESPRIT algorithm as a function of the direction θ_{SOI} for the signal of interest. The results are shown for the three different values of γ.

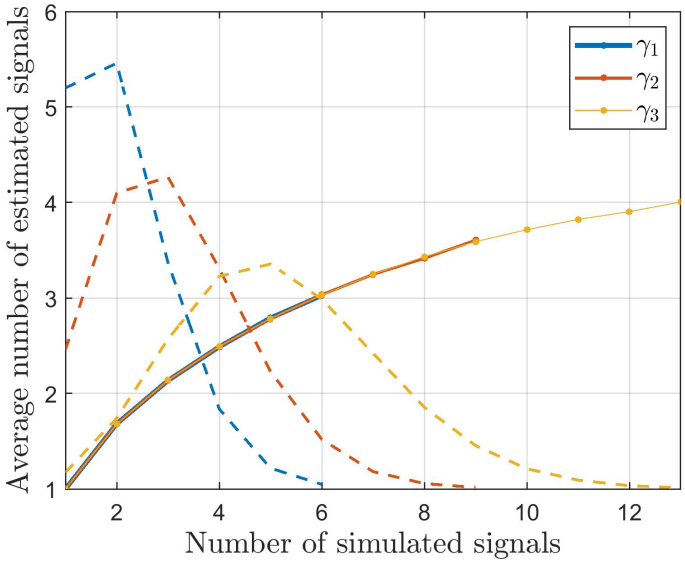

Figure 4.19: The average number of estimated signals in the ESPRIT algorithm as a function of the number of simulated signals. The results are shown for the three different values for γ. The dashed lines in corresponding colors display the distribution of the number of simulated signals. Note that number of simulated signals corresponding to less than 0.1 % of the total number of data points are disregarded.

Figure 4.19 displays the average number of estimated signals in the ESPRIT algorithm as a function of the number of simulated signals (the SOI and the number of interfering signals drawn from a Poisson distribution). Recall that the number of signals is estimated based on that the received signal strength, corresponding to the eigenvalues of the covariance matrix, should be 1 dB above the noise floor. It can be noted that this leads to an underestimation of the number of signals. This increases the risk of losing the SOI, but also removes interfering signals with low contribution to the total signal.

Moreover, the performance of the algorithms can be compared to a scenario in which the exact number of interfering signals and their directions of arrival are known "a priori". Consequently, this comparison can also give an indication of how well the DOA estimation with the ESPRIT algorithm works. Note that the focus here is on MPDR and LCMP only. Based on the results presented in Sections 4.1 and 4.2, the PC algorithm studied here can be assumed to have similar behavior as MPDR.

Figure 4.20 displays the average probability of detection as a function of the γ parameter for the different systems in different subareas. The same subareas as before are analyzed: $0-300$ km, $300-600$ km and $600-900$ km. The probability values are also displayed in Table 4.5. Plots over the probability of detection for the a priori tests can be found in Appendix A.2.

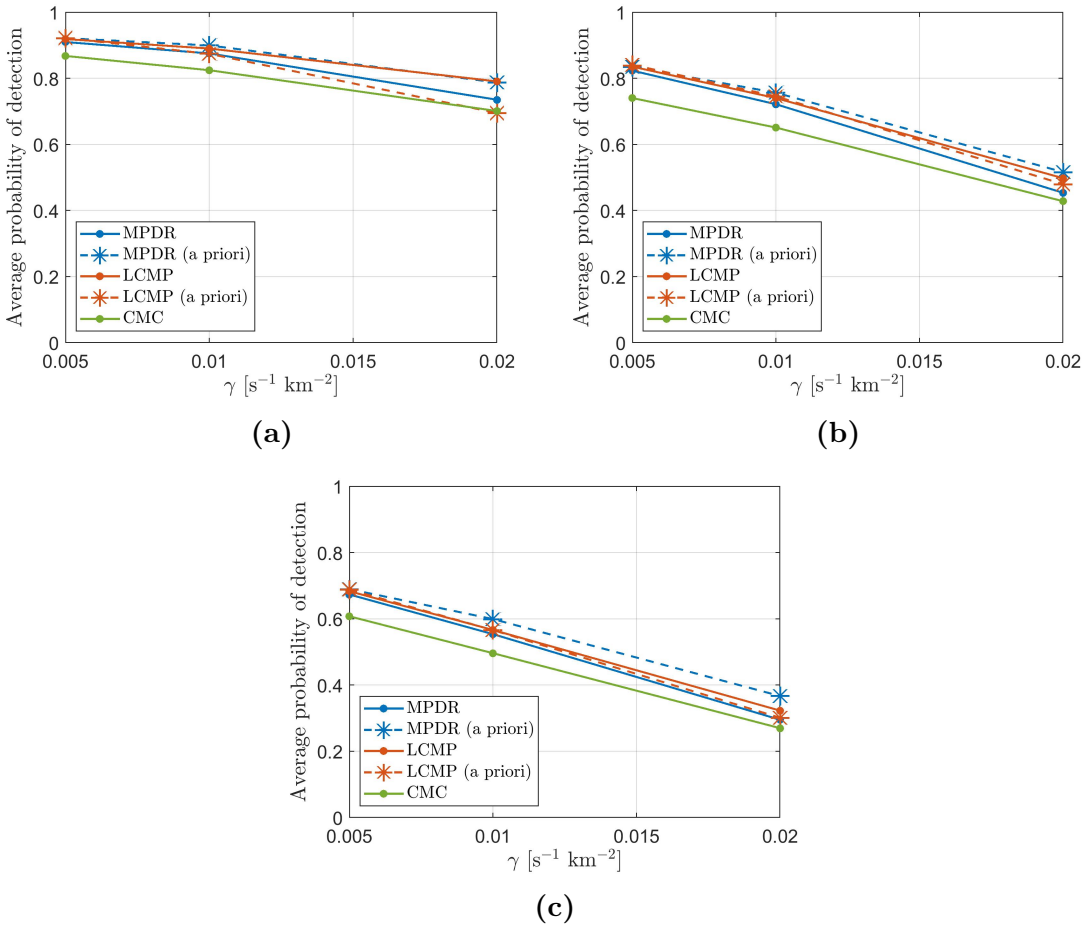

Figure 4.20: Average probability of detection as a function of the message rate per area γ [s^{-1} km^{-2}] for the different systems in different subareas. **(a)** Targets at a distance of 0−300 km. **(b)** 300−600 km. **(c)** 600−900 km. The solid lines are the same as found for MPDR and LCMP in Figure 4.7, where the directions of arrival are estimated. The dashed lines here represent corresponding simulations instead using a priori knowledge of the directions of arrivals. The CMC is included for comparison.

Table 4.5: The average probability of detection shown in Figure 4.20 displayed in table form.

Algorithm	Distance [km] / γ [s^{-1} km^{-2}]	0−300	300−600	600−900
MPDR	5×10^{-3}	0.91	0.82	0.67
	1×10^{-2}	0.88	0.72	0.55
	2×10^{-2}	0.74	0.45	0.29
MPDR (a priori)	5×10^{-3}	0.92	0.83	0.69
	1×10^{-2}	0.90	0.76	0.60
	2×10^{-2}	0.79	0.52	0.37
LCMP	5×10^{-3}	0.92	0.84	0.68
	1×10^{-2}	0.89	0.74	0.57
	2×10^{-2}	0.79	0.50	0.32
LCMP (a priori)	5×10^{-3}	0.92	0.84	0.69
	1×10^{-2}	0.87	0.75	0.57
	2×10^{-2}	0.70	0.48	0.30

Analyzing Figure 4.20 and Table 4.5, it can be noted that the MPDR with a priori information on average gives between 1 % and 24 % higher probability, with the biggest difference in Region 3 and for high disturbance. This could indicate that the ESPRIT algorithm exhibits greater difficulty in distinguishing targets further away, resulting in lower signal power, and in the presence of more interfering signals.

Regarding the LCMP, the scenarios with and without a priori information exhibits more similar results, indicating that it could be less sensitive to estimation errors compared to the MPDR. This is likely due to the null constraints imposed for the LCMP resulting in a sufficiently low gain near the direction of the interfering signals, even if the estimate deviates slightly from the true value.

However, the a priori LCMP displays 7−13 % lower probability of detection for $\gamma = 2{\times}10^{-2}\,s^{-1}\,km^{-2}$, compared to the LCMP with ESPRIT estimation. The reason behind this could be that when applying the ESPRIT algorithm, the interfering signals not reaching 1 dB above the noise are discarded, as shown in Figure 4.19. The a priori LCMP, on the other hand, imposes null constraints for all interfering signals. This could result in imposing more constraints than necessary and therefore a loss of gain in the direction of the SOI. This effect becomes more apparent for high disturbance, with multiple null constraints imposed. This is also the reason for why a priori MPDR outperforms a priori LCMP for higher disturbance.

To see the difference in performance between the a priori tests and the ESPRIT estimates, they are compared to the test cases from before, shown in Table 4.3. Figures 4.21, 4.22 and 4.23 display antenna patterns for the different test cases. Figure 4.23 illustrates the problem of imposing null constraints in the case of high disturbance, heavily reducing the gain in the direction of the SOI for a priori LCMP.

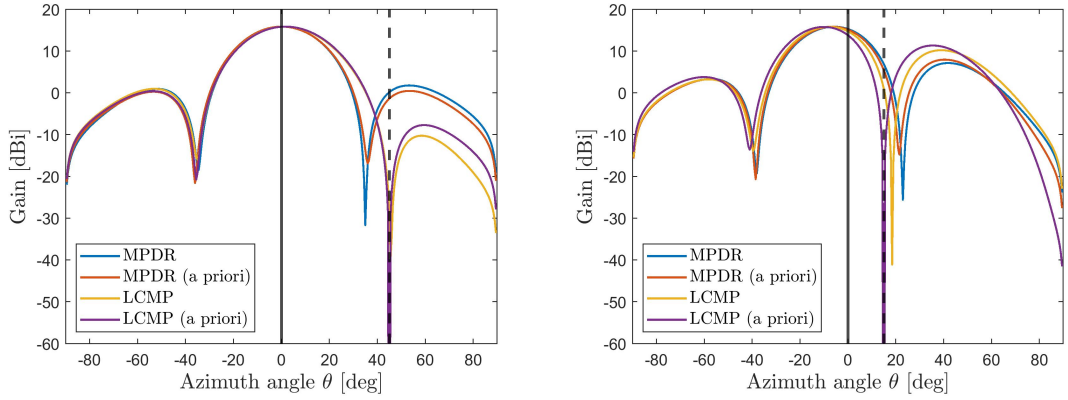

Figure 4.21: Antenna patterns for Case 1a in **(a)**, with one interfering signal at +45°, and for Case 1b in **(b)**, with one interfering signal at +15°.

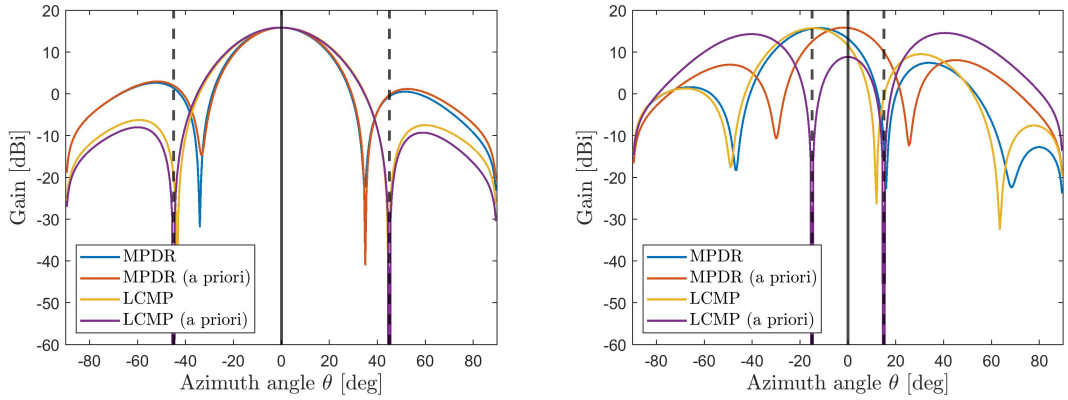

Figure 4.22: Antenna patterns for Case 2a in **(a)**, with two interfering signals at ±45°, and for Case 2b in **(b)**, with two interfering signals at ±15°.

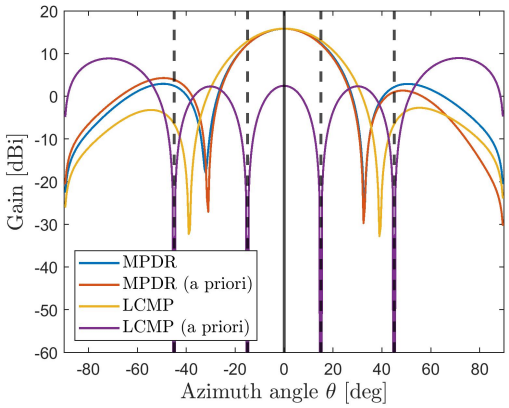

Figure 4.23: Antenna pattern for Case 3, with four interfering signals at ±45° and ±15°.

Finally, it can be interesting to see how well the MPDR and LCMP handles different interference scenarios. More specifically, it can be analyzed how the signal-to-interference ratio depends on the proximity in time and space between the SOI and an interfering signal.

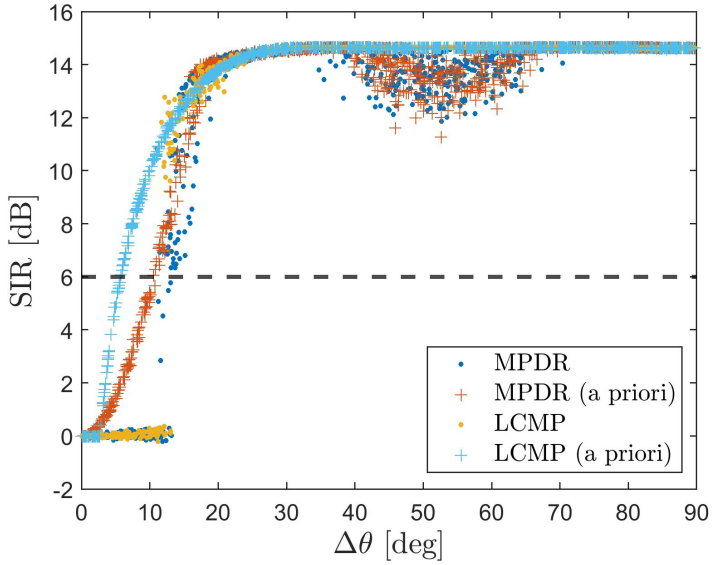

Figure 4.24: The signal-to-interference ratio as a function of the difference in azimuth $\Delta\theta$ between the SOI and one interfering signal. Results for 1,000 runs with randomized angles for the interfering signal. The SIR threshold at 6 dB is marked by a black dashed line.

Figure 4.24 displays the SIR as a function of the difference in azimuth $\Delta\theta$ between the SOI and one interfering signal. The SOI is placed at $r = 500$ km and $\theta = 0°$. The interfering signal is placed at $r = 706$ km and starts 60 µs after the SOI. The figure displays the result of 1,000 runs with randomized angles for the interfering signal. Note that the SIR is calculated with consideration of the noise floor level. Hence, this is the "efficient SIR" mentioned in Section 4.2.1.

It can be noted that the LCMP generates a higher SIR for smaller $\Delta\theta$ compared to MPDR. Analyzing the a priori tests, the LCMP intersects the SIR threshold, thus enabling detection, at $\Delta\theta \approx 6°$. The MPDR, on the other hand, intersects the SIR threshold at $\Delta\theta \approx 11°$. At around $\Delta\theta \approx 30°$, both algorithms converge towards 14.6 dB, corresponding to an SOI with maximum gain and an interfering signal suppressed below the noise floor. Moreover, it can be noted that for $\Delta\theta \lessapprox 15°$, the direction of arrival estimation with ESPRIT fails and the SOI and interfering signal cannot be distinguished from each other, resulting in an SIR around 0 dB.

Furthermore, it can be observed that several of the runs for MPDR (both a priori and ESPRIT estimation) in the interval $40° \leq \Delta\theta \leq 60°$ results in a lower SIR. This may be due to interfering signals arriving further from the antenna normal at 0° experiencing a smaller effective aperture area, thus having lower signal power at the receiving antenna. These signals therefore have a lesser impact on the signal

covariance matrix, making it more difficult for the MPDR to place implicit nulls. For $\Delta\theta \gtrapprox 60°$, this is compensated by the rather low received signal power from the interfering signal, making an inexact null placement less of a problem.

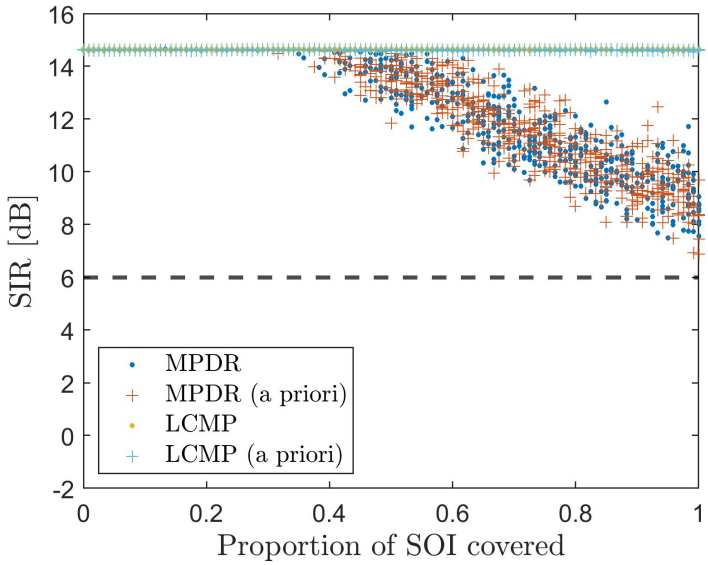

Figure 4.25: The signal-to-interference ratio as a function of the proportion of the signal of interest covered by one interfering signal. Results for 1,000 runs with randomized proportions covered. The SIR threshold at 6 dB is marked by a black dashed line.

Figure 4.25 displays the SIR as a function of the proportion of the signal of interest covered by one interfering signal, i.e., the relative time delay between the two signals. The SOI is placed at $r = 500$ km and $\theta = 0°$. The interfering signal is placed at $r = 706$ km and $\theta = 45°$. The figure displays the result of 1,000 runs with randomized starting times for the interfering signal.

It can be noted that the MPDR (both a priori and ESPRIT estimation) displays a clear decrease in SIR as the SOI becomes more covered, from the maximum SIR around 14.6 dB for a clean SOI to around 9 dB for a fully covered. The LCMP performs equally well for all proportions, indicating that the imposed explicit null constraint efficiently suppresses the interfering signal in this case.

5

Discussion

In this chapter, implications of the results are discussed in relation to the underlying theory. Furthermore, limitations of the method and consequences of the several assumptions are discussed. Finally, possibilities for future studies are discussed as well.

5.1 Implications of the results

Analyzing the results presented in previous chapter, it can be noted that the multi-channel system applying digital conventional beamforming (CMC) consequently outperforms the two-channel Σ/Δ system applying analog conventional beamforming. This is reasonable with regards to the functionality of digital beamforming, as explained in Section 2.5. The digitized phase shifters enable reception in multiple beam positions simultaneously. Consequently, this reduces the risk of accidentally having maximum gain in a disadvantageous direction when the signal of interest arrives, which is also reflected in the obtained results. The difference is most apparent for targets further away (600−900 km) and in the presence of more interfering signals, with on average up to five times higher probability of detection compared to the Σ/Δ system. This could be reasonable since the signal-to-interference ratio is on average smaller for high disturbance, resulting in greater sensitivity to changes in gain.

Unlike the conventional beamforming, the adaptive beamforming algorithms do not rely on a specific set of predetermined beam positions. In the simulations, a set of seven beam positions covering the area is used for the conventional systems. This creates the leaf-like shapes of the plots shown in Figures 4.1 and 4.2. The maximum gain, and consequently the maximum possible detection range, is lower between the beams. This affects the average performance in the outer region compared to the adaptive algorithms. However, increasing the number of beam positions would reduce the gap between the beams. In this way, the CMC would on average generate higher probability of detection compared to the results obtained here.

Regarding the adaptive algorithms, the LCMP exhibits the best performance. The probability of detection is consequently higher compared to the CMC, with on average 20 % higher probability of detection for targets at a distance of 600−900 km and in the presence of high disturbance. The results could indicate that the null constraints imposed in the optimization efficiently suppresses the interfering signals.

The MPDR and PC exhibits on average a lower performance than the LCMP, but higher than the conventional multi-channel system. The inherent difference compared to the LCMP is that no null constraints are imposed in the optimization. The nulling is instead performed implicitly, relying on the information contained in the covariance matrix $\boldsymbol{R}_x$. Albeit more computationally efficient, this could result in more inexact placement of the nulls. This also results in the MPDR being more sensitive to interfering signals being close in space and time, as shown in Figures 4.24 and 4.25. Note that the MPDR possibly would perform a more exact nulling for a higher sampling frequency, resulting in a better estimation of the covariance matrix.

Comparing the MPDR and PC, they display rather similar results. The optimization of the output power shown in Section 2.6.2 is the same for the two algorithms. The difference instead lies in the calculation of the covariance matrix. Instead of using the covariance matrix directly, the PC projects the incoming signal into a lower-dimensional signal-plus-interference subspace. Since the two methods generate similar results, this could indicate that the dimensionality reduction performed works well and that the principal components capture the most valuable signal information. The dimension of the signal-plus-interference subspace is estimated by requiring that the eigenvalues to the signal covariance matrix should be 1 dB above the noise floor. The performance of the PC dimensionality reduction would possibly degrade with a higher threshold, resulting in a greater loss of information.

The ESPRIT algorithm for estimating the directions of arrival generated a mean absolute error of around 2° to 5°, depending on the degree of disturbance (see Figure 4.18). The estimation works well in the sense that the "a priori" tests, where the directions are assumed to be known, do not display significantly different results. In the case test with one interfering signal, the algorithm cannot distinguish the interfering signal and the SOI from each other for $\Delta\theta \lessapprox 15°$, potentially reducing the performance in such scenarios. One important aspect of the application of the ESPRIT algorithm is the estimation of the subspace dimension, i.e., the total number of incoming signals. This is discussed more in the upcoming section, where several limitations of the method are considered.

5.2 Limitations of the method

There are multiple approximations and sources of error affecting the results obtained. One aspect is the choice of parameter values in the simulation. This, for example, includes the transponder output power, the target altitude, the different signal thresholds, and parameters regulating the antenna geometry such as the number of antenna elements and the distance between them. The parameters were chosen either based on ICAO regulations, earlier work in this topic or in consultation with supervisors to obtain fairly realistic scenarios. Some of the choices were also made to obtain physically reasonable results. For example, the maximum possible detection range (dependent on the output power, MDL and antenna geometry) should be smaller than maximum line-of-sight distance (dependent on the target altitude). Moreover, the distance between the antenna elements should be smaller

than $\lambda/2$, to avoid undesirable grating lobes [6]. Since this work has rather been a comparative analysis between systems employing different beamforming techniques, the exact choice of parameters was deemed secondary.

The antenna gain was approximated according to Equation (3.1). This is based on the idea that the amplitude of the beam pattern is limited by a maximum possible gain set by the effective aperture area. There are, however, other approaches which could be studied further. For example, the gain can also be calculated as $G = \eta D$, where D is the directivity [17]. The directivity can be obtained by dividing the radiation intensity, i.e., the power per unit solid angle, with the total radiated power. In the end, this is just another way of normalizing the beam pattern and another way of capturing the underlying physics. Instead of thinking of the situation as signals absorbed by an antenna with a certain effective area, it can be seen as what fraction of the total energy is available in a particular direction. The focus of this work, however, has been on the shape of the beam patterns rather than their exact normalization.

The probability of a successful detection was modelled based on two main criteria: 1) the signal power of the SOI should be above the minimum detection level, and 2) the maximum of the sum of the interfering signal power should be below the signal-to-interference threshold. This is a simplified image deemed sufficient to compare the different beamforming techniques in the work, but the model could be developed further. For example, the actual output signal in the time domain, $y(t) = \boldsymbol{w}^{\mathrm{H}}\boldsymbol{x}(t)$, could be studied directly rather than focusing on the amplitude of the signals. For example, a criterion based on the proximity of the resulting waveform to the desired ADS-B signal could be implemented.

When estimating the number of signals using the ESPRIT algorithm, as well as applying the principal component (PC) beamforming, the dimension of the signal-plus-interference subspace had to be estimated. As stated earlier, this was done by assuming that eigenvalues of the signal covariance matrix with a magnitude of 1 dB above the noise floor corresponded to signals. A too low threshold could result in noise being included, impairing the estimation. On the other hand, a too high threshold could result in the SOI being lost. Moreover, this method implies that $D + 1 \leq N$, the total number of signals is at most the number of antenna elements. This assumption is not necessarily true, especially as the disturbance increases. Recall that the number of interfering signals is a Poisson random variable. In this case, the interfering signals were assumed to be of type Mode S Long and Mode S Short. Note that the sum of two independent Poisson random variables $D_{\text{long}} \sim \text{Poi}(\lambda_{\text{Poi}}^{\text{long}})$ and $D_{\text{short}} \sim \text{Poi}(\lambda_{\text{Poi}}^{\text{short}})$ is given by $D \sim \text{Poi}(\lambda_{\text{Poi}}^{\text{long}} + \lambda_{\text{Poi}}^{\text{short}})$.

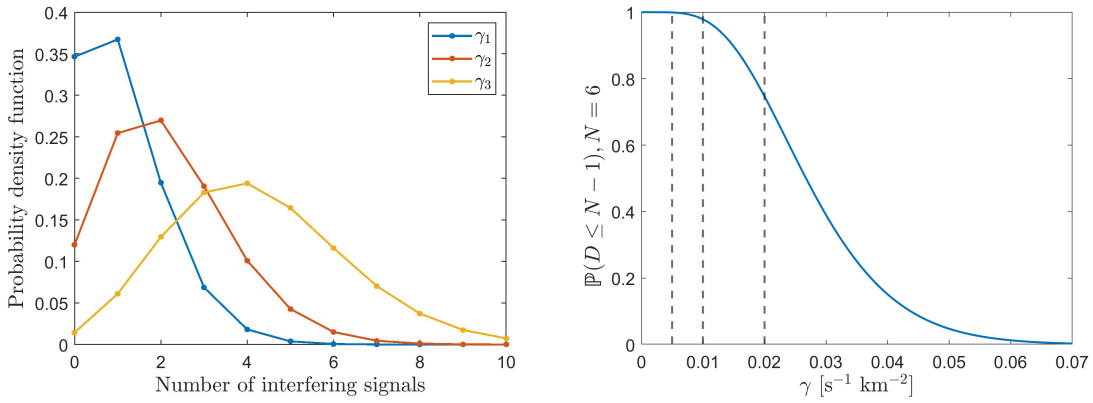

(a) **(b)**

Figure 5.1: (a) The discrete Poisson probability density function for the number of interfering signals. The three different cases for the γ parameter are shown. **(b)** The probability that the number of interfering signals are ≤ 5 as a function of the γ parameter. The three different cases investigated in this work are displayed as black dashed lines.

Figure 5.1(a) displays the probability density function for $D \sim \text{Poi}(\lambda_{\text{Poi}}^{\text{long}} + \lambda_{\text{Poi}}^{\text{short}})$ for the cases $\gamma = \gamma_1 = 5 \times 10^{-3}$ s^{-1} km^{-2} (blue), $\gamma = \gamma_2 = 1 \times 10^{-2}$ s^{-1} km^{-2} (red) and $\gamma = \gamma_3 = 2 \times 10^{-2}$ s^{-1} km^{-2} (yellow). As can be seen, the assumption that $D \leq N-1$, when $N = 6$, holds for $\gamma = \gamma_1$ and $\gamma = \gamma_2$. In these cases, $\mathbb{P}(D \leq 5) \approx 0.99$ and $\mathbb{P}(D \leq 5) \approx 0.98$, respectively. For $\gamma = \gamma_3$, however, $\mathbb{P}(D \leq 5) \approx 0.75$. Therefore, there is a 25 % risk to obtain more than $N = 6$ signals in total, thus exceeding the number of degrees of freedom. This becomes a more apparent problem as γ increases, as illustrated in Figure 5.1(b). For a larger number of interfering signals, however, it is more likely that some of them are coming from sources located far away in distance and azimuth relative to the receiving antenna. This reduces the received power heavily, and thus reduces the effective number of signals reaching above the noise floor. This is illustrated in Figure 4.19. In future studies, this problem could be studied in greater detail.

In the DOA estimation, the direction for the signal of interest was determined as $\hat{\theta}_{\text{SOI}} = \min |\hat{\theta}_i - \theta_{\text{SOI}}|$, where i counts the number of estimated signals. This could potentially lead to problems when the SOI cannot be distinguished from one or several of the interfering signals. In such a case, the gain is instead maximized in the direction of an interfering signal, thus impairing detection of the SOI. An example of this can be seen in Figure 4.12(b), where the gain is maximized at $\theta \approx -15°$. Instead of only choosing the direction closest to the true value, all possible weight vectors obtained could have been iterated over. This would, however, heavily increase the simulation time.

The Monte Carlo method was applied to obtain estimates for the probability of detection in every pixel in the spatial grid. Based on the convergence for randomly chosen test points, 1,000 iterations were deemed sufficient, resulting in an approximate error margin of around ± 0.02 for a 95 % confidence interval. More iterations

than 1,000 could have been used, but this would be at the expense of a longer simulation time, as seen in Figure 3.3(b).

5.3 Future studies

The are several ways to further develop the work presented in this thesis. Several of the limitations discussed in the previous section could be explored further, such as analyzing the criteria for probability of detection, how the performance of MPDR depends on the sample rate and how the dimensionality reduction for PC depends on the signal power threshold. In this work, the only simulation parameter varied has been the γ parameter, describing the degree of disturbance in the air. In new examinations, more parameters could be varied. It would for example be interesting to test different values for the signal-to-interference threshold, SIR_{min}, and analyze how this would affect the probability of detection for the different beamforming techniques.

Furthermore, more adaptive algorithms could be analyzed. For example, a dimensionality reduction using principal component analysis could be performed for the LCMP in the same way as for the MPDR. There are also algorithms where the weights are updated iteratively, such as the least mean squares (LMS) algorithm. This is in contrast to the sample matrix inversion analyzed here, in which the weights are obtained directly. In the LMS algorithm, the mean-squared error between a desired signal and the output signal is minimized using gradient descent [6]. This has been shown to generate good results and lower computational complexity [25]. Moreover, blind adaptive beamforming algorithms could be tested. In such algorithms, no reference signal is needed, meaning that the directions of arrival do not have to be estimated [8]. This could lead to better performance in some scenarios, but would on the other require more computation.

Additionally, other types of constraints for the LCMP could be explored. As mentioned, one risk of imposing null constraints is that too much gain is lost in the direction of the signal of interest. For example, constraints for the derivative of the beam pattern could be imposed. It has been shown that imposing derivative constraints in the vicinity of a null could improve robustness [6]. Moreover, the weights could also be optimized further using different optimization techniques. Other work has shown that use of for example reinforcement learning, in which the action space is defined by the possible changes in the weight vector, could potentially increase performance [26]. Moreover, evolutionary algorithms such as genetic algorithms and particle swarm optimization have shown promising results [27], [28].

It would also be interesting to compare the accuracy of the ESPRIT algorithm to other DOA estimation algorithms. For example, the performance of statistical methods such a maximum likelihood estimation can be analyzed. Another subspace-based method is MUSIC (Multiple signal classification), which exploits properties of the noise subspace rather than signal-plus-interference subspace. Some works indicate that MUSIC, albeit more computationally expensive, could generate more accurate estimations [29]. Moreover, the MPDR beamformer could be used for

DOA estimation as well by analyzing $1/\boldsymbol{v}^{\mathrm{H}}(\theta)\boldsymbol{R}_x^{-1}\boldsymbol{v}(\theta)$, the inverse denominator in Equation (2.10) as a function of θ. This corresponds to the spatial spectrum of the signal, from which the directions of arrival can be estimated [6].

In future studies, higher values for γ, the message rate per area, could be analyzed. This would, however, require a more careful analysis of the problem with the number of signals exceeding the number of antenna elements. For examples, the total incoming signal could be divided into smaller time slots, each containing a sufficiently small number of signals. Moreover, a concept that could be examined is difference co-arrays [30]. This signal processing technique makes use of the fact that the number of unique antenna element pairs exceeds the number of unique elements, N, and that the number of unique pairs increases with N^2. From this, a virtual array with more degrees of freedom can be created, thus enabling resolution of more signals than physical antenna elements.

Finally, it would be interesting to develop this work by performing more realistic simulations. For example, an inhomogeneous density of transponders could be assumed, resulting in different γ in different parts of the simulated area. This would mimic a more accurate description of the air traffic. It would also be more realistic to allow for moving targets, relating this study to field of target tracking. However, the assumption of stationary targets used here can be deemed sufficient with regards to the aircraft speed in relation to the size of the area and the simulated time. Furthermore, this thesis only considers reception of ADS-B signals, which are transmitted from targets without any interrogation. A future study could generalize this and analyze the performance of SSR interrogations and replies using digital beamforming.

6

Conclusion

In this thesis, the performance of a secondary surveillance radar was studied. More specifically, the probability of successfully detecting an incoming ADS-B signal, in the presence of interfering signals, was estimated for several different scenarios. This was done for different multi-channel systems implementing different types of digital beamforming, conventional and adaptive. Their performance was benchmarked against a two-channel system Σ/Δ system, using analog conventional beamforming.

The analysis indicates that the multi-channel system using conventional beamforming shows promising results, consequently outperforming the Σ/Δ system. Among the adaptive algorithms, the LCMP, imposing null constraints for the interfering signals, performs best, resulting in higher probability of detection compared to the conventional multi-channel system. The MPDR, in general, gives slightly lower probability of detection compared to the LCMP, but still illustrates that suppression of interfering signals could be performed adaptively without explicit nulling. The principal component (PC) beamformer, based on the MPDR, displays similar results, illustrating that a dimensionality reduction of the incoming data could be performed without loss of information. The ESPRIT algorithm used for estimating the directions of arrival provides satisfactory results in general, but alternative methods could be analyzed further to increase the accuracy.

This study highlights the potential of applying digital beamforming, conventional and especially adaptive. However, it is worth noting that the work presented in this thesis includes several limitations and simplifications. Further research is therefore needed to analyze the applicability of the results found here. To build on this work, future studies could focus on increasing the realism in the modelling, as well as analyzing more adaptive beamforming techniques.

As traffic in the air increases, so does the risk of an incoming signal from a desired target being interfered by other signals. Using accurate and computationally efficient signal processing algorithms to improve the reception performance for a signal of interest therefore becomes increasingly important. Analyzing different types of beamforming techniques can, to this end, play a crucial role. Consequently, studies on how to optimize the beamforming process, using both conventional and adaptive algorithms, will continue to be a topic of great interest in theoretical and applied signal processing.

Bibliography

[1] J. Sun, *The 1090 Megahertz Riddle: A Guide to Decoding Mode S and ADS-B Signals*. TU Delft OPEN Publishing, 2 ed., 2021.

[2] J. Eaves and E. Reedy, *Principles of modern radar*. Springer Science & Business Media, 2012.

[3] L. Bowden, "The story of IFF (identification friend or foe)," *IEE Proceedings A (Physical Science, Measurement and Instrumentation, Management and Education, Reviews)*, vol. 132, no. 6, pp. 435–437, 1985.

[4] ICAO, *Aeronautical Surveillance Manual*, 2nd ed., 2017.

[5] D. Johnson and D. Dudgeon, *Array Signal Processing: Concepts and Techniques*. Prentice-Hall signal processing series, P T R Prentice Hall, 1993.

[6] H. L. Van Trees, *Optimum array processing: Part IV of detection, estimation, and modulation theory*. John Wiley & Sons, 2002.

[7] K.-B. Yu, "Digital beamforming of multiple simultaneous beams for improved target search," in *2009 IEEE Radar Conference*, pp. 1–5, IEEE, 2009.

[8] W. Wang, R. Wu, and J. Liang, "ADS-B signal separation based on blind adaptive beamforming," *IEEE Transactions on Vehicular Technology*, vol. 68, no. 7, pp. 6547–6556, 2019.

[9] G. Galati, N. Petrochilos, and E. G. Piracci, "Degarbling Mode S replies received in single channel stations with a digital incremental improvement," *IET Radar, Sonar & Navigation*, vol. 9, no. 6, pp. 681–691, 2015.

[10] F. Le Neindre, G. Ferre, D. Dallet, F. Letellier, and K. Pitois, "A successive interference cancellation-based receiver for secondary surveillance radar," *IEEE Transactions on Aerospace and Electronic Systems*, vol. 59, no. 2, pp. 805–816, 2022.

[11] M. A. Garcia, J. Stafford, J. Minnix, and J. Dolan, "Aireon space based ADS-B performance model," in *2015 Integrated Communication, Navigation and Surveillance Conference (ICNS)*, pp. C2–1, IEEE, 2015.

[12] R. E. Boisvert and V. A. Orlando, "ADS-Mode S system overview," in *[1993 Proceedings] AIAA/IEEE Digital Avionics Systems Conference*, pp. 104–109, IEEE, 2005.

[13] C. Heumann and M. S. Shalabh, *Introduction to statistics and data analysis*. Springer, 2016.

[14] S. Banerjee and V. V. Dwivedi, "Effect of signal to interference ratio on adaptive beamforming techniques," *Journal of King Saud University-Engineering Sciences*, vol. 30, no. 4, pp. 313–319, 2018.

[15] D. Richardson, "AESA radar technology," *Armada International*, vol. 39, no. 3, pp. 24–30, 2015.

[16] C. A. Balanis, *Antenna Theory: Analysis and Design*. John Wiley & Sons, 2016.

[17] H. Rahman, *Fundamental Principles of Radar*. CRC Press, 2019.

[18] A. Roederer, E. Farr, L. Foged, M. Francis, R. Hansen, R. Haupt, and K. Warnick, "IEEE standard for definitions of terms for antennas," *IEEE Std*, pp. 145–2013, 2014.

[19] R. Landauer, "Johnson-Nyquist noise derived from quantum mechanical transmission," *Physica D: Nonlinear Phenomena*, vol. 38, no. 1-3, pp. 226–229, 1989.

[20] C. Wolff, "Minimum Detectable Signal." `https://www.radartutorial.eu/09.receivers/rx51.en.html`. [Online]. Accessed on: 2024-05-05.

[21] N. R. Goodman, "Statistical analysis based on a certain multivariate complex Gaussian distribution (an introduction)," *The Annals of Mathematical Statistics*, vol. 34, no. 1, pp. 152–177, 1963.

[22] C. Wolff, "Analogue vs. Digital Beamforming." `https://www.radartutorial.eu/06.antennas/Digital%20Beamforming.en.html`. [Online]. Accessed on: 2024-05-05.

[23] G. Feng, J. Huang, and M. Yi, "General formulas of effective Earth radius and modified refractive index," *IEEE Access*, vol. 9, pp. 115068–115076, 2021.

[24] Flightradar24, "Flightradar24: Live Flight Tracker - Real-Time Flight Tracker Map." `https://www.flightradar24.com/`. [Online]. Accessed on: 2024-05-07.

[25] R. K. Patra and C. K. Nayak, "A comparison between different adaptive beamforming techniques," in *2019 International Conference on Range Technology (ICORT)*, pp. 1–4, IEEE, 2019.

[26] C. Hao, X. Sun, and Y. Liu, "Adaptive beamforming based on the deep reinforcement learning," in *2022 IEEE International Conference on Networking, Sensing and Control (ICNSC)*, pp. 1–6, IEEE, 2022.

[27] Q. Wu and Z. L. Gong, "On the performance of genetic algorithm based adaptive beamforming," in *6th International SYmposium on Antennas, Propagation and EM Theory, 2003. Proceedings. 2003*, pp. 339–343, IEEE, 2003.

[28] S. Darzi, T. S. Kiong, M. T. Islam, M. Ismail, S. Kibria, and B. Salem, "Null steering of adaptive beamforming using linear constraint minimum variance assisted by particle swarm optimization, dynamic mutated artificial immune

system, and gravitational search algorithm," *The Scientific World Journal*, vol. 2014, 2014.

[29] O. A. Oumar, M. F. Siyau, and T. P. Sattar, "Comparison between MUSIC and ESPRIT direction of arrival estimation algorithms for wireless communication systems," in *The first international conference on future generation communication technologies*, pp. 99–103, IEEE, 2012.

[30] G. Jiang, M. Wang, X. Mao, C. Qian, Y. Liu, and A. Nehorai, "Underdetermined direction-of-arrival estimation using difference coarray in the presence of unknown nonuniform noise," *IEEE Access*, vol. 7, pp. 157643–157654, 2019.

[31] C. W. Therrien, *Discrete random signals and statistical signal processing*. Prentice Hall PTR, 1992.

[32] R. Remmert, *Theory of complex functions*, vol. 122. Springer Science & Business Media, 1991.

A

Appendix

A.1 Complex optimization

This section contains more details and explanations of the complex optimization performed in the derivation of the optimal beamformers in Section 2.6.2.

Assume a complex optimization problem where the function $f : \mathbb{C}^N \to \mathbb{R}$ is minimized subject to the constraint $C(\boldsymbol{z}) = 0$, where $C : \mathbb{C}^N \to \mathbb{C}$. Consequently,

$$\begin{cases} \min\limits_{\boldsymbol{z}} & f(\boldsymbol{z}) \\ \text{s.t.} & C(\boldsymbol{z}) = 0. \end{cases}$$

Effectively, the constraint $C(\boldsymbol{z}) = 0$ corresponds to two separate constraints: $\mathrm{Re}[C(\boldsymbol{z})] = C_\mathrm{r}(\boldsymbol{z}) = 0$ and $\mathrm{Im}[C(\boldsymbol{z})] = C_\mathrm{i}(\boldsymbol{z}) = 0$ [31]. The Lagrangian can be written as

$$\mathcal{L}(\boldsymbol{z}, \lambda_\mathcal{L}) = f(\boldsymbol{z}) + \mu_1 C_\mathrm{r}(\boldsymbol{z}) + \mu_2 C_\mathrm{i}(\boldsymbol{z}),$$

where $\mu_1, \mu_2 \in \mathbb{R}$ are the Lagrange multipliers. Now define $\lambda = \lambda_\mathrm{r} + i\lambda_\mathrm{i}$, and let $\mu_1 = 2\lambda_\mathrm{r}$ and $\mu_2 = -2\lambda_\mathrm{i}$. This gives

$$\mathcal{L}(\boldsymbol{z}, \lambda_\mathcal{L}) = f(\boldsymbol{z}) + 2\lambda_\mathrm{r} C_\mathrm{r}(\boldsymbol{z}) - 2\lambda_\mathrm{i} C_\mathrm{i}(\boldsymbol{z}) = f(\boldsymbol{z}) + 2\mathrm{Re}[\lambda C(\boldsymbol{z})] =$$

$$= f(\boldsymbol{z}) + \lambda C(z) + \lambda^\mathrm{H} C^\mathrm{H}(z).$$

Hence, it is equivalent to define a Lagrangian with the conjugate of the constraint, rather than analyzing its real and imaginary parts separately.

Moreover, it can be noted that $\boldsymbol{z} = \boldsymbol{x} + i\boldsymbol{y}$ and $\boldsymbol{z}^\mathrm{H} = \boldsymbol{x} - i\boldsymbol{y}$ can be regarded as independent variables when performing complex optimization. This can be seen be studying the Wirtinger derivatives for the different components of $\boldsymbol{z}$ [32]. For a component $z_k = x_k + iy_k$, where $k = 1, 2, \ldots, N$, the Wirtinger derivatives are defined as

$$\frac{\partial}{\partial z_k} = \frac{1}{2}\left(\frac{\partial}{\partial x_k} - i\frac{\partial}{\partial y_k}\right), \frac{\partial}{\partial z_k^\mathrm{H}} = \frac{1}{2}\left(\frac{\partial}{\partial x_k} + i\frac{\partial}{\partial y_k}\right).$$

This gives,

$$\frac{\partial z_k}{\partial z_k} = 1, \frac{\partial z_k^\mathrm{H}}{\partial z_k} = 0, \frac{\partial z_k}{\partial z_k^\mathrm{H}} = 0, \frac{\partial z_k^\mathrm{H}}{\partial z_k^\mathrm{H}} = 1.$$

Consequently, z_k and z_k^H can be regarded as independent variables.

A.2 Additional results

This section contains results for the probability of detection for the ”a priori” tests for MPDR and LCMP discussed in Section 4.3. Figure A.1 displays the results for MPDR and Figure A.2 displays the results for LCMP.

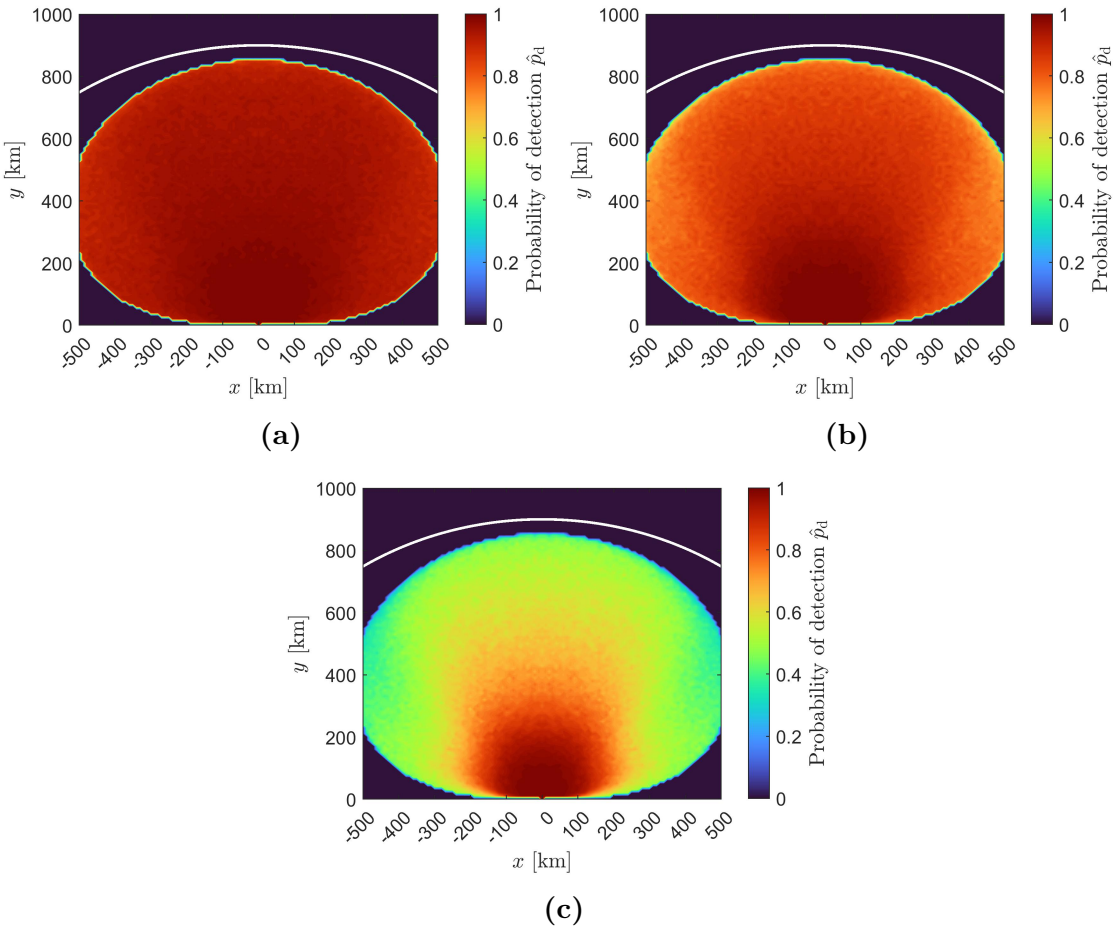

Figure A.1: Estimated probability of detection for the multi-channel system with adaptive MPDR beamforming with a priori knowledge of the number of signals and their direction. **(a)** The case $\gamma = 5 \times 10^{-3}$ s^{-1} km^{-2}. **(b)** The case $\gamma = 1 \times 10^{-2}$ s^{-1} km^{-2}. **(c)** The case $\gamma = 2 \times 10^{-2}$ s^{-1} km^{-2}. Red tones indicate higher probability, while blue tones indicate a lower probability. Note that the maximum line-of-sight distance at 900 km is marked by a white line.

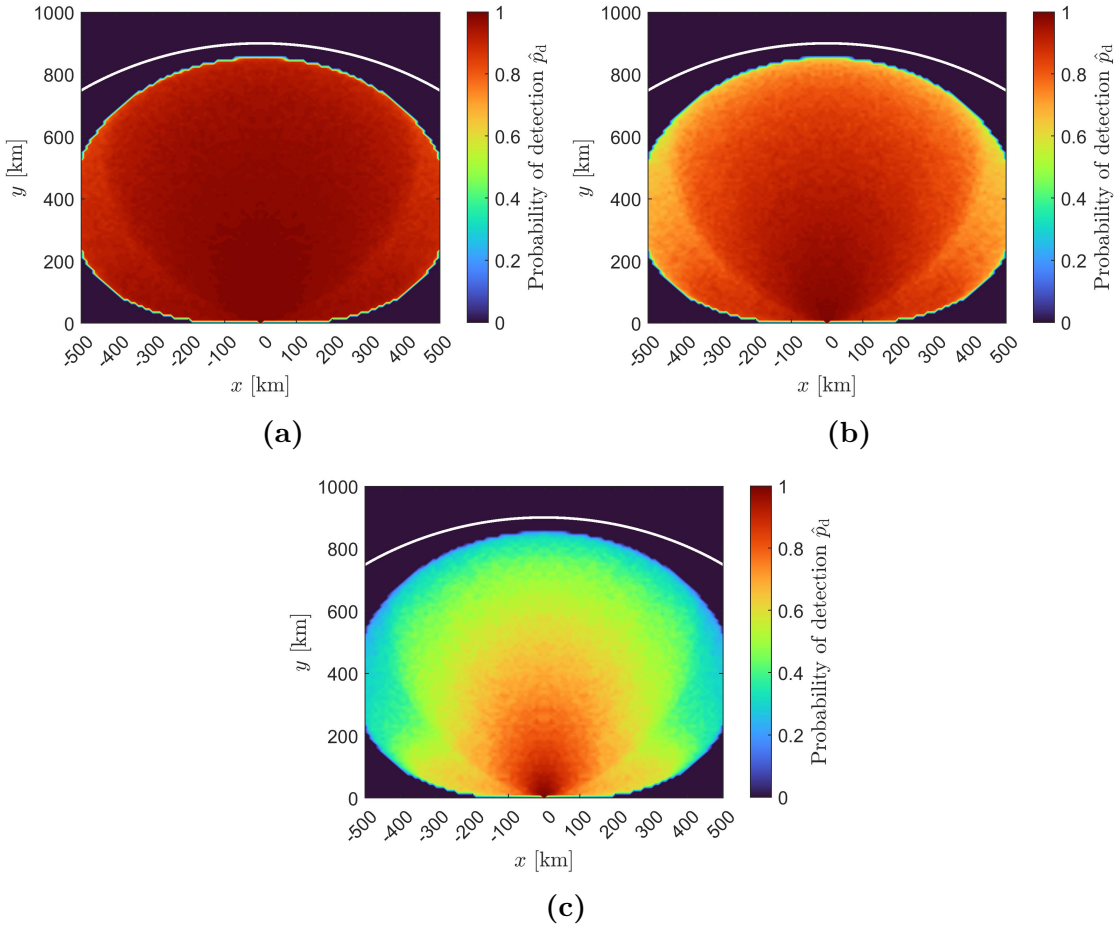

Figure A.2: Estimated probability of detection for the multi-channel system with adaptive LCMP beamforming with a priori knowledge of the number of signals and their direction. **(a)** The case $\gamma = 5 \times 10^{-3}$ s^{-1} km^{-2}. **(b)** The case $\gamma = 1 \times 10^{-2}$ s^{-1} km^{-2}. **(c)** The case $\gamma = 2 \times 10^{-2}$ s^{-1} km^{-2}. Red tones indicate higher probability, while blue tones indicate a lower probability. Note that the maximum line-of-sight distance at 900 km is marked by a white line.

DEPARTMENT OF MATHEMATICAL SCIENCES
CHALMERS UNIVERSITY OF TECHNOLOGY
Gothenburg, Sweden
www.chalmers.se

CHALMERS
UNIVERSITY OF TECHNOLOGY